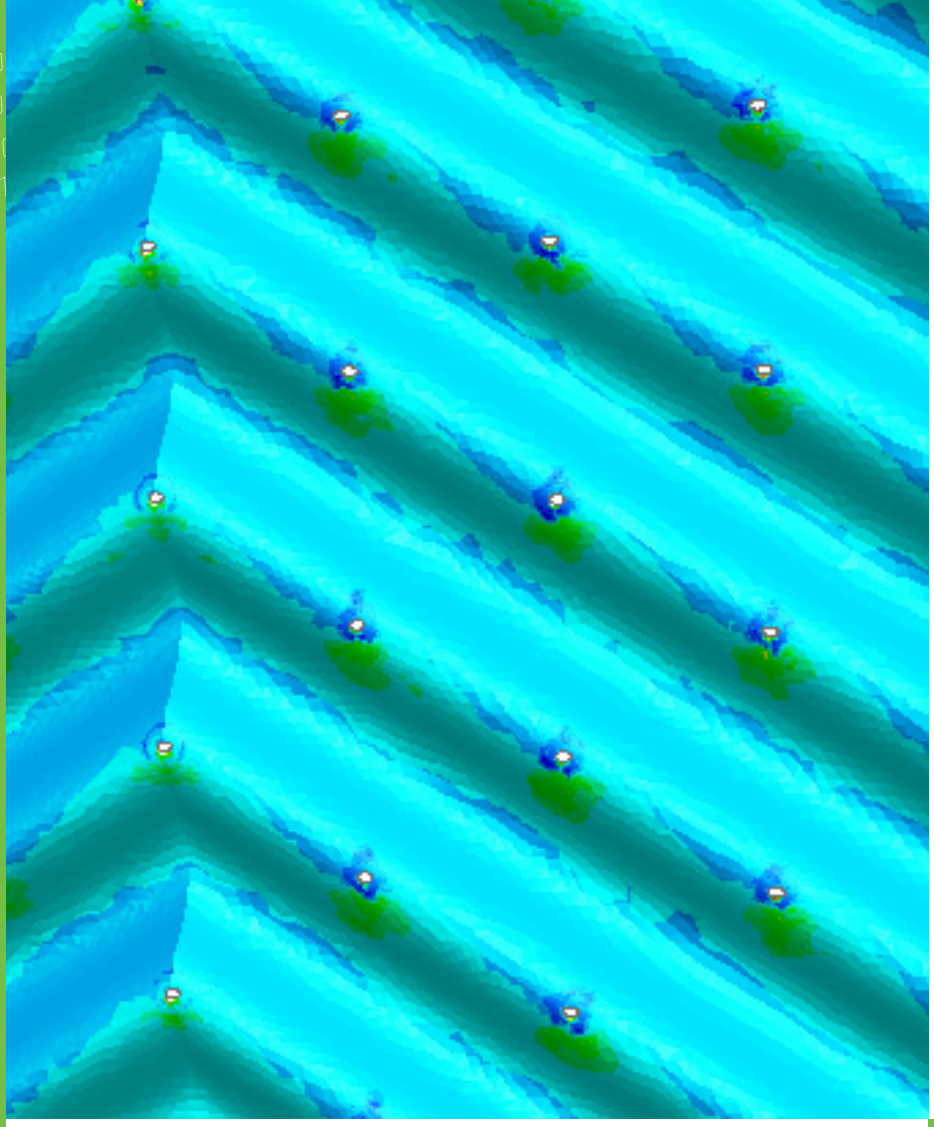

SCIENCE • TECHNOLOGY • RESEARCH HIGHLIGHTS • VISIONS •

Dissertation
88

Modelling particulate fouling in heat exchanger with high solid content liquid suspension

Ulla Ojaniemi

VTT

VTT SCIENCE 88

Modelling particulate fouling in heat exchanger with high solid content liquid suspension

Ulla Ojaniemi

Thesis for the degree of Doctor of Science (Department of Energy Technology) to be presented with due permission for public examination and criticism in Auditorium K215, at Aalto University, on the 21st of May, 2015 at 12.

ISBN 978-951-38-8250-1 (Soft back ed.)
ISBN 978-951-38-8251-8 (URL: http://www.vtt.fi/publications/index.jsp)

VTT Science 88

ISSN-L 2242-119X
ISSN 2242-119X (Print)
ISSN 2242-1203 (Online)

JULKAISIJA – UTGIVARE – PUBLISHER

Teknologian tutkimuskeskus VTT Oy
PL 1000 (Tekniikantie 4 A, Espoo)
02044 VTT
Puh. 020 722 111, faksi 020 722 7001

Teknologiska forskningscentralen VTT Ab
PB 1000 (Teknikvägen 4 A, Esbo)
FI-02044 VTT
Tfn +358 20 722 111, telefax +358 20 722 7001

VTT Technical Research Centre of Finland Ltd
P.O. Box 1000 (Tekniikantie 4 A, Espoo)
FI-02044 VTT, Finland
Tel. +358 20 722 111, fax +358 20 722 7001

Grano Oy, Kuopio 2015

Preface

The work for this thesis has been conducted within the projects of FOULSURFACE (MATERA ERA-NET, 2007–2009) and EFFIMAT (MATERA+, 2010–2013) at VTT Technical Research Centre of Finland Ltd. The project organizations are acknowledged for financially supporting the projects.

I would like to express my gratitude to all those people who have made this dissertation possible. The excellent work of coordinator Ph.D. Eini Puhakka made the projects successful. D.Sc.(Tech.) I am deeply grateful to Timo Pättikangas for his practical advice and great ideas. MSc. Markus Riihimäki from Oulu University is gratefully acknowledged for ideas and discussions and for providing the experimental work during the projects. Dr. Stein-Tore Johansen and Dr. Sverre Johnsen from SINTEF, Norway, are acknowledged for the useful discussions on the model development. Also MSc. Tiina Pääkkönen from Oulu University is thanked for the discussions. The working with all the collaborators has been very rewarding.

Most of all, D.Sc.(Tech.) Mikko Manninen, is acknowledged for the great work with the model development and supervising. He has extremely board experience with computational fluid dynamics. The excellent work of his made it possible to have such a great novel CFD model for particulate fouling.

I would like to acknowledge my supervising Professor Markku Lampinen who supported me to complete the work.

Most importantly, none of this would have been possible without the patience of my family. I gratefully express my warmest thanks to my husband, Juha, and my sons, Ville and Valtteri, for the endless source of support and strength all these years.

Espoo, April 2015
Ulla Helena Ojaniemi

Academic dissertation

Supervising professor, Custos	Professor Markku Lampinen Department of Applied Thermodynamics, Aalto University Espoo, Finland
Thesis advisor	Principal Scientist, D.Sc. (Tech.), Mikko Manninen VTT Technical Research Centre of Finland Ltd Espoo, Finland
Preliminary examiners	Adjunct Professor, Dr., Stein Tore Johansen NTNU, Dept. of Energy and Process Technology Tronheim, Norway Docent, D.Sc. (Tech.), Esa Muurinen University of Oulu Environmental and Chemical Engineering Oulu, Finland
Opponent	D.Sc. (Tech.), Jouni Pyykönen Espoo, Finland

Contents

List of symbols

Roman symbols

Symbol	Description	SI unit
A_H	Hamaker constant	J
C	Particle concentration	kg/m^3
C_0	Approximated particle concentration at wall	kg/m^3
C_D	Drag coefficient	-
D_B	Brownian diffusion coefficient	m^2/s
D_t	Turbulent diffusion coefficient	m^2/s
E	Young's modulus	Pa
$\mathbf{F}$	Force	N/m^3
$\mathbf{F_{a\tau}}$	Pull-off force, re-entrainment	N
$\mathbf{F_D}$	Drag force, re-entrainment	N
F_a	Faraday constant, 96485	C/mol
H_i	Sensible enthalpy of phase i	J
H_o	Minimum separation distance, 0.158	nm
I	Ion strength	mol/dm^3
J	Particle flux	$kg/(m^2 \cdot s)$
K_f	Deposition mass transfer coefficient	m/s
K_{pq}	Interphase momentum exchange coeff.	$kg/(m^3 \cdot s)$
R	Gas constant, 8.3144	$J/(K \cdot mol)$
Re	Reynolds number	-
Re_p	Particle Reynolds number	-
$\mathbf{S_p}$	Mass source term	$kg/(m^3 \cdot s)$
S_T	Soret coefficient	1/K
T	Temperature	K
a	Distance between surfaces	m
a	Acceleration	m/s^2
$c_{p,i}$	Specific heat capacity of phase i	$J/(kg \cdot K)$
d_p	Particle diameter	m
ds	Distance between wall and cell centre	m

f	Drag function	-
f_c	Correction factor for Stokes flow	-
f_r	Fraction of particles remaining on surface	-
$\dot{f}_r$	Fractional re-entrainment rate	1/s
h_i	Specific enthalpy of phase i	J/kg
k	Elastic constant	-
k_b	Boltzmann constant, $1.3807 \cdot 10^{-23}$	J/K
m	Mass	kg
q_W	Heat flux	kW/m^2
r_p	Particle radius	m
p	Re-entrainment rate	1/s
t	Time	s
u	Velocity	m/s
v_{sg}	Slip velocity due gravitation	m/s
u_τ	Friction velocity at the wall	m/s
y	Distance from surface	m
y^+	Dimensionless distance from surface	-
y_c	Distance of the cell centre from the wall	m

Greek symbols

Symbol	Description	SI unit
ϕ	Interaction energy in XDLVO theory	J
	Lognorm. distribution in re-entrainment	-
α_i	Volume fraction phase i	-
ε_0	Permittivity of vacuum, $8.854 \cdot 10^{-12}$	$C^2/(m \cdot J)$
ε_r	Relative permittivity	-
κ	Inverse of Debye length	1/m
λ	Decay length of water, 0.6	nm
λ_i	Thermal conductivity of phase i	W/(m·K)
μ	Dynamic viscosity	kg/(m·s)
ν	Poisson's ratio	m^2/s
	Kinematic viscosity	m^2/s
δ_D	Diffusion layer thickness	m
σ_t	Turbulent Schmidt number, 0.9	-
σ'	Standard deviation	-
ρ	Density	kg/m^3
τ_p	Particle relaxation time	s
γ-	Electron donor surface energy comp.	J/m^2
γ+	Electron acceptor surface energy comp.	J/m^2
$\dot{\gamma}$	Shear rate	1/s

γ	Free surface energy	J/m^2
ζ	Electrical surface potential	V

Indecies

Symbol	Description
AB	Lewis acid-base
LW	Lifshitz-van der Waals
a	Asperity
b	Bulk
diff	Diffusion
dr	Drift velocity
drag	Drag force
edl	Electrical double layer
exp	Expected value
lift	Lift force
m	Mixture
p	Particle
q	Liquid
s	Surface
slip	Slip between phases
t	Turbulent
tb	Turbophoresis
th	Thermophoresis
vdw	van der Waals

List of Abbreviations

ASM	Algebraic Slip Mixture model
CC	Constant surface Charge
CFD	Computational Fluid Dynamics
CFL	Courant number
CHE	Corrugated plate Heat Exchanger
CP	Constant surface Potential
CPU	Computational Power Used
DI	Derjaguin Integration
DLVO	Derjaguin, Landau, Verwey, Overbeek
EWT	Enhanced Wall Treatment
LES	Large Eddy Simulation
LSA	Linear Superposition Approximation

ODEs	Ordinary Differential Equations
PBE	Poisson-Bolzman Equation
RANS	Reynolds-averaged Navier Stokes
RMS	Root Mean Square
RnR	Rock'n'Roll
SEI	Surface Element Integration
SGM	Sub Grid Model
UDF	User Defined Functions
WALE	Wall-Adapting Local Eddy-Viscosity
Wf	Wall function approach
XDLVO	Extended DLVO

1. Introduction

1.1 Fouling

Undesirable deposition formation causes problems in severe branches of industries, especially in the chemical process industry. In recent years, the interest on the fouling of heat exchangers has increased due to the costs associated to the fouling: maintenance costs, downtime and overdesign of the equipment. The fouled layers lead to the increase in thermal resistance and therefore to a decreased efficiency of the heat exchanger. The status of fouling research during 50 years has been reviewed in publication by Müller-Stainhagen (2011). The estimated fouling costs are about 0.2% of the Gross National Product of countries. Therefore, for the designing of the heat exchangers, the knowledge obtained from the modelling is valuable. In addition, the fouling trends varying with operation conditions and time are needed in order to determine the feasible cleaning periodic of the equipment.

Fouling is a complicated phenomenon categorized by the dominant process inducing the accumulation of deposits: crystallization, particulate, chemical reaction, corrosion and biological fouling (Andritsos and Karabelas, 2003). Usually the deposits consist of more than one material. Crystallization is one of the most dominant and the most commonly investigated fouling process. However, suspended solids are present in numerous industrial processes.

Particulate fouling has been largely investigated experimentally with non-crystallizing materials by e.g. Yiantsios and Karabelas (2003) and by Grandgeorge *et al.* (1998). Several experimental studies of the suspended particles of crystallizing materials have been presented. Calcium carbonate, $CaCO_3$, is one of the most studied compounds forming the deposits of inverse-solubility salts. The effect of calcite particles on the fouling of a plate heat exchanger has been experimentally studied by Karabelas (2002) and Andritsos and Karabelas (2003). In their experiments, the increasing effect of colloidal calcite particles on fouling rate was evident. The particles of non-crystallizing materials did not have the same effect on the deposition rate. Deposition rate is the mass of foulants deposited on the wall per unit of time and per area.

In general, opposite to the tenacious layers due scaling, the deposits due to the fouling of suspended particles are more easily removed from the surfaces. With

submicron size particles, severe particulate fouling problems arise more often in processes, because the importance of colloidal interaction forces increases and more effort is needed for the particle removal from the surface (Andritsos and Karabelas, 2003).

1.2 Background

The particulate fouling can be considered as a serial process of transportation into the vicinity of the wall, adherence on the surface and re-entrainment as proposed by Epstein (1997). Models for deposition of aerosols have been widely presented in the literature. For colloidal particles suspended in liquids, the amount of detailed models available is smaller. Eulerian models have been presented by Guha (1997, 2008) for aerosol particles transference to the wall. Adomeit and Renz (1996) and Yiantsios and Karabelas (2003) have applied Eulerian method for modelling particulate fouling in liquid. The Eulerian-Lagrangian formulation was applied in the deposition model developed by Maniero and Canu (2006) and Henry *et al.* (2012). The Lagrangian computation consisting of tracking of trajectories of very large number of particles is not effective method in practical simulation cases.

The presented papers in literature were mainly focused on modelling the particle transport to the wall. The modelling of adhesion has gained less attention in the developed models for computational fluid dynamics, CFD. The attachment of the particles has been modelled based on e.g. empirical coefficient (2003) or sticking probability (Eskin *et al.*, 2011). The adhesion of the particles on the wall is controlled by colloidal interaction forces, like molecular forces and DLVO (Derjaguin, Landau, Verwey, and Overbeek) forces. The DLVO force appears between charged solid bodies interacting through a liquid medium. In the models developed by Adomeit and Renz (1996) and Henry *et al.* (2012) the adhesion on the wall surface was modelled based on DLVO theory.

DLVO theory has known to predict zero-values for deposition in repulsive conditions, although based on the experimental studies the fouling has been detected (Henry *et al.*, 2011). The overestimation of interaction energy predicted by DLVO theory is corrected more often by taking into consideration the surface roughness and heterogeneity of surface charges or by taking into account the acid-base interactions (XDLVO). The XDLVO theory is generally accepted in the aqueous colloidal systems (Bower *et al.*, 2010). However, the interaction energy predicted by the XDLVO has been found to be overestimated in the near surface region under the distances of few nanometers (Bower *et al.*, 2010).

1.3 Scope and objectives

The work is concentrated on the modelling colloidal particles fouling in the heat exchangers, where the high concentration of suspended calcite particles is present.

The object for developing a CFD model for the particulate fouling were

i. to have a model based on parameters taken from literature or experiments
ii. the model was aimed to be applicable in practical sized heat exchangers
iii. estimate the effect of the applied materials on the particulate fouling rate.

The work was comprised of the following sub tasks:

- The magnitude and interaction region of the forces affecting on the colloidal particles transport in to the heated wall were studied in order to determine the relevant forces affecting on the particulate transport in the near wall region. For that purpose, all the relevant near-wall forces affecting the particles were included into a detailed CFD fouling model, which was applied for a fouling test apparatus simulation with an extremely fine mesh near the fouling surface.
- The adhesion of the particles on the surface was modelled with XDLVO theory. The sensitivity of XDLVO theory on the process parameters was examined. The effects of chemical heterogeneity of the surface and the surface roughness on the fouling rate were examined.
- A correction for the XDLVO theory was applied on the basis of the models of Podgornic *et al.* (1987) and Teschke *et al.* (2001). The electric field due to the double layer formed near the surface effects on the polarization of the water based solution. Therefore, the water permittivity near the surface is changed, and that effects on the double layer thickness.
- A wall function approach was derived. The approach allows much larger near-wall cell, and therefore decreases the computational effort dramatically. The numerical models were tested for an experimental setup with several mass fractions of colloidal $CaCO_3$ particles, mass flows and heat flows. The applicability of the fouling model for comprising the effect of process conditions was examined.
- For including the effect of thermophoresis, the wall function approach was further developed to include also the temperature profile. The models presented in literature for the Soret coefficient of charged, spherical colloid in liquid were studied.
- The shear stress is the major effect in particle re-entrainment implying that the realistic modelling of turbulence is essential. Therefore, the CFD simulations of a test heat exchanger in 3D were performed with

Large Eddy Simulation (LES) and compared to the results calculated with standard k-ε model with Enhanced Wall Treatment (EWT). The applicability of the low Reynolds number turbulence model of Yang and Shih (1993) was tested.

- As a practical case, the wall function approach was applied in the modelling of industrial corrugated heat exchanger equipment with extremely high solid content slurry. The viscosity behavior of high solid content solution is non-Newtonian. The model for the non-Newtonian viscosity was derived from the experiments and implemented into CFD code. The effect on the fouling rate was examined.
- The effect of surface roughness and surface energy on the particle re-entrainment was studied with the models presented in literature. The re-entrainment model of Vainshtein *et al.* (1997) was modified for the CFD application. The CFD simulation with the practical sized heat exchanger was carried out in order to evaluate the effect of the surface energy on the fouling rate.

2. Description of the particulate fouling

2.1 Transport of the particles into the near wall region

The particulate fouling can be considered as a serial process of transportation of particles into the vicinity of the wall, adherence on the surface and re-entrainment (Epstein, 1997). The treatment of separate subprosesses is commonly justified with the comparison of the length scales of the forces. The length scales of hydrodynamic forces effecting on the movement of the particles are larger compared to the colloidal interaction forces causing the adherence on the wall, that are typically order of tens of nanometres (Elimelech and O'Melia, 1990).

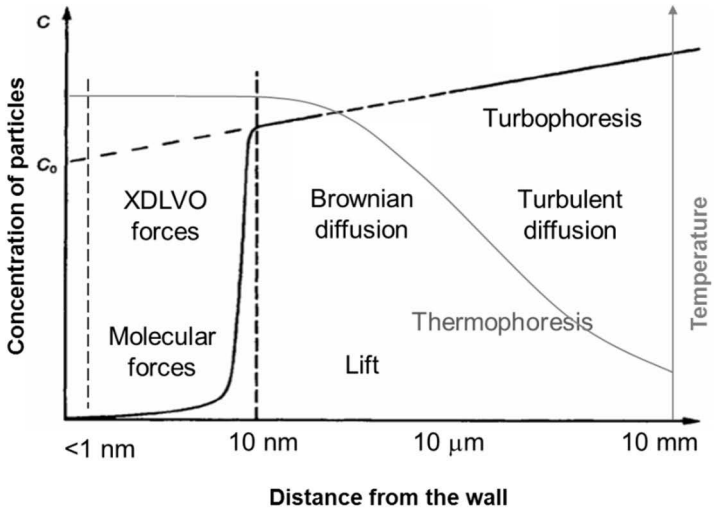

Figure 1. Schematic overview of the interaction region of the forces effecting on the particulate transport.

In the near-wall region, the particle transport is controlled by diffusion and convection (Elimelech and O'Melia, 1990). The dominating forces and mechanisms in transporting the colloidal particles were accounted. The considered forces were force due to Brownian and turbulent diffusion $\mathbf{F}_{\mathbf{diff}}$, drag $\mathbf{F}_{\mathbf{drag}}$, lift $\mathbf{F}_{\mathbf{lift}}$, thermophoretic $\mathbf{F}_{\mathbf{th}}$ and turbophoretic force $\mathbf{F}_{\mathbf{tb}}$. Interaction region of the forces are presented in schematic overview in Figure 1. In addition, the near wall colloidal forces, i.e. XDLVO and molecular forces, affecting on the adherence are described.

In Sections from 2.1.1 to 2.1.4, the forces affecting the particulate transporting are described and the models applied are presented, and the significance is discussed. In addition, the significance of the forces on the colloidal particle transporting is considered in the Section 6.1.2 with simulated results. The method for including the effect of the short range forces between the wall and particle into the particle concentration in the near wall region is presented in Section 2.2. In Section 2.3, the XDLVO theory applied in particle adhesion on the wall is described. Once adhered on the surface the particle re-entrainment might occur. The model applied for the re-entrainment is described in the Section 2.4. In addition, the effects of the surface heterogeneity and roughness are discussed in Sections 2.5 and 2.6.

2.1.1 Diffusion and drag force

For modelling the diffusion velocity $\mathbf{u}_{\mathbf{diff}}$, the generally applied Fick´s law is used and the force (per unit volume) acting on particles is modelled with

$$\mathbf{F}_{\mathbf{diff}} = K_{pq}\mathbf{u}_{\mathbf{diff}} = -K_{pq}D_{diff}\nabla\alpha_p \tag{2.1.0}$$

where the diffusion coefficient D_{diff} based on Brownian diffusivity D_B, and turbulent diffusivity D_t is given by

$$D_{diff} = D_B + D_t \text{, where } D_B = \frac{k_b T}{3\pi\mu_q d_p} \text{ and } D_t = \frac{\nu_t}{\sigma_t}. \tag{2.1.1}$$

Here σ_t = 0.9 the turbulent Schmidt number, $\alpha_{p/q}$ is the volume fraction of particle/liquid phase, μ_q is the liquid dynamic viscosity, ν_t the kinematic turbulent viscosity, k_b the Boltzmann constant, T the fluid temperature and d_p the particle diameter. K_{pq} is the interphase momentum exchange coefficient. In general form, the coefficient K_{pq} is written as

$$K_{pq} = \frac{\alpha_p \rho_p f}{\tau_p} \tag{2.1.1A}$$

where τ_p is the particle relaxation time given as

$$\tau_p = \frac{\rho_p d_p^2}{18\mu_q} \tag{2.1.1B}$$

and the drag function f is defined as

$$f = \frac{C_D \, \mathrm{Re}_p}{24} \tag{2.1.1C}$$

The drag coefficient C_D is most often based on the particle Reynolds number $Re_p=\rho \mathbf{u} d_p/\mu_q$. For the drag coefficient C_D, there are numerous models presented in literature. In modelling the forces due to diffusion, and further due to drag and thermophoresis, the drag coefficient is calculated according to Wen and Yu (1966) (Fluent, 2009).

As presented in Figure 1, for colloidal particles, Brownian diffusion dominates over turbulent diffusion in the near wall region, while the turbulent transport is predominant within the turbulent core. Brownian diffusion is proportional with the temperature, equation (2.1.1), therefore in the near wall region of the heated wall, the velocity due to the Brownian diffusion is increased.

Drag force is experienced by a particle moving through a fluid and it is proportional with the velocity difference between the phases

$$\mathbf{F_{drag}} = -K_{pq}\mathbf{u_{slip}}, \tag{2.1.2}$$

where $\mathbf{u_{slip}} = \mathbf{u_p} - \mathbf{u_q}$.

2.1.2 Lift force

The particle transport in the shear flow is affected by hydrodynamic lift force caused by particle rotation due to pressure distribution developed on a particle in a velocity gradient. The lift force is perpendicular to the direction of the flow. The implemented lift force is the general expression for the Saffman force extended to three dimensional flows (Crowe *et al.*, 1998)

$$\mathbf{F_{lift}} = 1.61 d_p^2 \sqrt{\frac{\mu_q \rho_q}{|\omega_q|}} \left[\left(\mathbf{u_q} - \mathbf{u_p} \right) \times \omega_q \right], \qquad (2.1.3)$$

where $\omega_q = \nabla \times \mathbf{u_q}$.

The effect of the lift force has been reported to be insignificant for the colloidal particles (Adomeit and Renz, 1996). It has been shown that with the condition $d_p u_\tau / \nu < 1$ with friction velocity u_τ, the drag force dominates over lift force (Ziskind *et al.*, 1998). Therefore, in the tested case of liquid suspension with colloidal particles, the lift force is assumed to be insignificant. The model of Crowe *et al.* (1998) was tested in order to evaluate the effect of lift force in the fouling rate.

2.1.3 Thermophoresis

Thermophoresis is a phenomenon of mass transport in a temperature gradient, and it is described with Soret coefficient S_T. Near the heated surface, the temperature gradient is larger compared to the gradient further away from the surface. Thus, the thermophoresis is present mostly in the near wall region. The thermophoretic force has been studied largely in the aerosol systems during recent decades. In liquids, the thermophoresis has been examined with a variety of solvents – particulate systems, but still there is a lack of generally accepted theory (Putnam *et al.,* 2007; Würger, 2009). The thermophoretic mobility of charged particles has been reported to be largely determined by the electrolyte solution (Würger, 2009; Semenov and Schimpf*,* 2011).

Most often the models for Soret coefficient S_T are based on a single particle theory, and the particle-particle interactions are not included. It has also been found that the thermal diffusion can have different signs in different environments, i.e. the direction of the force may be towards the wall or away from the wall. The sign of the coefficient in the model of Semenov and Schimpf (2011) was explained by the dominating contribution of electrostatic interaction in a double layer or Hamaker interactions of the suspended colloid particle. Würger (2009) proposed the temperature dependence of the sign of Soret coefficient to arise from thermoelectric contribution. Several studies of the nanoparticle suspensions have shown similar particle behavior: particles are moving towards the hot wall when the bulk temperature is low, e.g. below 293K (negative coefficient) and towards the cold side if the bulk temperature is more than 303 K (Putnam *et al.*, 2007, Würger, 2009).

For calculating the thermophoretic force in a liquid, a few models are available in the literature. Some of the presented models for Soret coefficient S_T for charged colloids in liquid were examined (Ojaniemi *et al., 2013)*. Figure 2 shows the Soret coefficients as a function of temperature predicted by several models from literature: Parola and Piazza (2004), Putnam *et al.* (2007), Dhont *et al.* (2007), Würger

(2009) and Semenov and Schimpf (2011). The models presented result in a wide range of values, as seen in Figure 2.

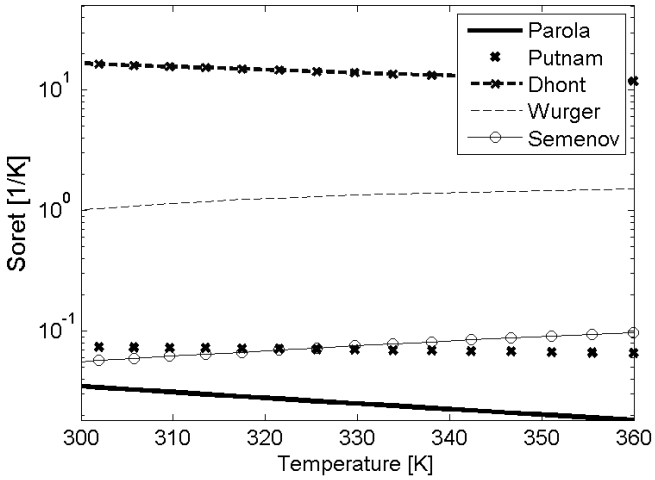

Figure 2. Soret coefficients predicted with several models, 1/K (Ojaniemi *et al.,* 2013).

Several models were chosen for further study with particulate CFD fouling model in order to evaluate the magnitude of the thermophoresis in comparison to the other forces affecting particle transport (Ojaniemi *et al.,* 2013*)*. The results are shown for the models Parola and Piazza (2004), Putnam *et al.* (2007) and Würger (2009). The modelled coefficients are taken positive due to the bulk temperature 333 K applied in the experiments, i.e. thermophoresis has been considered as cleaning mechanism.

Parola and Piazza (2004) have proposed for the charged colloids the following form of the Soret coefficient for coupling the heat and mass transfer in liquids

$$S_{T\_PP} = \frac{\varepsilon_r \varepsilon_0 d_p}{2 k_b T^2} \zeta_p^2 \qquad (2.1.4)$$

where ζ_p is the electrical surface potential of the spherical $CaCO_3$ particle, and ε_0 and ε_r are the dielectric permittivity of vacuum and the relative permittivity of water.

In the model of Putnam *et al.* (2007), the model of Anderson is approximated with the electric field of flat double layer. The model of Anderson is based on the Derjaguin model of the thermo-osmosis of an electrolyte in a porous medium. Anderson then derived the model to describe the thermophoresis of the particles in liquids. In the modified model of Putnam *et al.* (2007), the electrostatic field due

to the polarization of water molecules in the double layer is included into the model resulting in

$$S_{T\_P} = \frac{3\pi d_p}{4k_b T^2}\left(1+\frac{\lambda_p}{2\lambda_q}\right)^{-1}\left(\varepsilon_r\varepsilon_0 + T\frac{\partial(\varepsilon_r\varepsilon_0)}{\partial T}\right)\zeta_p^2 \tag{2.1.5}$$

with the restrictions $\zeta \leq 2\, k_b T / e$ and $\kappa d_p / 2 >> 1$. λ_p and λ_q are the thermal conductivities of particle and liquid.

Würger (2009) has proposed that for the charged colloids in aqueous solutions the electric forces dominate in comparison to the dispersion forces, i.e. van der Waals interaction and thermal expansivity of the solution. The model for the Soret coefficient including the electrostatic forces is thus

$$S_{T\_W} = \frac{\varepsilon_r\varepsilon_0\zeta_p}{\mu_q T}\left(\frac{\zeta_p}{3} - \delta\alpha\,\frac{k_b T}{e}\right)D_B^{-1} \tag{2.1.6}$$

where thermoelectric coefficient $\delta\alpha(T) = 0.8 + 0.025K^{-1}(T - 298K)$ and e is the electron charge. The first term accounts for the flow of the electric energy density in the temperature gradient, and the second term results from the thermoelectric field.

The thermophoretic force acting on the particle is modelled as

$$\mathbf{F_{th}} = K_{pq}\mathbf{u_{th}} \tag{2.1.7}$$

where the velocity of the particle is given by

$$\mathbf{u_{th}} = -D_B S_T \nabla T \,. \tag{2.1.8}$$

2.1.4 Turbophoresis

Turbophoresis is caused by the interaction between the particle inertia and the inhomogeneity of the fluid turbulence field. The turbophoretic force $\mathbf{F_{th}}$ depends on the particle fluctuating RMS (Root Mean Square) velocity. If the RMS velocities of the fluid and the particles are of the same order, as they are for the colloidal size particles, the particles follow effectively the fluid flow, and the turbophoretic force is insignificant (Reeks, 1983; Guha, 1997). For the colloidal particle size consid-

ered in the test case, the magnitude of the turbophoretic force was evaluated to be negligible. Thus, the turbophoretic force was not included in the model.

2.2 Particle flux at the wall

The particle transport to the surface is calculated based on convective-diffusion equation including the Brownian diffusion, which is the dominating diffusion force in the near-wall region. The colloidal particles transportance is affected by the particle-wall interaction energy and the reduced mobility of the particle. If the repulsion due to the colloidal forces in the near wall region is insignificant, and the attractive forces are dominating, the deposition of particles is calculated with convective-diffusion equation considering a perfect sink at the wall surface, and the particle concentration at the wall is vanishing. In a case of repulsive forces are affecting on the particle transportance, the particle concentration in the near wall region is not vanishing, and the electrical interaction energy between the surfaces of the particles and the wall determines the amount of deposited mass on the wall.

In the CFD model for the particulate fouling, the method of Spielman and Friedlander (1973) is used for incorporating the interaction energy into the calculation of particle flux at the wall (Grandgeorge *et al.,* 1998*)*. The deposition rate is calculated in this method from the electrical interaction potential barrier. The method is applicable to surfaces having charges of the same sign, i.e., in the presence of a repulsive force. The energy barrier, which is a secondary maximum, has to exist in the total interaction energy (Elimelech *et al.*, 1995).

The concentration distribution for the colloids in a fluid flowing on a flat surface can be modelled according to Spielman and Friedlander (1973) with

$$\frac{\partial}{\partial y}\left(D_B \frac{\partial C}{\partial y} + \frac{C D_B}{k_b T} \frac{\partial \phi_{tot}}{\partial y} \right) = 0 \qquad (2.2.0)$$

where *y* is the distance from the surface and D_B is the Brownian diffusion coefficient. The interaction energy ϕ_{tot} in equation (2.2.0) due to the electrostatic forces (see equation (2.3.6)), is the external force acting on the particles and it is assumed to be a function of distance from the surface only.

The equation (2.2.0) is valid for the laminar flow. However, the electrostatic forces considered here are present in a near wall region. Therefore, when considering the turbulent flow, the forces are in the region of viscous layer, and the flow is close to the laminar flow (White, 1991). Therefore, the developed method for modelling the deposition rate can be considered valid also for the turbulent flow.

The particle flux J to the wall at the point x can be obtained by integrating equation (2.2.0) once, and assuming a perfect sink at the wall, $C(y = 0) = 0$ (Spielman and Friedlander, 1973),

$$J(x) = D_B \frac{\partial C(y)}{\partial y} + \frac{D_B C(y)}{k_b T} \frac{\partial \phi_{tot}}{\partial y} = -D_B \frac{\partial C(y)}{\partial y}\bigg|_{y=0}. \quad (2.2.1)$$

By integrating equation (2.2.0) twice, the concentration of the particles is found (Spielman and Friedlander, 1973),

$$C(y) = -\frac{J(x)}{D_B} e^{-\phi_{tot}/k_b T} \left[\int_0^y \left(e^{\phi_{tot}/k_b T} - 1 \right) dy' + y \right]. \quad (2.2.2)$$

Since the total interaction energy ϕ_{tot} vanishes at distances much larger than the width of the electrical double layer ($y >> \kappa^{-1}$), the particle concentration reduces to (Spielman and Friedlander, 1973; Elimelech *et al.,* 1995)

$$C(y) = -\frac{J(x)}{D_B} \left[\int_0^{\delta_D} \left(e^{\phi_{tot}/k_b T} - 1 \right) dy' + y \right]. \quad (2.2.3)$$

In order to ensure the total interaction energy ϕ_{tot} equal to zero, the upper limit of the integration is set in here to the thickness of the diffusion layer, δ_D ($>>\kappa^{-1}$) (Elimelech *et al.,* 1995). Typically, the width of the electrical double layer κ^{-1},is of the order of several nanometres to tens of nanometres (see e.g. Figure 6). This is likely to be very thin in comparison with the thickness of the diffusion layer, δ_D (Spielman and Friedlander, 1973).

Convective transport is insignificant in the diffusion layer. In the limit of the diffusion layer, the diffusive transport equals the convective transport. Based on this, and taking the velocity profile linear in the near wall region, in fully developed channel flow the thickness of the diffusion layer $\delta_{D,}$ can be evaluated from (Probstein, 2013)

$$\frac{\delta_D}{x} \sim \left(\frac{h}{x} \right)^{2/3} \left(\frac{D}{u_{\max} h} \right)^{1/3} \quad (2.2.4)$$

In here, h is the channel half-width, D is diffusion coefficient, x is the distance from inlet and u_{max} is the fluid maximum velocity in the channel. Taking D_B for the diffusion coefficient and the channel width and maximum velocity from the test case described in Section 5, the thickness of diffusion layer is of order of tens of micrometres. Therefore, the determination $\delta_D >> \kappa^{-1}$ is valid.

The expected concentration profile near the surface according to equation (2.2.2) is presented in Figure 3. While the distance from the wall is large enough, $y>>\kappa^{-1}$, the total interaction energy ϕ_{tot} equals to zero, and the value for the integral in the equation (2.2.3) is constant. Therefore, at sufficiently large distances ($y>>\kappa^{-1}$), the concentration will be linear according to equation (2.2.3) (Spielman and Friedlander, 1973). By matching this linear portion with the convective-diffusion equation in the absence of colloidal forces, an approximate profile for the concentration can be obtained in the vicinity of the wall, see Figure 3.

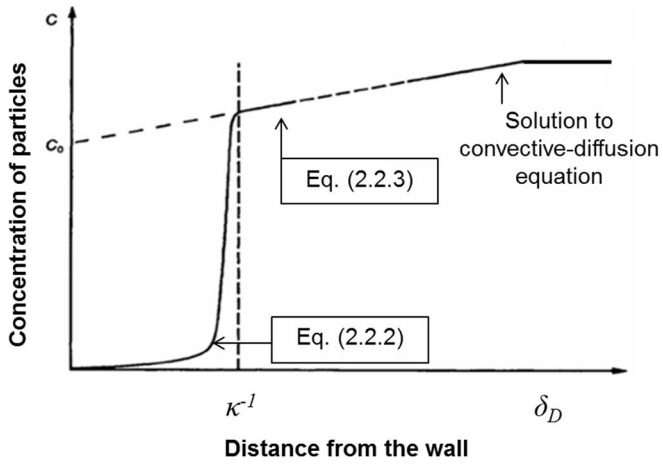

Figure 3. Schematic overview of the particle concentration profile in the near wall region (based on Fig. 2 presented in Spielman and Friedlander,1973). Order of thickness of κ^{-1} is several tens of nanometres, and thickness of δ_D is order of micrometres.

Spielman and Friedlander (1973) suggested that the matching procedure is equivalent to using the following boundary condition for the convective-diffusion equation:

$$C(y=0,x) = -\frac{J_0(x)}{D_B}\left[\int_0^{\delta_D}\left(e^{\phi_{tot}/k_bT}-1\right)dy'\right]. \qquad (2.2.5)$$

Here, the value $C(y=0,x)$ correspond with the value C_o in the Figure 3.

The approach of Elimelech *et al.* (1995) was used for modelling the reduction in particle mobility. The correction factor $g_1(H)$ was included into the model for the particle flux at the wall to account for the hydrodynamic interaction between the wall and the particle. The particle transport in the vicinity of the wall is affected by reduction of the particle mobility. Equation (2.2.3) is then replaced by (Elimelech *et al.,* 1995).

$$C(y) = -\frac{J(x)}{D_B}\left[\int_0^{\delta_D}\left(g_1(H)e^{\phi_{tot}/k_bT} - 1\right)dy' + y\right]. \qquad (2.2.6)$$

For the hydrodynamic correction factor $g_1(H)$, the model proposed by Warzynski (2000) has been applied

$$g_1(H) = \frac{19H^2 + 26H + 4}{19H^2 + 4H}, \qquad (2.2.7)$$

where $H=a/r_p$ is the distance between the surfaces normalized with the particle radius.

The boundary condition (2.2.4) for the convective diffusion equation is replaced with (Elimelech *et al.,* 1995)

$$C_0 = -\frac{J_0(x)}{D_B}\left[\int_0^{\delta_D}\left(g_1(H)e^{\phi_{tot}/k_bT} - 1\right)dy'\right]. \qquad (2.2.8)$$

Hence, the calculation of the deposition rate of Brownian particles in the presence of repulsive colloidal forces confined to a narrow zone in a near wall region has been reduced to solving the general convective-diffusion equation with the boundary condition (Spielman and Friedlander, 1973; Elimelech *et al.,* 1995)

$$J_0(x) = -K_f C_0 = -D_B \left.\frac{\partial C}{\partial y}\right|_{y=0}, \qquad (2.2.9)$$

where J_o is the local flux of the particles at the surface and K_f is a pseudo-first-order rate constant

$$K_f = D_B\left\{\int_0^{\delta_D}\left(g_1(H)e^{\phi_{tot}/k_bT} - 1\right)dy\right\}^{-1}. \qquad (2.2.10)$$

In a case the particle surface and the wall are of like charge, and the repulsion is dominating, the effective surface concentration is greater than zero. This implies that the deposition rate is decreased in comparison to the perfect sink due to the energy potential barrier in a narrow zone ($\sim\kappa^{-1}$) near the surface (Spielman and Friedlander, 1973).

The integral (2.2.10) for the mass transfer coefficient can be evaluated numerically. If the height of the potential barrier is larger than k_bT, the following approximation can be used: if the upper limit of the integral is large enough, the value of the integral does not depend on the upper limit (Elimelech *et al.,* 1995). Therefore, the arbitrary determination of diffusion layer thickness according to equation (2.2.4) is not needed as far as the upper limit of the integration is clearly smaller than the evaluated value for the layer thickness.

The integral (2.2.10) is dependent on temperature, but not on the fluid properties, and thus it can be determined as a function of temperature (see Section 4.1). However, if the turbulent diffusion is likely to take place in the region of integration, the equation (2.2.10) has to be considered to include the effective diffusion coefficient according to equation (2.1.1.) and cannot be determined as a function of temperature only.

2.3 Particle adhesion at the wall

2.3.1 DLVO theory

The adhesion of the particles on the wall surface is influenced by electrostatic forces. The particle – substrate interaction in the near wall region in aqueous medium is generally described with Derjaguin-Landau-Verwey-Overbeek (DLVO) theory of colloidal stability (Derjaguin and Landau, 1941; Vervey and Overbeek, 1948). The theory comprises the attractive van der Waals interactions and the electrostatic double layer interactions, which are repulsive for surfaces of like sign.

In literature, two main approaches are presented for calculating the van der Waals interaction energy: the microscopic and the macroscopic methods (Liang *et al.,* 2007). In the microscopic approach, the interaction energy between the bodies is assumed to be pairwise additive, thus the effect of the neighboring atoms in the bodies are ignored. In the macroscopic approach of the Lifshitz theory, the problem of additivity is avoided by treating the large bodies as continuous media and deriving the forces in terms of the bulk properties. The macroscopic method is valid for the cases with liquid medium and has been applied in this study.

While immersed in the liquid of high dielectric constant ε_r, the electrical layer is formed around the particle. On the particle surface, a charge is formed due to the ionization or dissociation of the surface groups, or due to adsorption of the ions from the solution. Therefore, the first of the double layers is formed by the charge in the particle surfaces. The second layer is formed by the excess of the oppositely charged ions in the solution. The layer extends over a certain distance from the particle surface vanishing gradually with increasing distance (diffuse layer).

As the two particles of like charged surfaces approach each other in the medium, the double layers start to overlap until the repulsive forces hiders the further overlapping. The response of the double layers on each other is in generally considered to be due to constant surface charge or due to constant surface potential (Elimelech *et al.*, 1995; Oliveira, 1997; Liang *et al.,* 2007). The method of the

constant surface potential (CP) corresponds to the maintenance of surface – chemical equilibrium at every point during the approach of the bodies. The constant potential can be assumed, if the surfaces are highly conducting (metallic) or the surface charge is determined by the adsorption of ions. Due to the impossibility of measuring, the surface potential is replaced with zeta potential ζ in the calculations. When the charged surface and adjacent electrolyte solution are in relative movement, a part of the double layer charge moves with the liquid. The plane separating the fixed part and the mobile part of the double layer is called a shear plane. The zeta potential is the electrokinetic potential at the plane of shear.

The constant charge (CC) implies that the charge density at the body surface remains fixed, irrespective on their separation distance. The assumption may be valid with the clay particle which has a certain ion exchange capacity and the surface charge is formed due isomorphic substitution. However, at the close separations, the assumption of constant charge is thermodynamically adverse due to the highly increased electric potential between the surfaces (Adamczyk and Werónski, 1999). In both methods, the size of the particle has to be much larger than the double layer thickness, $d_p >> \kappa^{-1}$.

For relating the averaged charge distribution and the electrical potential energy in the double layer between two plane surfaces, the non-linear Poisson-Boltzmann equation (PBE) is applied (Elimelech *et al.*, 1995). The analytical solution of the interaction energy for spherical particle systems is usually not possible. For constructing approximations, the analytical and numerical solutions for the known expressions, typically for plates, are applied. The expression for the interaction energy can be obtained with Derjaguin summation approach or with linear superposition approximation (LSA).

In the method of LSA, it is assumed that a region exists between the two interacting surfaces where the potential is sufficiently small and obeys the linearized PB equation. Contributions from each surface can be added to give an overall potential. In a vicinity of each surface the potential is assumed to be due to that surface alone. The approach is valid only, if the separation distance >> double layer thickness κ^{-1} (Elimelech *et al.*, 1995).

In Figure 4, the interaction energy between the wall surface and particle is presented. The energy is calculated with the three different methods (Elimelech *et al.*, 1995): constant charge, constant potential and LSA. The interaction energy results have been calculated for a clean, smooth stainless steel surface and for colloidal, spherical calcite particles in water. For the zeta potential of the particles, the value of –25 mV from Riihimäki *et al.* (2010) was applied. For the steel surface, the value –25 mV was applied (Boulangé-Petermann *et al.*, 1995). For the ion strength, the value evaluated from the test fluid used in the experiments based on the conductivity measurement and chemical analysis was applied, see Table 6. The potential energy is expressed in units k_bT which is comparable to the particle energy under Brownian motion (Elimelech *et al.*, 1995).

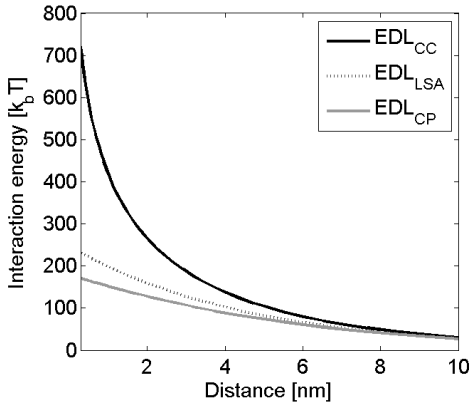

Figure 4. Interaction energy of electric double layers between wall surface and particle as a function of separation distance at temperature 345 K. Models of constant charge, CC, constant potential, CP, and LSA are applied. For particle and wall surface the zeta potential is –25 mV.

The values for the surface energy parameters used in calculation of the results shown in Figure 4 were taken from the literature, see Table 1. The surface energy γ is the energy needed in forming a new surface when splitting the material or forming a droplet; it is a measure of the strength of interatomic forces (Bhushan, 2013). In generally, γ is called free surface energy for solids, and surface tension for liquids. The values for liquids are determined with wetting experiments, and they are typically of the order of few tens of mJ/m^2, see Tables 1 and 4

Table 1. Surface energy parameters for the DLVO theory.

	Water, [1] mJ/m^2	Stainless steel [2] mJ/m^2	$CaCO_3$ [3] mJ/m^2
Non-polar component, γ^{LW}	21.8	42.8	26.7
Electron donor, γ^-	25.5	11.5	28.4
Electron acceptor, γ^+	25.5	2.0	2.0

1) Van Oss, 2006, in temperature of T=293 K
2) Santos *et al.*, 2004, AISI 316L
3) Wu *et al.*, 1996

The dynamic aspects of the double layer interaction are not fully understood. The considerations of the constant charge or constant potential comprise the phenomena at the surface of the bodies, but the interaction between the double layers depend on the potential at the Stern layer, in where the response time for equilib-

rium is more rapid. Therefore, neither of the extreme assumptions of the constant charge, CC, or the constant potential, CP, is likely to be applied in practice (Elimelech *et al.*, 1995; Liang *et al.,* 2007). The LSA method might be the most convenient method to apply. However, the method is not applicable in the short separation distances.

The method of constant potential, CP, is applied in further studies: The particle size in the study is larger than double layer thickness, and the near wall phenomena are to be studied. In addition, the method of CP has been most widely examined in literature. Both the LSA and CC methods have been shown to be inaccurate at short separation distances (Elimelech *et al.*, 1995).

2.3.2 XDLVO theory

DLVO theory has known to predict zero-values for deposition in repulsive conditions, although based on the experimental studies the fouling has been detected (Henry *et al.*, 2011). The overestimation of interaction energy predicted by DLVO theory is corrected often by taking into consideration the surface roughness and heterogeneity of surface charges. While taking into account the non – DLVO interactions arising e.g. from acid-base interfacial forces, the DLVO forces are lowered by two decades of magnitude. Addition of non – DLVO forces into DLVO interaction theory is referred as 'extended – DLVO' or XDLVO approach. In Table 2, the generally accepted equations of XDLVO theory applied in here in a case of sphere-flat surface are presented (Hoek and Agarwal, 2006; van Oss, 2006).

In Table 2, eq. (2.3.0) presents the unretarded Lifshitz – van der Waals (*vdw*) interaction potential. A_H, equation (2.3.1), is the particle – substrate Hamaker constant presented with Lifshitz – van der Waals free energy (LW) per unit area at a minimum contact between wall surface and particle interacting in water. H_O is the minimum separation distance due to Born repulsion, and a is the separation distance between the surfaces.

The interaction potential due electrostatic double layer (*edl*) is presented with equation (2.3.2). The Debye screening length, κ^{-1}, presented with equation (2.3.3), is the effective thickness of the double layer. ζ_p and ζ_s are the surface potentials of the particle and wall surface, and ε_0 and ε_r are the dielectric permittivity of vacuum and the water relative permittivity.

The polar interactions are included with the equation (2.3.4). Polar interactions are defined to comprise all electron-acceptor – electron-donor (or Lewis acid-base, AB) interactions (van Oss, 2006). The polar free energy per unit area between the nanoparticle and wall surface at the minimum contact is described by equation (2.3.5**)**. λ is the decay length for polar interactions in water, and γ is the surface energy component.

Table 2. Equations for the XDLVO theory.

Lifshitz-van der Waals attractive interaction potential, sphere-plate (van Oss, 2006)

$$\phi_{vdw} = -\frac{A_H d_p}{12a} \tag{2.3.0}$$

$$A_H = 24\pi H_0^2 \left(\sqrt{\gamma_1^{LW}} - \sqrt{\gamma_3^{LW}}\right)\left(\sqrt{\gamma_2^{LW}} - \sqrt{\gamma_3^{LW}}\right) \tag{2.3.1}$$

The electrical double layer interaction potential (Oliveira, 1997)

$$\phi_{edl} = \varepsilon_r \varepsilon_0 \pi \cdot \frac{d_p}{2} \cdot \left[\left(\zeta_s + \zeta_p\right)^2 \ln\left(1 + e^{-\kappa a}\right) + \left(\zeta_s - \zeta_p\right)^2 \ln\left(1 - e^{-\kappa a}\right)\right] \tag{2.3.2}$$

$$\kappa^{-1} = \left(\frac{\varepsilon_r \varepsilon_0 RT}{2F_a{}^2 I \cdot 10^3}\right)^{1/2} \tag{2.3.3}$$

Lewis Acid-base interaction energy (van Oss, 2006)

$$\phi_{AB} = \pi\lambda d_p \Delta G_{H_0}^{AB} \exp\left(\frac{H_0 - a}{\lambda}\right) \tag{2.3.4}$$

$$\Delta G_{H_0}^{AB} = 2\sqrt{\gamma_3^+}\left(\sqrt{\gamma_1^-} + \sqrt{\gamma_2^-} - \sqrt{\gamma_3^-}\right) + 2\sqrt{\gamma_3^-}\left(\sqrt{\gamma_1^+} + \sqrt{\gamma_2^+} - \sqrt{\gamma_3^+}\right) - 2\left(\sqrt{\gamma_1^+\gamma_2^-} - \sqrt{\gamma_1^-\gamma_2^+}\right) \tag{2.3.5}$$

Adhesion is determined by the balance between the attractive and repulsive forces. According to XDLVO theory, the balance is calculated as a total sum of the interaction potentials obtained from equations (2.3.0), (2.3.2) and (2.3.4)

$$\phi_{tot} = \phi_{vdw} + \phi_{edl} + \phi_{AB}. \tag{2.3.6}$$

2.3.3 Modified XDLVO theory

The XDLVO theory has been successful in aqueous systems but found to result in too high values of interaction energy within a region of few nanometres from the surfaces (Bower *et al.,* 2010). By incorporating the effect of the electric double layer on the water permittivity, the values of estimated interaction energy with the XDLVO theory decreased. When the electrical double layer is formed in the proximity of the solid bodies, the electric field formed near the surface affects the polarization of the medium, e.g., water. This changes the water permittivity. The shape of the permittivity function depends on the distance *y* from the surface according to (Podgornik *et al.*, 1987)

$$\varepsilon_{r,DL}\left(y\right)=\varepsilon_{r,\max}\left[1+\left(\varepsilon_{r,\max}/\varepsilon_{r,\min}-1\right)\exp\left(-2\kappa y\right)\right]^{-1} \tag{2.3.7}$$

According to Teschke *et al.* (2001), the minimum permittivity $\varepsilon_{r,min}$ = 4 at the solid surface. The maximum permittivity $\varepsilon_{r,max}$ is the permittivity of the bulk, which is calculated as temperature dependent (Handbook of Chemistry and Physics, 1998)

$$\varepsilon_{r,\max}=5321T^{-1}+233.76-0.9297T+0.1417\times10^{-2}T^{2}-0.8292\times10^{-6}T^{3} \tag{2.3.8}$$

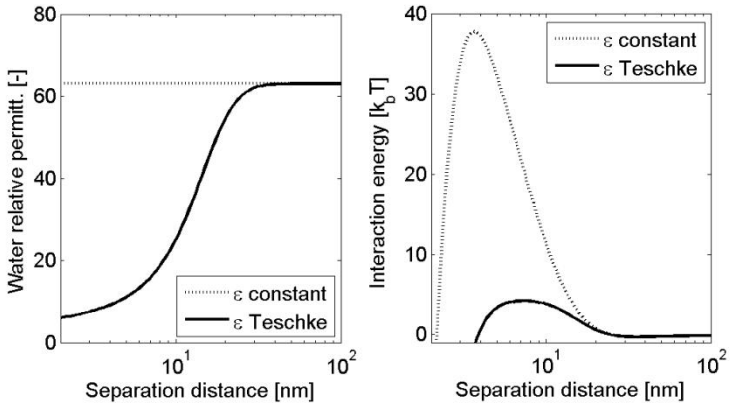

Figure 5. On the left: The relative permittivity of water obtained from the model of Teschke *et al.* (2001) compared to the bulk value of the permittivity at temperature 345 K. On the right: Interaction energy between the calcite particle and steel surface modelled with the XDLVO theory applying the constant value and the model of Teschke *et al.* (2001) for relative permittivity of water at temperature 345 K (Ojaniemi *et al.,* 2012*)*.

The relative permittivity of water calculated according to equation (2.3.8) is shown in Figure 5, where it is compared to the constant value at T=345 K. Figure shows also the effect of the decreased permittivity of the water near the surface on the interaction energy (Ojaniemi *et al.,* 2012*)*.

As shown in Figure 5, the interaction energy between the surfaces is decreased significantly while taking into account the decreased permittivity near the surface. The values used in Section 2.3.1 in calculation of interaction potential between the wall surface and particle has been applied in calculating the results in Figure 5. If the constant bulk value for the water permittivity would be used instead of the model of Teschke *et al.* (2001), a smaller fouling rate would be obtained.

2.3.4 Adhesion sensitivity of the XDLVO parameters

Analysis of the particle adhesion response to the model parameters showed that the total interaction energy obtained from equation (2.3.6) is very sensitive to the ion strength of the fluid and to the size of the particle. In Figure 6, the total interaction energy is shown as calculated with three ion strengths and two particle sizes. The smaller the particle and the higher the ion strength, the lower energy is needed for the particle to get over the energy barrier near the wall surface. The electrostatic forces between the particles are influenced by salt content of the fluid and the zeta potential and the Debye length κ^{-1} decrease with increasing ionic strength. Both of these effects decrease the repulsion force (Elimelech *et al.,* 1995). Thus, the energy barrier near the wall is reduced and the fouling can take place more easily. The particle which is captured by the primary minimum of the potential near the wall is strongly adhered on the wall. For the greater particles, a deeper secondary minimum is formed. From the secondary minimum, the particle re-entrainment by hydrodynamic forces is easier.

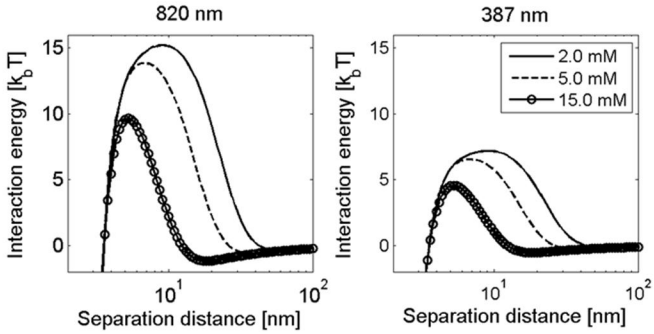

Figure 6. Interaction potential between spherical $CaCO_3$ particle and clean, stainless steel surface with three ion strengths: Solid line –2.0 mmol/l, dashed line –5.0 mmol/l, circle-dashed line –15.0 mmol/l. Two particle sizes are shown, 387 nm and 820 nm. For particle and wall surface the zeta potential is –25 mV (Ojaniemi *et al.,* 2012*)*.

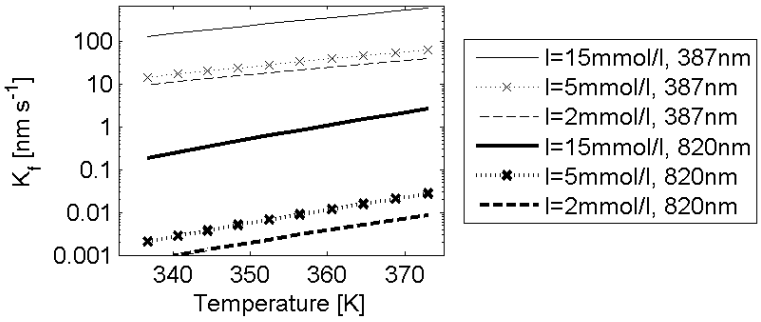

Figure 7. Mass transfer coefficient as a function of wall surface temperature. Smooth, clean steel surface and spherical calcite particle were considered, with zeta potential of –25 mV (Ojaniemi *et al.,* 2012*)*.

The mass transfer coefficients calculated from equation (2.2.10) for the cases shown in Figure 6 are presented in Figure 7 as a function of temperature. In practice, the larger particle is adhered on the surface only if the ion strength is high. For smaller particle size, fouling occurs even in the slurry of lower ion strength.

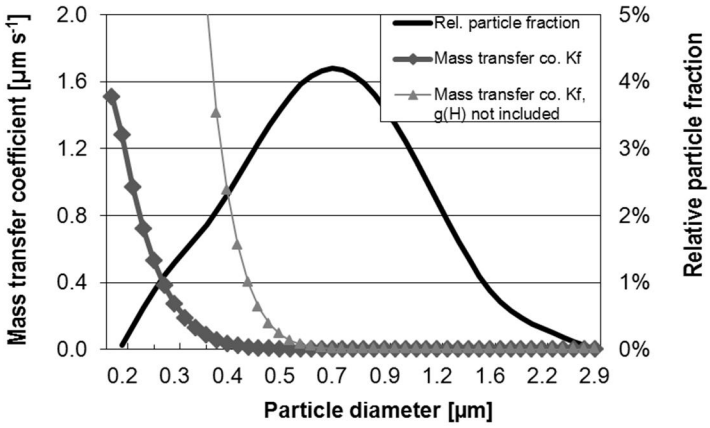

Figure 8. Mass transfer coefficient as a function of the particle size at temperature 345 K (bold grey line). The light grey line shows the mass transfer coefficient without the mobility correction of eq. (2.2.7) near the wall. The particle size distribution of the experiment is shown with black solid line. Smooth, clean stainless steel surface and spherical calcite particle were considered with a zeta potential of –25 mV (Ojaniemi *et al.,* 2012*)*.

According to the XDLVO theory, the fouling is strongly dependent on the particle size. In Figure 8, the mass transfer coefficient is shown as function of particle size at temperature of 345 K. For illustrating the importance of the hydrodynamic correction factor presented in equation (2.2.7), the mass transfer coefficient is also shown without the correction. For comparison, the particle size distribution of the slurry applied in the experiment is included in Figure 8. According to the model, only a small part of the size distribution is responsible of the fouling rate. The probability of the submicron particles to increase the fouling rate is in agreement with the discussion in Yiantsios and Karabelas (2003). Also Bacchin *et al.* (2006) showed that the surface interactions dominate over the other transport phenomena for the small particle sizes.

2.4 Re-entrainment of the adhered particles

Once the particle is adhered on the wall surface, the re-entrainment of the particle might take place. The models for re-entrainment are related to particle size, liquid dynamic viscosity and shear stress. The models presented in literature are based on force (or momentum) balance between the hydrodynamic forces and the corresponding surface forces (or momentums). In dynamic models, the re-entrainment of the particles is modelled with similar approach as with chemical kinetics: escaping of the molecules desorpted from a surface from the potential well. In here, the energy accumulation due to the natural resonant frequency of the particle-surface vibrations is included into the model. In quasi-static models, the instant force balance without energy accumulation is considered. For modelling the particle removal from the surface, the approaches based on dynamic re-entrainment, e.g., models of Vainshtein *et al.* (1997) and Reeks and Hall (2001) are proven to provide most accurate numerical predictions in comparison with the experimental data (Stempniewicz and Komen, 2010).

The so called Rock'n'Roll (RnR) quasi-static kinetic models are based on the idea of particle rocking continuously on about their contact point with the surface (Reeks and Hall, 2001; Zhang, F. *et al.*, 2013). The rocking is due to the fluctuation of the hydrodynamic force. If the contact with the surface is broken, rolling of the particle takes place, i.e. the re-entrainment of the particle. Therefore, the re-entrainment is dependent on the timescales of the particle rocking on the surface and fluctuating of the drag force.

In order to evaluate the re-entrainment form different substrate materials, the model has to be able to consider the material properties. Burdick *et al.* (2005) presented a model of critical particle Reynolds number for the hydrodynamic removal including the system-dependency via the Hamaker constant of van der Waals force. The model was applicable in laminar flow and the effect of turbulence was not considered. The model of Vainshtein *et al.* (1997) is capable of taking into account the surface energies of the materials and the hydrodynamic fluctuations.

The re-entrainment model of Vainshtein *et al.* (1997) has similarities with the approach of the RnR model: The particle is re-entrained once it has gained sufficient vibration energy to escape from the adhesive potential minimum. In the model of Vainshtein *et al.*, the depth of the adhesive potential minimum is described with the tangential pull-off force $\mathbf{F_{a\tau}}$

$$\mathbf{F_{a\tau}} = 9.3\frac{\Delta\gamma^{4/3} r_p^{2/3}}{k^{1/3}} \tag{2.4.0}$$

The tangential pull-off force is determined with the particle streamwise oscillations on the surface restrained by a spring. Thus, the adhesion force is balanced with the elastic tension.

The hydrodynamic drag force, $\mathbf{F_D}$, experienced by the adhered particle is parallel to the surface, and for a spherical particle in shear flow in contact with a plane surface the drag force can be calculated from (Goldman *et al.,* 1967)

$$\mathbf{F_D} = 6\pi\mu\dot{\gamma} r_p^2 f_c \tag{2.4.1}$$

where f_c = 1.7 is a correction factor to the Stokes drag due to the geometry of the problem.

The condition for the detachment is $\mathbf{F_{a\tau}} / \mathbf{F_D}$ < 1. The relation of the forces is (Vainshtein *et al.,* 1997)

$$\frac{\mathbf{F_{a\tau}}}{\mathbf{F_D}} = 0.3\frac{\Delta\gamma^{4/3}}{r_p^{4/3} k^{1/3} \mu\dot{\gamma}} \tag{2.4.2}$$

where r_p is particle radius, $\dot{\gamma}$ shear rate and $\Delta\gamma$ surface energy. k is elastic constant given by

$$k = \frac{4}{3}\left(\frac{1-\nu_p^2}{E_p} - \frac{1-\nu_s^2}{E_s}\right) \tag{2.4.3}$$

where $\nu_{p/s}$ and $E_{p/s}$ are the Poisson's ratio and Young's modulus of a particle and wall surface.

In calculation of the tangential pull-off force, $\mathbf{F_{a\tau}}$, in equation (2.4.2), the free surface energy $\Delta\gamma$ is the change in the surface energy that must be applied in order to separate a unit area of the surface (Bhushan, 2013):

$$\Delta\gamma = \gamma_1 + \gamma_2 - \gamma_{12}. \tag{2.4.4}$$

where γ_1 is the surface energy per unit area for the surface in fluid, and γ_2 is for the particle in fluid and γ_{12} in the contact between the materials. The data for the surface energies is not available for the most of the materials and their estimations has to be applied. The values for solids free surface energies ranges in generally from few hundreds to few thousands mJ/m^2. In comparison, for liquids the values are of the order of few tens of mJ/m^2, as shown in Tables 1 and 4 The higher the values are for solid surfaces, the stronger the bonds will be formed with the mating material (Bhushan, 2013).

The tangential pull-off force, $\mathbf{F_{a\tau}}$ from equation (2.4.0), and drag force, $\mathbf{F_D}$ from equation (2.4.1), are presented in Figure 9 on the smooth stainless steel plane surface as function of shear rate for three particle sizes. The detachment condition $\mathbf{F_{a\tau}} / \mathbf{F_D} < 1$ is obtained only with the particle size 40 µm with shear rates over 20 000 1/s.

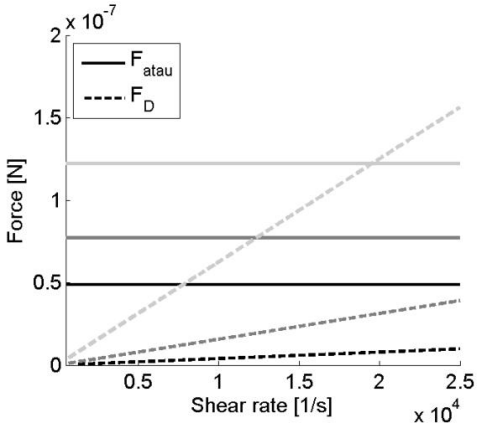

Figure 9. Tangential pull-off force, $\mathbf{F_{a\tau}}$ (solid line), and drag force, $\mathbf{F_D}$ (dashed line), on the smooth stainless steel plane surface as function of shear rate for three particle sizes: 10 µm (black lines), 20 µm (grey lines) and 40 µm (light grey lines).

According to the RnR model, the particle is re-entrained once it has gained sufficient vibration energy. The weakly bounded particles are assumed to have encountered a burst in a turbulent boundary layer before resuspending, similarly as in Reeks *et al.* (1988). The bursting frequency applied for a turbulent motion in a turbulent boundary layer applied is

$$f_o = \frac{u_\tau^2}{300\nu} \tag{2.4.5}$$

For calculation of the fraction of particles remaining on a flat surface at time t, the exponential decay assumed by Reeks *et al.* (1988) is used in the model of Vainstein *et al.* (1997)

$$f_r(t) = e^{-pt}, \tag{2.4.6}$$

where the re-entrainment rate constant p is calculated from (Vainshtein *et al.*, 1997)

$$p = f_o \exp\left[-\left(\frac{\mathbf{F_{a\tau}}}{\mathbf{F}_D}\right)^{4/3}\right] \tag{2.4.7}$$

The drag force, $\mathbf{F_D}$, in equation (2.4.7) is calculated from the mean value of the fluctuating component of the shear rate derived by Ziskind *et al.* (1995)

$$\langle \dot{\gamma} \rangle = 0.3 \frac{u_\tau^2}{\nu} \tag{2.4.8}$$

where u_τ is friction velocity at the wall.

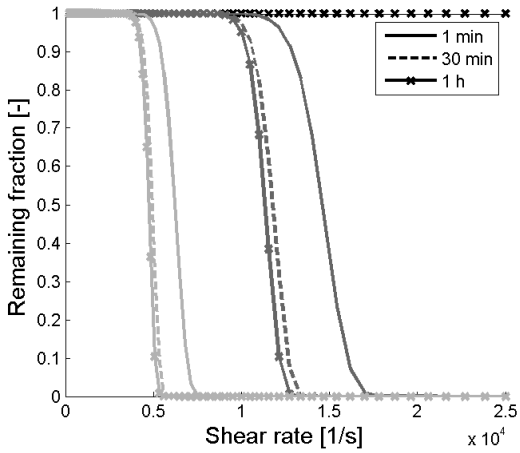

Figure 10. Remaining fraction on the smooth stainless steel plane surface for three particle sizes: 2 µm (black lines), 10 µm (grey lines) and 20 µm (light grey lines). The re-entrainment rates are shown as function of shear rate for three time instants: 1 min. 30 min and 1 h.

In Figure 10, the fraction of particles remaining on the smooth steel plane surfaces from the particles on the surface is shown for three particle sizes: 2 µm, 10 µm and 20 µm. The results are shown as function of shear rate at the instant times of 1 min, 30 min and 1 h. As shown in Figure 10, the particles sized 2 µm are not removed from the surface even with the shear rate 25 000 1/s and after one hour

exposure. The larger the particle is the easier is the re-entrainment. The parameters applied in the calculation are shown in Table 3. Therefore, based on the model of Vainshtein *et al.* (1997), the re-entrainment of submicron sized particle is not occurring from the smooth surface. The particle size has to be order of micrometres for the re-entrainment to occur.

Table 3. Model parameters for the re-entrainment.

	Calcite [1)]	Stainless steel [2)]
Poisson's ratio, -	0.322	0.28
Young's modulus, GPa	83.4[1]	215
Surface energy, J/m^2		0.15[2]

1) Chung-Cherng, 2013
2) Vainshtein *et al.,* 1997

2.5 Surface energy heterogeneity effect on fouling

The models presented in Section 2.3 describe the interactions between the spherical particle and wall surface with the uniform charge distribution. If the distribution is not uniform, the interaction between the particles is more complicated. The particle deposition on an unfavourable surface is enhanced, if the surface has favourable patches. Therefore, on the surface with small amounts of randomly distributed favourable patches, the locally attractive regions might be formed. This was suggested also by Bendersky and Davis (2011).

According to the predictions of the XDLVO model, a pure calcite particle is not adhering on a pure calcite surface, see Figure 11 (Ojaniemi *et al.,* 2012*)*. Since there is no minimum in energy barrier between the calcite particle and the calcite surface when approaching the surface, theoretically no adherence can take place.

In the analysis of deposited material of the industrial heat exchangers, in addition to the calcium, the scales are found to contain also other minerals, such as magnesium, silicates and iron (Riihimäki *et al.*, 2005). Magnesium is also a main impurity in natural calcites. The amount of these minerals in the scales is typically considerably greater than in the process fluid. Thus, the fouling of calcite particles can be thought to occur due to the impurities accumulated from the process fluid into the scales. The impurities have an effect on the surface chemistry of the fouled layer.

---

[1] Calculated from bulk modulus *K* and shear modulus *G* presented in Chung-Cherng (2013) with equation *9KG*/(*3K*+*G*).
[2] The value is for glass particles on a steal surface.

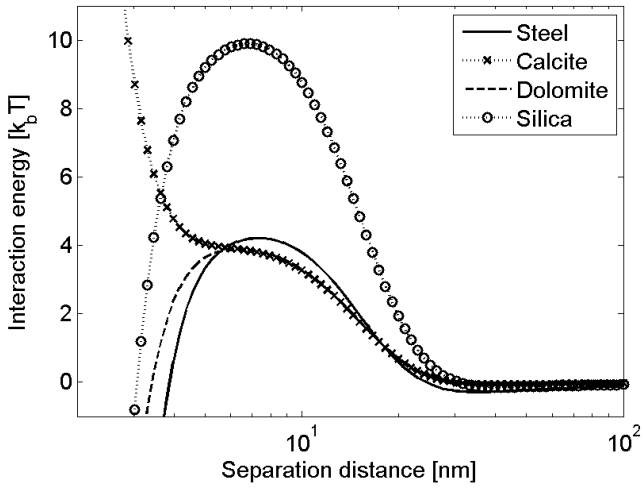

Figure 11. Interaction potential between $CaCO_3$ particle and surfaces of stainless steel, calcite, dolomite and silica at the surface temperature of 345 K. The potentials obtained by using the permittivity model of Teschke *et al.* (2001) are shown. Note the logarithmic scale of the distance between the particle and the surface (Ojaniemi *et al.,* 2012).

The interaction energies between the calcite particle and the flat surfaces of stainless steel, calcite, dolomite and silicate are compared in Figure 11. The energy barrier between the particle and the stainless steel surface is wider than the barrier between the dolomite surface and the particle. Therefore, the mass transfer coefficient for particle adhesion on the stainless steel surface was slightly greater than on the dolomite surface with the applied surface potentials. The fouling can also take place on the silicate surface, although it would be unlikely due to the large energy barrier. If the constant bulk value for the water permittivity would be used instead of the model of Teschke *et al.* (2001), a smaller fouling rate would be obtained in the presented cases.

The parameters for surface energy applied in the XDLVO calculations are shown in Table 1 and 4. The zeta potential of stainless steel was –25 mV, calcite –18 mV, dolomite –18 mV (Gence and Nurgul, 2006) and silicate –49 mV (Franks, 2002). For the particle zeta potential, the value –18 mV was applied.

The presence of additional salts, magnesium and silicates, in the fouled layer were included into the model as a deposition layer component (Ojaniemi *et al.,* 2012). In the fouling experiments, the deposition composition was not analysed. Therefore, the amounts of the impurities were taken from the industrial scale fouling analysis (Riihimäki *et al.*, 2005). The averaged mass of the magnesium Mg^{2+} compared to the mass of the calcium Ca^{2+} was found to be 8.2%. Thus, the fouling of calcite particles on the calcite surface consisting of 8.2 wt% magnesium was modelled. That is, the mass transfer coefficient K_f for dolomite surface was calcu-

lated from equation (2.5.0) with weight W = 0.082. For silicates, the relationship was 18.4 wt%. Thus, the mass transfer coefficient K_f for the silicate surface was calculated with W = 0.184.

$$K_{f,tot} = WK_{f,Mg} + (1-W)K_{f,CaCO_3}. \quad (2.5.0)$$

Table 4. Surface energy parameters for the XDLVO theory.

	Dolomite [1)] mJ/m^2	Silica [1)] mJ/m^2
Non-polar component, γ^{LW}	26.3	33.4
Electron donor, γ^-	15.9	15.3
Electron acceptor, γ^+	1.2	2.8

1) Wu *et al.*, 1996

2.6 Effect of surface roughness on fouling rate

2.6.1 Effect of surface roughness on particle adherence

The classical DLVO theory was developed for the smooth surfaces. Several studies have been carried out for investigating the effect of surface roughness on DLVO interaction energies. The studies are distinguished mainly in two methods: modified Derjaguin interaction (DI) approach (Suresh and Walz, 1996; Hoek and Agarwal, 2006; Huang *et al.*, 2010) and the surface element integration (SEI) (Martines *et al.*, 2008; Henry *et al.*, 2011). In the modified Derjaguin approximation technique, the smooth surface is assumed to consist of hemispherical asperities, and the interaction energy is assumed to be additive. SEI technique consists of calculating the interaction potential between the surfaces by integrating the energy per unit area over the exact surface topology.

Huang *et al.* (2010) showed that in comparison with SEI the modified Derjaguin integration (DI) remains accurate approximation when the particle size is large in comparison with the asperities. Method of SEI is more elementary and less restricted in a sense of particle radius, but it is also more computationally demanding in order to be implemented into CFD code. Therefore, in order to study the effect of surface roughness on particle deposition, the modified Derjaguin approximation technique proposed by Huang *et al.* (2010) was adopted. In the method, the surface is assumed to consist of hemispherical protrusions (convexes) and depressions (concaves), which separation distance were determined.

The equations (2.3.0), (2.3.2) and (2.3.4) present the method provided by Derjaguin (DI) for expressing the interaction energy between the sphere and plate.

The interaction between two spherical geometrics of different diameter, d_1 and d_2, is obtained from the equations by replacing d_p with

$$d = \frac{d_1 d_2}{(d_1 + d_2)} \tag{2.6.0}$$

In the method of Huang *et al.* (2010), the averaged magnitude of the interaction energy between the adhering particle and the rough surface is calculated as weighted sum of the interaction energies of between particle – hemispherical convexes (U_{SA}) and particle – flat surface (U_{SP}):

$$U_{SR}(D)=\eta U_{SA}(D)+(1-\eta-\omega)U_{SP}(D) \tag{2.6.1}$$

where D is the minimum separation distance between the surfaces, η is the fraction of interactions involving convex asperity and particle, and ω is the fraction of interactions involving concave asperity and particle. The weighting factors are presented by Huang *et al.* (2010).

In the case of surface with concave asperities, the interaction energy between the concave and particle larger than the concave is assumed to be zero, because the DI method is applicable only to the convex or plane surfaces. If the particle is smaller than the concave, the region of the edges of the concave is assumed to be zero-interaction region, and at the bottom, the spherical – flat plate interaction approximation is applied.

The method was applied on the model surfaces presented in Figure 12. In here, the interaction energy was calculated separately for the asperity sizes of 0.5 r_p and 2 r_p, where r_p is the particle radius 194 nm. The distance between the asperities, d_a, was three to six times the asperity radius. The weighting factors η and ω calculated for the applied scenarios with the model of Huang *et al.* (2010) are presented in Table 5.

Table 5. Weighting factors applied in Figure 13, calculated according to Huang *et al.* (2010).

Scenario	Asperity radius r_a	Distance d_a	η	ω
Convex	0.5 r_p	6 r_a	0.70	
	0.5 r_p	3 r_a	1	
	2 r_p	3 r_a	0.45	
Alternate	2 r_p	3 r_a	0.22	0.04

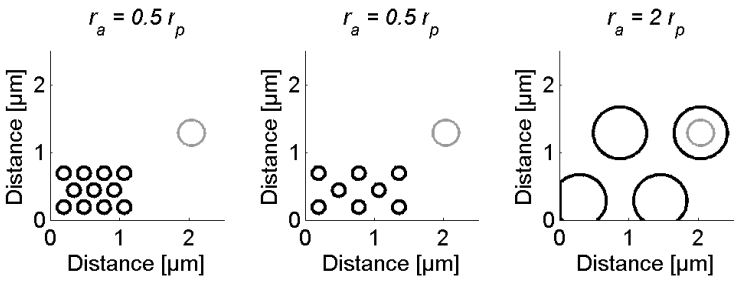

Figure 12. Models for rough surfaces. Surfaces are composed from hemispherical asperities. On the left: asperity radius r_a = 0.5 r_p, and distance between the asperities d_a = 3 r_a. At the middle: r_a = 0.5 r_p and d_a = 6 r_a. On the right: r_a = 2 r_p and d_a = 3 r_a. Particle sized r_p = 194 nm is shown with gray line.

In Figure 13, the effect of surface roughness on fouling rate is shown. The deposition mass transfer coefficient K_f was calculated separately for the model surfaces shown in Figure 12. In modelling, the asperities have assumed to be all convexes (C). In addition, for the surface with smallest asperities, the assumption of alternative convexes and concaves was applied (shown with dashed line, C+C, in Figure 13). The result for smooth, plane surface is shown for comparison.

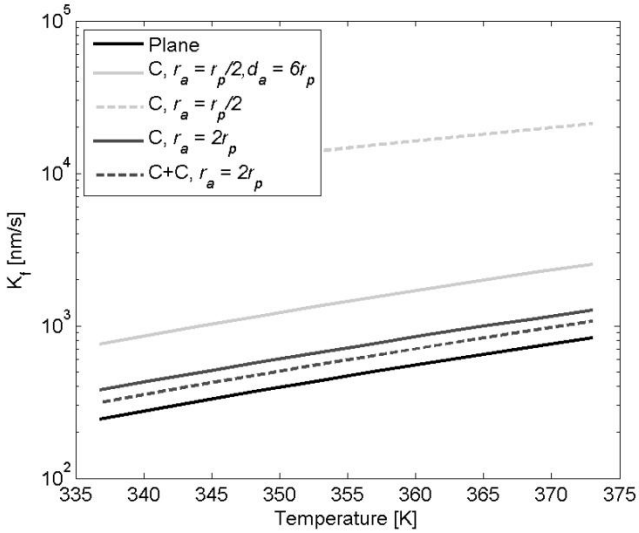

Figure 13. Fouling rate calculated for the model rough surfaces shown in Figure 12. C – convex asperities, C+C – convex and concave asperities. Particle size is r_p = 194 nm and distance between the asperities d_a = 3, if not mentioned. Note the logarithmic scale.

As seen in Figure 13, the model surface with the smallest convex asperities proved to be most easily fouled. The dense the distribution of the small asperities is the greater is the deposition rate. This is due to that in that case the particle is not reaching the smooth plane surface between the asperities (see Figure 12). The concaves decrease the fouling rate of particles larger than the concave in comparison to the surface comprising only convexes. The surfaces across the concaves are separated by the depth of the concave, and the interaction is not taking place as strongly. In the case of particle radius smaller than the concave, the bottom of the concave is assumed to be flat, and the deposition rate is decreased. The mechanical entrapment is not included in here.

In a case of the particle radius is smaller than the radius of the asperity, and the asperity size is increasing, the geometry between the asperity and particle surfaces approach to the geometry between plane and spherical particle. Therefore, also the fouling rate tends to the fouling rate on the smooth plane surface.

2.6.2 Removal from rough plane surface

In the quasi-static kinetic models, e.g., in the RnR model the particle is assumed to be rocking continuously on about its contact point with the surface (Reeks and Hall, 2001; Zhang, F. *et al.*, 2013). In modelling the re-entrainment from a smooth plane surface, the contact point of vibration was considered to be between the plane and the spherical particle. On a rough surface, the contact point is considered between the hemispherical protrusion and the particle. Therefore, the adhesive force on a rough surface is considered as a reduced force from an adhesive force on a smooth plane.

The reduction in the adhesive force is described with the adhesive radius $r_a' = r_a/r_p$, in where r_a is the asperity radius and r_p is the particle radius. The adhesive radius is considered to have a lognormal distribution $\phi(r'_a)$ with geometric mean $\overline{r_a}'$ and geometric standard deviation σ'_a

$$\phi(r_a') = \frac{1}{\sqrt{2\pi}} \frac{1}{r_a'} \frac{1}{\ln(\sigma_a')} \exp\left(-\frac{[\ln(r_a'/\overline{r_a}')]^2}{2(\ln(\sigma_a'))^2} \right). \tag{2.6.2}$$

The geometric mean $\overline{r_a}'$ is considered to be a measure of the reduction in adhesion force due to the surface roughness, and $\sigma'_a$is the spread of the adhesive forces (Vainshtein *et al.,* 1997). Biasi *et al.* (2001) has determined the parameters $\sigma_a' = 1.8 + 0.136r^{1.4}$ and $\overline{r}_a' = 0.016 - 0.0023r^{0.545}$ empirically based on the range of experiments presented in literature. Physically, $\phi(r'_a)$ describes the fraction of deposited particles that are attached on the surface with the adhesive force determined with r_a'.

The fraction $f_r(t)$ remaining on the rough surface at time t is obtained from equation (2.4.6) and (2.6.2) by integrating over the adhesive radius distribution (Reeks *et al.*, 1988, Vainshtein *et al.,* 1997)

$$f_r(t) = \int_0^\infty \exp([-p(r_a')t]\phi(r_a')d(r_a'), \tag{2.6.3}$$

In Figure 14, the lognormal distribution of adhesive radius r_a' from equation (2.6.2) calculated with particle sizes 0.387 µm and 2 µm are shown. In Figure 15, the fraction of particles remaining on the rough, stainless steel plane surfaces from the particles adhered on the surface is shown for two particle sizes: 0.387 µm and 2 µm. The results are shown as function of shear rate at the instant times of 1 ms, 1 s and 1 min. The parameters applied in calculation are shown in Table 3. In comparison with Figure 10 with plane surface, in where the particles sized 2 µm were not resuspending, the particles are re-entrained from the rough surface easily with significantly lower shear rates.

In Figure 16, the fraction of particles remaining on the rough stainless steel plane surfaces from the particles on the surface is shown for particle sizes of 0.387 µm. The results are shown as function of time with three shear rates 500, 1000 and 4000 1/s. For comparison, the result for the smooth plane is also shown. Even the submicron sized particles are re-entrained from the rough surface.

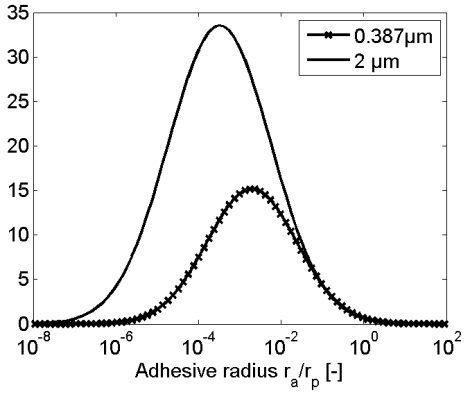

Figure 14. The lognormal distribution of adhesive radius calculated for particle sizes 0.387 µm and 2 µm with the parameters based on Biasi *et al.* (2001).

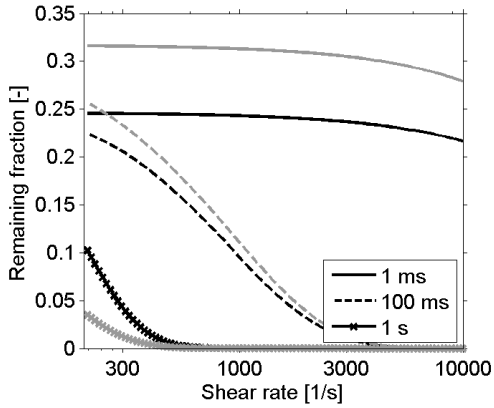

Figure 15. Remaining fraction on the rough stainless steel plane surface for two particle sizes: 0.387 µm (black lines) and 2 µm (grey lines). The remaining fractions are shown as function of shear rate for three time instants: 1 ms, 100 ms and 1 s.

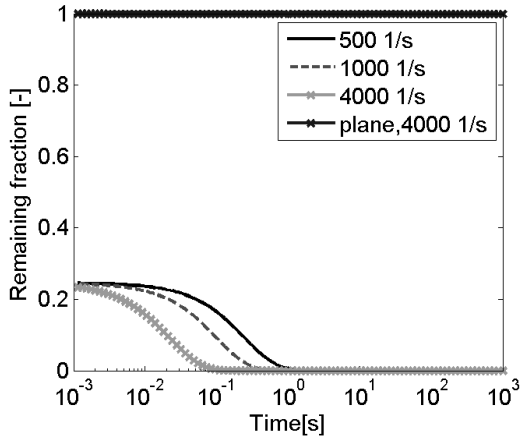

Figure 16. Remaining fraction on the rough, stainless steel plane surface with three shear rates for particle size 0.387 µm as a function of time. For comparison, the result for smooth plane surface is shown.

2.6.3 Combined effect of roughness on fouling rate

The surface roughness has shown to affect the particle adherence on the surface, and therefore the deposition of the particles is easier. On the other hand, the particles are more easily removed from the rough surface due to the smaller interaction energy. However, the comparisons with the experiments and theoretical calcula-

tions are difficult due to the randomness of the naturally rough surfaces. In here, the method of combined calculation of roughness effect on adhesion and re-entrainment of the particles is applied on the model surfaces presented in Figure 12.

The results for the effect of the model surface roughness on the deposition mass transfer coefficient K_f at the surface are shown in Figures from 17 to 19. The results of calculations with the model surface with asperity size of $0.5\ r_p$ are shown in Figures 17 and 18. In Figure 19, the results are shown for the model surface with asperity size of $2\ r_p$. All the asperities were assumed to be convexes. For comparison, the mass transfer coefficient for smooth plane is also shown. In calculations, the zeta potential of stainless steel was –25 mV, calcite –18 mV. The results are calculated for a time instant 0.1 s.

The effect of combined re-entrainment and adhesion effect on fouling rate due to the surface roughness depends on the adhesive radius magnitude. If the asperity size is small in comparison with the particle size, the deposition rate increases significantly in comparison with the smooth surface, see Figures 17 and 18. The shear rate should be quite high, around 5000 1/s for obtaining the fouling rate smaller than with the smooth surface. The deposition rate is even higher with the dense asperity distribution.

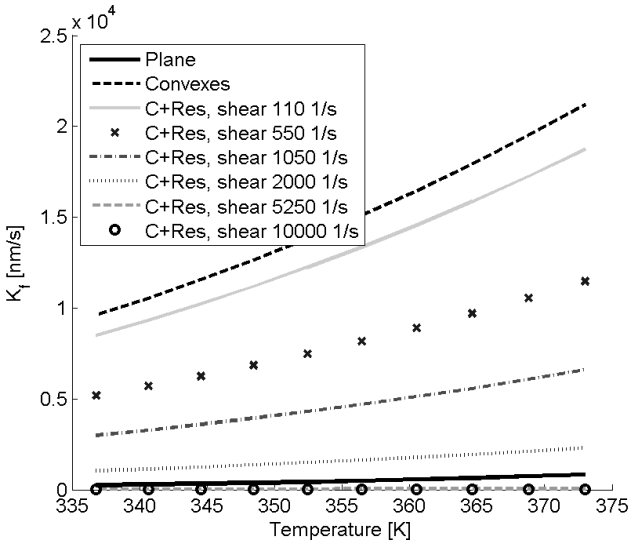

Figure 17. The deposition mass transfer coefficient K_f for $CaCO_3$ particle and rough stainless steel surface at the surface temperature of 345K. Particle size r_p = 194 nm, asperity size 0.5 r_p, distance between asperities 3 r_a, zeta potential of particle -18 mV and steel -25 mV. Results are calculated at time instant 0.1 s.

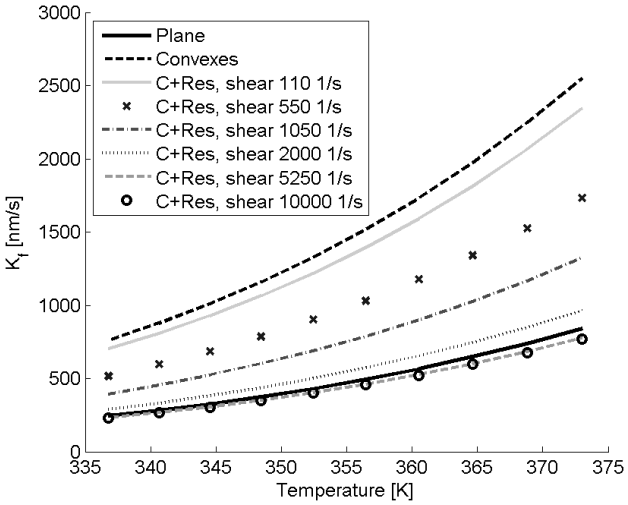

Figure 18. The deposition mass transfer coefficient K_f for $CaCO_3$ particle and rough stainless steel surface at the surface temperature of 345K. Particle size r_p = 194 nm, asperity size 0.5 r_p, distance between asperities 6 r_a, zeta potential of particle –18 mV and steel –25 mV. Results are calculated at time instant 0.1 s.

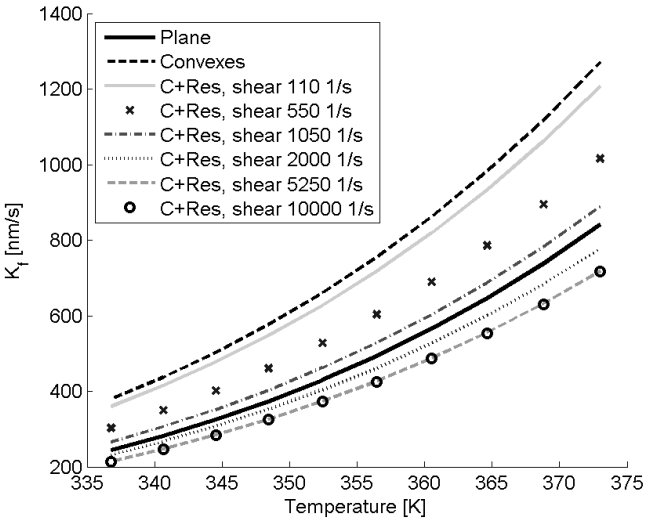

Figure 19. The deposition mass transfer coefficient K_f for $CaCO_3$ particle and rough stainless steel surface at the surface temperature of 345K. Particle size r_p = 194 nm, asperity size 2 r_p, distance between asperities 3 r_a, zeta potential of particle –18 mV and steel –25 mV. Results are calculated at time instant 0.1 s.

With the size of the asperity larger than particle size, e.g. in Figure 19, the deposition rate is not as strong as with the size of the asperity smaller than particle size. In addition, the fouling rate smaller than with the smooth plane is obtained already with the shear rates around 2000 1/s.

3. Wall function approach for particulate fouling

3.1 Wall function approach

The method of modelling particulate fouling in detail is applicable only for two-dimensional calculations due to the large computational effort caused by the fine mesh needed in the near-wall region. The size of the cell needed at the surface with detailed model is of order of micrometres. Coarse-grained fouling model, where the near-wall region is described with wall functions, was developed in order to simulate fouling by using larger near-wall grid cells with $y^+ = yu_\tau/\nu$ around or greater than one (Ojaniemi *et al.,* 2012).

The starting point for the wall function model is the assumption of the local equilibrium implying that the particles move always with their terminal velocity. This means that the particles are presumed to accelerate to the terminal velocity infinitely fast. The assumption is accurately valid for small colloidal particles in a liquid.

The equation for the slip velocity is

$$0 = \mathbf{F}_{\mathbf{tot}} + \left(\rho_p - \rho_q\right)\left[\mathbf{g} - \left(\mathbf{u}_\mathbf{m} \cdot \nabla\right)\mathbf{u}_\mathbf{m}\right] \tag{3.1.0}$$

where *m* refers to mixture and $\mathbf{F}_{\mathbf{tot}}$ is the total force affecting particle transport. The lift force was neglected as insignificant in comparison to the diffusion force (Adomeit and Renz, 1996; Ojaniemi *et al.*, 2008). Therefore, the total force affecting particles is composed of the drag and diffusion forces

$$\mathbf{F}_{\mathbf{tot}} = \mathbf{F}_{\mathbf{diff}} + \mathbf{F}_{\mathbf{drag}} \tag{3.1.1}$$

In equation (3.1.0), the term due to velocity gradients can be neglected close to the wall. Only the direction perpendicular to the wall (the y-component) is of interest. The acceleration term is also small because the mixture velocity in the y-direction and the x-derivative of the mixture velocity are small. Only the perpendicular component of gravitation $\mathbf{g}$ to the wall is important, although in colloidal sys-

tem gravitation is insignificant in overall. The equation for the y -component of the slip velocity is then (Ojaniemi *et al.,* 2012)

$$v_{slip} = -D_{diff}\frac{\partial \alpha_p}{\partial y} + v_{sg} \tag{3.1.2}$$

where the diffusion coefficient D_{diff} is modelled with equation (2.1.1) and v_{sg} is the slip velocity due to gravitation

$$v_{sg} = \frac{d_p^2\left(\rho_p - \rho_q\right)g_y}{18\mu_m}. \tag{3.1.3}$$

Here the slurry (mixture) viscosity μ_m is used instead of water viscosity in order to take into account the first order correction to the slip velocity.

Close to the wall, the form of the continuity equation proposed by Johnsen and Johansen (2010) is applied:

$$\frac{\partial}{\partial y}\left(\alpha_p \rho_p v_p\right) = -\frac{J_W}{y_b} \tag{3.1.4}$$

where ρ_p is the particle density and y_b is a distance beyond the particle boundary layer (Ojaniemi *et al.,* 2012). J_W is defined as positive when the particle flux is towards the wall.

Integration of equation (3.1.4) from 0 to y ($\alpha_p \rho_p v_p\big|_{y=0} = -J_W$) results in

$$-\alpha_p \rho_p v_p = J_W\left(1 - \frac{y}{y_b}\right) \tag{3.1.5}$$

Inserting the slip velocity (3.1.2) for v_p (positive away from the wall) the differential equation for the particle volume fraction can be written as

$$\alpha_p \rho_p\left(D_{diff}\frac{\partial \alpha_p}{\partial y} - v_{sg}\right) = J_W\left(1 - \frac{y}{y_b}\right) \tag{3.1.6}$$

Considering vertical flow, the gravitation vanishes in the direction perpendicular to the wall, i.e. $v_{sg} = 0$. As shown in Ojaniemi *et al.* (2012), integrating equation (3.1.6) with boundary conditions $\alpha_p(y_b) = \alpha_b$ and $\alpha_p(y_b) = J_W/(\rho_p K_f)$, and using the wall temperature for calculating D_B, the equation is formulated

$$-\ln\left(\frac{1-\alpha_b}{1-\alpha_0}\right)=\int_0^{y_b}\frac{J_W}{\rho_p\left(D_B+\nu_t/\sigma_t\right)}\left(1-\frac{y}{y_b}\right)\partial y \tag{3.1.7}$$

The turbulent kinematic viscosity profile near the wall is obtained from Johansen (1991)

$$\nu_t=\nu\left(\frac{y^+}{11.15}\right)^3, \quad y^+<3 \tag{3.1.8}$$

The equation (3.1.7) is integrated with the correlation for the turbulent kinematic viscosity, equation (3.1.8), and the following form is obtained (Ojaniemi *et al.,* 2012)

$$-\ln\left(\frac{1-\alpha_b}{1-\alpha_0}\right)=\frac{11.15^3\sigma_t J_W}{\rho_p u_\tau}I\left(y_b^+,a\right) \tag{3.1.9}$$

where $a = 11.15^3\sigma_t D_B/\nu$, $\alpha_p(0) = \alpha_0 = J_W/(\rho_p K_f)$, and

$$I\left(y_b^+,a\right)=\int_0^{y_b^+}\frac{dy^+}{(a+y^{+3})}\left(1-\frac{y^+}{y_b^+}\right) \tag{3.1.10}$$

The integral (3.1.10) can be evaluating analytically. The final algebraic equation for solving the particle flux to the wall from the bulk volume fraction α_b far away from the wall become

$$J_W=\rho_p K_f\left[1-e^{J_W/B}\left(1-\alpha_b\right)\right] \tag{3.1.11}$$

where

$$B=\frac{b}{I\left(y_b^+,a\right)}=\frac{\rho_p u_\tau}{1386\cdot\sigma_t I\left(y_b^+,a\right)} \tag{3.1.12}$$

The gravitation has to be taken into account e.g. in the case of profiled heat exchanger plate surfaces. When the gravitation term is retained in the model of slip velocity, the obtained model is not analytically solvable. A fairly accurate analytical solution is obtained by making the approximations $a^{1/3} << y_b^+$ and $\alpha_q \sim 1$ (Ojaniemi *et al.,* 2012). Denoting $c = \rho_p v_{sg}/b$ and

$$I_1\left(y_b^+, a\right) = \int_0^{y_b^+} \frac{dy^+}{(a + y^{+3})} \tag{3.1.13}$$

the approximate equation for solving the particle flux to the wall is written in a form

$$\alpha_b = -\frac{J_W}{\rho_p v_{sg}} + J_W \left(\frac{1}{\rho_p K_f} + \frac{1}{\rho_p v_{sg}} \right) e^{cI_1(y_b^+, a)} \tag{3.1.14}$$

The particle concentration profile in the near wall region was solved with ordinary differential equations (ODEs) in MATLAB (MATLAB, 2012) from equation (3.1.6). In calculations, the shear stress at the wall has been obtained from the CFD calculation with a dense grid (see Figure 27). The simulations with CFD are described in Sections 5 and 6. The calculated results are compared with the CFD simulation results in Figure 20. The calculated profiles with the wall function approach are in fairly qood agreement, within 5% difference with the simulated profile. The difference between the models is due to the different model applied for the turbulent viscosity, see Figure 31.

The simplified wall function model includes drag and diffusion, but thermophoresis, lift forces, and particle interaction are neglected.

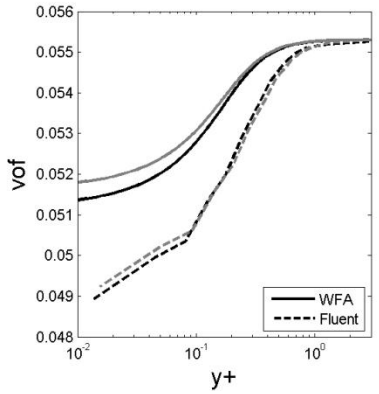

Figure 20. Particle volume fraction profile in the near wall region solved from equation (3.1.6) and simulated with CFD. Black – Yang and Shih model. Light gray – standard k-ε model with enhanced wall treatment. See text for the description of the profiles.

3.2 Wall function approach with thermophoresis

The thermophoresis is present mostly in the near wall region of the heated surface, where the temperature gradient is larger compared to the gradient further away from the surface. Therefore, in the slip velocity calculation of the wall function approach, equation (3.1.0), $\mathbf{F}_{\mathbf{tot}}$, has to include also thermophoresis (Ojaniemi *et al.,* 2013)

$$\mathbf{F}_{\mathbf{tot}} = \mathbf{F}_{\mathbf{diff}} + \mathbf{F}_{\mathbf{drag}} + \mathbf{F}_{\mathbf{th}} \tag{3.2.0}$$

The thermophoretic velocity is calculated by thermal diffusivity $D_{th} = S_{th} D_B$, where the Soret coefficient S_{th} is a model and temperature dependent coefficient and D_B is Brownian diffusion.

The equation for the y-component of the slip velocity from equation (3.1.0) is now

$$v_{slip} = -\left(\frac{D_B + D_t}{\sigma \alpha_p \alpha_q}\right)\frac{\partial \alpha_p}{\partial y} - S_{th}\frac{\partial T}{\partial y} + \frac{\left(\rho_p - \rho_q\right) g_y}{K_{pq}} \tag{3.2.1}$$

where the Stokes expression is applied for the interphase momentum exchange coefficient, K_{pq}.

In order to complete the model, temperature wall function is also needed. With the assumption that the temperatures of fluid and particles are equal, the enthalpy equation is

$$\nabla \cdot \left(\alpha_p \rho_p \mathbf{u_p} H_p + (1-\alpha_p)\rho_q \mathbf{u_q} H_q\right) = \nabla \cdot \left(\lambda_{eff} \nabla T\right) \tag{3.2.2}$$

where λ_{eff} is the effective heat transfer coefficient and H_i is the sensible enthalpy of phase i. Next it is approximated that the liquid velocity perpendicular to the wall is small and can be neglected. The specific enthalpy h_i of phase i is assumed to be constant so that for particle phase

$$h_p = h_{p,ref} + c_{p,p}\left(T - T_{ref}\right) \tag{3.2.3}$$

Integrating Eq. (3.2.2) and denoting the wall heat flux by q_W (positive towards the wall), it follows

$$q_W = \lambda_{eff}\frac{\partial T}{\partial y} - \alpha_p \rho_p v_{slip}\left[c_{p,p}\left(T - T_W\right)\right] \tag{3.2.4}$$

The effective heat transfer coefficient is written as

$$\lambda_{eff} = \frac{c_{p,m}\mu_t}{\mathrm{Pr}_t} + \alpha_p\lambda_p + \alpha_q\lambda_q \tag{3.2.5}$$

where the default value for Pr_t is 0.9. Combining equation (3.2.3) with equation (3.1.5) and with $v_p = v_{slip}$ gives

$$q_W = \lambda_{eff}\frac{\partial T}{\partial y} + J_W\left(1-\frac{y}{y_b}\right)c_{p,p}\left(T-T_W\right) \tag{3.2.6}$$

Solving for $\partial T/\partial y$ and inserting in equation (3.1.5) with $v_p = v_{slip}$ from equation (3.2.1) results in

$$\rho_p\left(\frac{D_B+D_t}{\sigma\alpha_q}\right)\frac{\partial\alpha_p}{\partial y} + \alpha_p\rho_p S_{th}\frac{q_W}{\lambda_{eff}} - \alpha_p\rho_p\tau_p g_y = J_W\left(1-\frac{y}{y_b}\right), \tag{3.2.7}$$

where $\tau_p = d_p^2(\rho_p-\rho_q)/(18\mu)$ is the particle relaxation time. The convective term in the heat transfer equation is considered to be negligible. The solution for the equation (3.2.7) is obtained by assuming the temperature dependent physical fluid properties to be constant at the wall temperature (Ojaniemi *et al.,* 2013*)*. This assumption is valid, because the wall function model operates in the near-wall region y^+ < 3, where the change in the temperature is of the order of few degrees, see Figure 21.

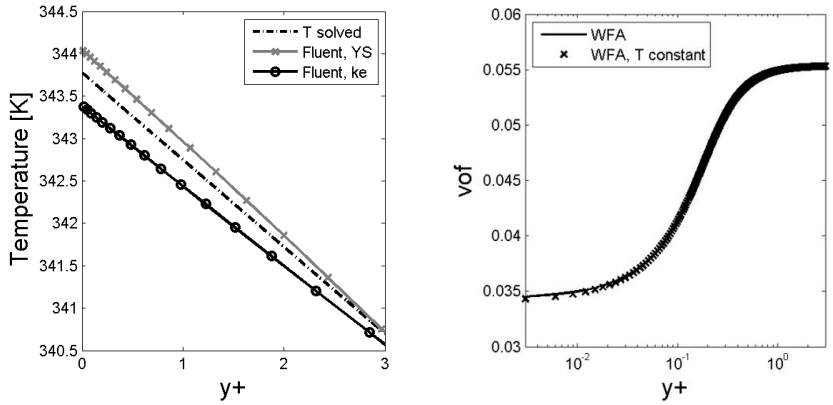

Figure 21. On the left: Temperature profiles in the near wall region solved from equation (3.2.7) and simulated with CFD. On the right: Particle volume fraction profiles in the near wall region. See text for the description of the profiles.

The temperature profiles in Figure 21 are calculated from equation (3.2.7) with solving the temperature dependent properties of the fluid and with assuming the properties to be constant in a wall temperature. The equation is solved with Ordinary Differential Equations (ODEs) in MATLAB (MATLAB, 2012). In calculations, the shear stress at the wall has been obtained from the CFD simulation. The CFD simulations are described in Sections 5 and 6. The calculated results for the temperature profiles are compared with the CFD simulation results. The both calculated profiles agree well with the simulated profile. The difference between the profiles calculated with the assumption of constant temperature dependent properties or solving the properties with temperature profile is insignificant. As seen in Figure 21, the effect on the particle volume fraction profile in the near wall region is negligible. Therefore, the assumption of applying the constant temperature dependent properties calculated at the wall temperature is valid. The model of Würger (2009) for the Soret coefficient, equation (2.1.6), has been applied in calculation of the results shown in the Figure 21.

The final algebraic equation for solving the particle flux to the wall from the bulk volume fraction α_b far away from the wall is

$$J_W = \rho_p K_f \left[\frac{Z - J_W e^{J_W/B}\left(1-\alpha_b\right)}{Z + (c-s)e^{J_W/B}\left(1-\alpha_b\right)} \right], \tag{3.2.8}$$

where $Z = J_W + (c - s)\ \alpha_b$, $c = \rho_p\ v_{sg}$, $s = \rho_p\ S_{th}\ q_W / \lambda_{eff}$ and B is a parameter depending on the diffusion coefficients (Ojaniemi *et al.*, 2013).

4. Implementation of CFD models

4.1 Implementation of detailed fouling model

In the CFD model developed for particulate fouling, the models described in Section 2.1 for the forces influencing the particle movement have been adapted. The detailed particulate fouling model describes the forces affecting the particle transport precisely. The deposition rate at the heated wall was calculated from the particle flux which was applied as a boundary condition.

The boundary condition for the particle flux at the heated wall was calculated from equation (2.2.9). The concentration of the particles C_0 at the wall was evaluated by using the value at the centre of the cell adjacent to the wall and the concentration gradient calculated by Fluent. Hence, the concentration at the wall is

$$C_0 = C(y = y_c, x) - \left.\frac{\partial C}{\partial y}\right|_{y_c} ds \tag{4.1.0}$$

where ds is the distance between the wall and the cell centre, y_c is the y-coordinate of the cell centre, and the concentration gradient $\partial C/\partial y$ is calculated at the point y_c. With the aid of equations (4.1.0) and (2.2.10), the particle flux to the wall can be obtained from equation (2.2.9).

The models for the forces affecting the particle transport and the adhesion of particles on the wall surface were implemented into the Euler-Euler multiphase model of Fluent using User-Defined Functions, UDF (Fluent, 2009). The particle flux calculated by using the wall boundary condition (2.2.9) was implemented as a sink term in the mass conservation equation. The sink term $\mathbf{S_p}$ was added into the mass conservation equation of particle phase:

$$\frac{\partial \rho_p}{\partial t} + \nabla \cdot \left(\rho_p \mathbf{u_p} \right) = \mathbf{S_p} \tag{4.1.1}$$

The forces affecting on the particle transport were included into the momentum conservation equation as source terms. The momentum conservation equation for phase *p* with the granular flow is (Fluent, 2009)

$$\begin{aligned}&\frac{\partial}{\partial t}\left(\alpha_p \rho_p \mathbf{u_p}\right)+\nabla\cdot\left(\alpha_p \rho_p \mathbf{u_p}\mathbf{u_p}\right)=\\&-\alpha_p \nabla p-\nabla p_s+\nabla\cdot\left(\overline{\overline{\tau}}_p\right)+\alpha_p \rho_p \mathbf{g}+\sum_{p=1}^{n}\mathbf{F_{drag,pq}}+\mathbf{F_{tot}}\end{aligned}, \tag{4.1.2}$$

where $\mathbf{F_{tot}} = \mathbf{F_{diff}}$ is total source due to the diffusion forces. For the fluid phase q, the same source terms with opposite sign were added. At the wall region, the momentum sink due to the removed mass, $-\mathbf{S}_p\mathbf{u}_p$, was added into the momentum conservation equation of particulate phase.

The calculation of the reaction rate K_f from equation (2.2.10) would be of large computational effort if incorporated in the CFD simulation as such. Therefore, the reaction rate K_f was calculated separately with several wall surface temperatures in MATLAB. The results were fitted with exponential function, which was then applied in the CFD simulations. The reaction rate fitted to the results calculated with the parameters described in Section 2.3.1 is

$$K_f(T)=\exp\left(-6\cdot10^{-5}T^2+0.069T-7.4\right) \tag{4.1.3}$$

The calculated K_f values and the curve from equation (4.1.3) are shown in Figure 22 as a function of temperature.

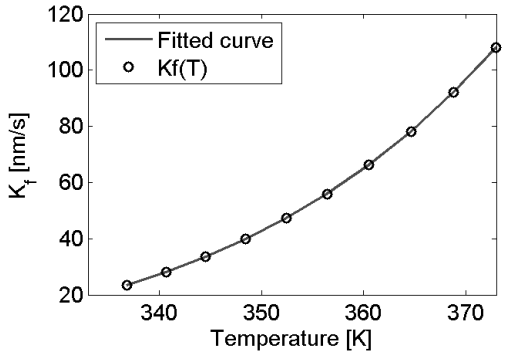

Figure 22. Rate constant K_f as a function of the wall surface temperature.

4.2 Implementation of Wall function approach

The wall function is based on the formulation of the forces applied in the detailed model. From the particle flux at the wall, the source term for particle deposition was calculated. The approach was first implemented in Euler-Euler multiphase model.

The particulate deposition rate on the wall surface was calculated from the particle flux modelled by equations (3.1.11), (3.1.14) or 3.2.8. The particle flux to the wall was solved numerically from the volume fraction of the particles, α_b, in the computational cell centre adjacent to the wall. The flux was implemented with UDF as a boundary condition at the heated surface. In the Eulerian-Eulerian approach, the sink term $\mathbf{S_p}$ was added into the mass conservation equation of particle phase, see eq. (4.1.1). The momentum sink due to the removed mass, $-\mathbf{S}_p\mathbf{u}_p$, was added into the momentum conservation equation of particulate phase, see equation (4.1.2).

The wall function approach was implemented also with the algebraic slip mixture model (ASM). In the ASM approach, the sink term $\mathbf{S_p}$ was added into the mass conservation equation of particle phase. The momentum sink due to the removed mass, $\mathbf{F_{tot}} = -\mathbf{S}_m\mathbf{u}_m$, was added into the momentum conservation equation of mixture phase

$$\begin{aligned}\frac{\partial}{\partial t}\left(\rho_m \mathbf{u_m}\right) + \nabla\cdot\left(\rho_m \mathbf{u_m}\mathbf{u_m}\right) &= -\nabla p - \nabla p_s \\ + \nabla\cdot\left(\mu_m\left(\nabla\mathbf{u_m} + \nabla\mathbf{u_m^T}\right)\right) + \rho_m\mathbf{g} + \nabla\cdot\left(\sum_{p=1}^{n}\left(\alpha_p\rho_p\mathbf{u_{dr,p}}\mathbf{u_{dr,p}}\right)\right) &+ \mathbf{F_{tot}}\end{aligned} \tag{4.2.0}$$

where m refers to mixture, and $\mathbf{u_{dr,p}} = \mathbf{u_p} - \mathbf{u_m}$ is the drift velocity for particle phase (Fluent, 2009).

4.3 Implementation of model for re-entrainment

The model for particulate re-entrainment proposed by Vainshtein *et al.* (1997) presented in equation (2.6.3) for rough surface was implemented into CFD code with applying probability analysis. The fractional re-entrainment rate is calculated from (Reeks *et al.,* 1988) *et al.*

$$\Lambda(t) = -\dot{f}_r(t) = \int_0^\infty p(r_a')\exp([-p(r_a')t]\phi(r_a')d(r_a') \tag{4.3.0}$$

For calculating the averaged time for particulate re-entrainment, the probability theory was applied. Based on fractional rate equation (4.3.0), the expected value for the re-entrainment time (t_{exp}) is calculated from[3]

$$\begin{aligned} E(t) &= -\int_0^\infty \dot{f}_r(t) t dt \\ &= \int_0^\infty \int_0^\infty t p(r_a') \exp([-p(r_a')t] \phi(r_a') d(r_a') dt \\ &= \int_0^\infty \frac{1}{p(r_a')} \phi(r_a') d(r_a') \end{aligned} \tag{4.3.1}$$

For calculating the re-entrainment rate with CFD, the source term $\mathbf{S_p}$ for the removed mass is calculated with the expected re-entrainment time and with the fraction of particles remaining at the surface at that time

$$\mathbf{S_p} = n_p \left(1 - \frac{f_{susp}(t_{\exp}) \Delta t}{t_{\exp}} \right) \frac{m_p}{V_{cell} \Delta t} \tag{4.3.2}$$

where $t_{\exp} = E(t)$, n_p number of adhered particles, Δt time step [s], V_{cell} cell volume [m^3] and $f_{susp}(t_{\exp}) = 1 - f_r(t_{\exp})$. $f_r(t_{\exp})$ was calculated according to equation (2.6.3).

The integration of equation (4.3.1) was calculated in MATLAB as a function of shear rate. The term in equation (4.3.2) comprising the expected time and fraction remaining at the expected time was calculated, and fitted with polynomic function for obtaining a simple equation for implementation of the source term for depositing mass including re-entrainment, see Figure 23.

---

[3] Equation (4.3.1) presenting the expected time for the fractional re-entrainment is normalized as

$$-\int_0^\infty \dot{f}_r(t) dt = -\left(f_r(\infty) - f_r(0) \right) = -\left(0 - 1 \right) = 1$$

where $f_r(t)$ is the fraction of particles remaining on the surface at time t.

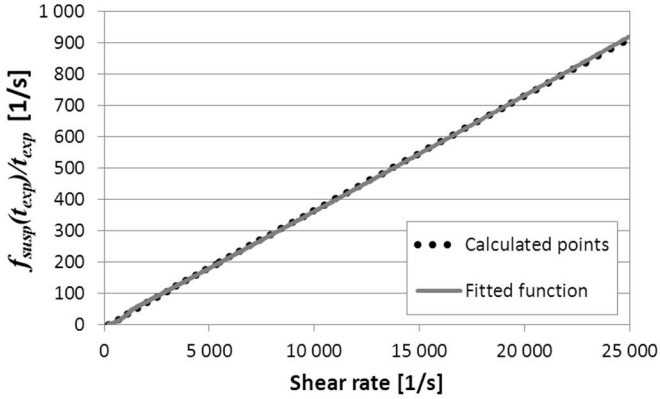

Figure 23. The term in equation (4.3.2) comprising the expected time and fraction remaining at the expected time as a function of shear rate.

5. Test case for modelling fouling

5.1 The laboratory fouling apparatus

The test equipment of fouling experiments in Oulu University was used as a test case in simulations with CFD (Riihimäki *et al.*, 2010). The test apparatus consisted of agitated vessel of 150 dm^3, from where the slurry was pumped to the test section through the double pipe heat exchanger, which controls the temperature of the test fluid. The test section consisted of a rectangular flow channel, which had a flow area of 15 x 100 mm and a length of 0.95 m. In the test section, two removable smooth stainless steel (AISI 316L) test plates of area 100 x 200 mm were mounted. The test plates were placed on a 25 mm thick copper block with embedded ohmic heaters. The testing facilities are described in more details in Riihimäki *et al.* (2010), and Ojaniemi *et al.* (2012).

Test runs were carried out by MSc. Markus Riihimäki with several mass flow rates of slurry, particle concentrations and heat fluxes. Table 6 shows the parameters of the test cases applied in the comparison. Test periods were restricted from 200 to 600 min. The mass of the deposited particles was measured after each experiment and mass deposition rate was calculated from the mass and time of the experimental test period.

In the experiments, the dispersed slurry of grounded lime stone with solid content of 50 wt% was applied as test fluid. The slurry was diluted with de-ionized water to the lower concentrations, and the conductivity of the slurry was maintained with added $MgCl_2$. More details of the test fluid are found from Ojaniemi *et al.* (2012).

5.2 Computational grid

In the simulations of the fouling test apparatus, three computational grids were applied: for detailed model extremely 2D grid was required, for wall function approach, a coarser 2D grid was of applied, and for modelling with Large Eddy Simulation (LES), the 3D dense grid was needed. The outlines of the 2D and 3D computational grids for are shown in Figure 24. The vertical flow is directed downwards.

The detailed model required extremely dense grid in the near wall. The two-dimensional grid is symmetrical with respect to the centreline consisting of 2240 cells. The width of the grid is 11.5 mm and height 254 mm. The size of the smallest cells in the vicinity of the wall is 1 µm. The value of y^+ in the near wall cells was 0.01. The simulations were carried out as time dependent calculation with a time step of 1 ms.

For the wall function approach, a coarse 2D grid could be applied thus reducing the computational effort needed. The applied two-dimensional asymmetric computational grid consisted of 1120 cells. With the wall cell size of 0.15 mm, the y^+ value of about 1 was obtained.

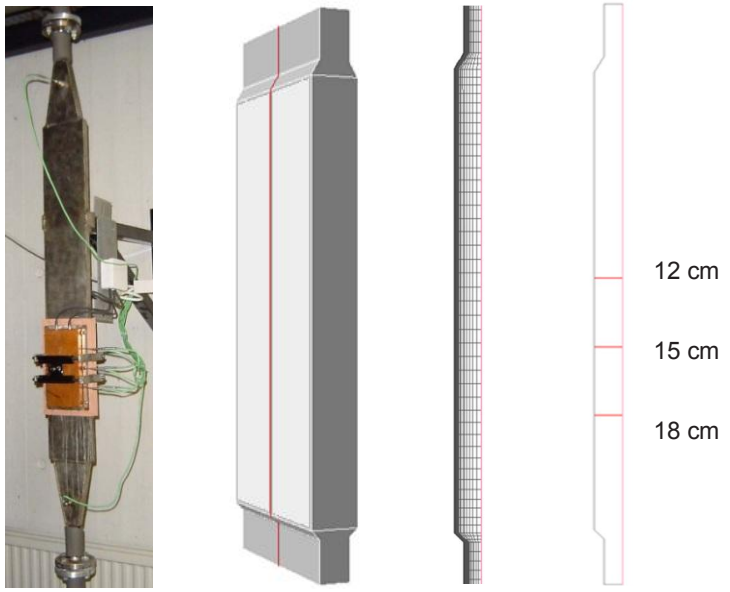

Figure 24. Test apparatus and computational 3D and 2D grids applied. Flow is directed downwards (Ojaniemi *et al.,* 2013*)*. On the right, the planes at three distances from the inlet at the top of the grid are shown.

For modelling the flow field structure with Large Eddy Simulation (LES) approach, the three-dimensional computational grid used consisted of 1.2 million cells. The non-dimensional grid spacings at the wall were Δx^+*~40,* Δz^+*~10* and Δy^+*~0.7,* in accordance with the typical resolution requirements for LES (Menter, 2011). With time step 7.5 ms, the Courant number was around 0.4 in the near wall region (Ojaniemi *et al.*, 2013).

5.3 Boundary conditions of the test case

In the simulation, the material properties and the boundary conditions used in experiments were applied. The parameter values are shown in Table 6. In the verification of the detailed model and the wall function approach, a smooth, clean stainless steel surface was assumed. The value applied for zeta potential of calcite particle was –18 mV and for steel surface, –25 mV.

In the experiments, the time period was several hours, implying that the fouling was actually occurring on the fouled surface after the first layer of deposited material covered the steel surface. Therefore, the simulations for comparison the result with the experimental results were carried out with the assumption of fouled layer. The presence of additional salt of magnesium was included into the model as a deposition layer component according to Section 2.5. The value applied for zeta potential of dolomite was –18 mV and for calcite particle, –18 mV, according to the measurement after the salt addition in the experiments (Riihimäki *et al.*, 2010).

Table 6. Material properties and boundary conditions of the case modelled.

Density of particles ($CaCO_3$) , kg/m^3	2711
Zeta potential of particles, mV	-18
Thermal conductivity of particles, W/(m·K)	2.7
Specific heat of particles, J/(kg·K)	856
Averaged particle diameter, nm	820
Representative particle diameter, nm	387
Mg^{2+} content of fouled layer, -	0.08
Ion strength, mol/dm^3	0.0044
Slurry viscosity, kg/(m·s)	2 × water viscosity
Flow rate, dm^3/s	0.3, 0.5, 0.8
Particle concentration at inlet, vol%	4.9, 5.5
Temperature of water at inlet, K	333
Heat flux from heat wall, kW/m^2	18.5, 21, 24

The fouling is strongly dependent on the particle size, as shown in Figures 6 to 8. With the average particle size of 820 nm determined from the test fluid, the fouling rate would be very small and would not represent correctly the fouling due to the whole distribution of the particle sizes. In order to keep the computing time reasonable, the CFD modelling was restricted to one particle size. Therefore, it is essential to determine the characteristic particle size of the system. The experiment was simulated with three particle sizes: with the smallest size of the distribution 210 nm, the median size of the distribution 680 nm and the size in between

these two sizes, 360 nm. The characteristic particle size was determined by finding the size, with which the resulting fouling rate would correspond to the resulting fouling rate of the three particle sizes. By using this procedure, the characteristic particle size determining the fouling was found to be 387 nm (Ojaniemi *et al.,* 2012).

In the simulations, the inlet profiles for velocity magnitude, particle distribution and turbulent kinetic energy and dissipation, and velocity were calculated separately with CFD in order to minimize the effect of inlet into the flow field. The model of standard k-ε with enhanced wall treatment (EWT) for turbulence modelling was applied in calculating the profile. The enhanced wall treatment approach is a method in Fluent for modelling the near wall region (Fluent, 2011). In the method, the turbulence models are modified to enable the viscosity-affected region to be solved with a mesh to the wall, including also the viscous sub layer. The method is adequate e.g. with the flows of low Reynolds number, $\mathrm{Re}=\rho\mathbf{u}\mathrm{L}/\mu$. The characteristic length L of the channel flow is the half width of the channel.

5.4 Turbulence models applied in CFD simulation

The shear stress is the major effect in particle re-entrainment implying that the realistic modelling of turbulence is essential. Here, the CFD simulations of a test heat exchanger were performed with Large Eddy Simulation (LES) in 3D and compared to the results calculated with standard k-ε model with EWT in 2D and 3D (Ojaniemi *et al.*, 2013). The Reynolds number of the test case was 6200. In the industrial test heat exchanger, the Reynolds number is lower. Therefore, the applicability of the low Reynolds number turbulence model of Yang and Shih (1993) was tested (Fluent, 2009).

Since the large scale turbulent eddies contain most of the energy and account for most of the turbulent transport, they dominate the main properties of the turbulent flow. In LES, the large eddies are resolved numerically, and only the small scale eddies having a slight effect on the large scale eddies are modelled with sub grid scale model (SGM). The wall-bounded flows, as in the case of heat transfer, are demanding situations for LES modelling. The high resolution of the grid is needed near the wall. The needed computational power used (CPU) increases also due to the need of small Courant number, $CFL=\mathbf{u}\,\Delta t/\Delta x < 1$, where $\mathbf{u}$ is bulk fluid velocity.

The classical and widely applied Smagorinsky sub grid model is not applicable in wall bounded flows due to the excessive dampening of the large scale eddies near the wall without correcting the model parameters. The Wall-Adapting Local Eddy-Viscosity (WALE) model returns the correct near wall behavior of turbulent viscosity for wall bounded flows (Nicoud and Ducros, 1999; Fluent, 2011). In addition, WALE returns a zero turbulent viscosity for laminar shear flows, in contrast to the Smagorinsky model. From the models provided by Fluent, the WALE model is then preferable model for the sub grid model of LES in the studied case.

Therefore, the simulations were carried out with LES model applying the WALE model for sub grid turbulent viscosity. For the momentum conservation, the bounded central discretization method was applied, for volume fraction the second order discretization and for time discretization, the implicit second order method was used. For producing the turbulent flow in the LES simulations, the boundary condition of introducing vortex instabilities into the flow was applied at inlet.

For comparison of the results with LES, the standard k-ε model with EWT was used for modelling turbulence in the same case with same grid and time step. The same inlet profiles calculated with separate CFD for velocity, particle distribution, turbulent kinetic energy and dissipation were applied in both 3D simulations.

5.5 Hydrodynamic models applied in CFD simulation

CFD simulations of the particle deposition on the heated wall were carried out with the multiphase models of Eulerian two-phase model and algebraic slip mixture model (ASM) of Fluent (Fluent, 2009). The pressure based coupled solver was applied. At the outlet boundary, the static gauge pressure was set to zero.

For the interphase momentum exchange coefficient between the phases, the model of Wen and Yu (1966) was applied. The particle-particle interaction was included by applying the granular model of Fluent. The model takes into account the maximum packing density of the particles in the fluid. With Eulerian two-phase model, the kinetic viscosity of particles was calculated with the model of Gidaspow *et al.* (1992). For the bulk viscosity, the model of Lun *et al.* (1984) was applied. With the model of ASM, the mixture viscosity was applied for the both phases. For granular temperature in the model of solids pressure, the algebraic model was applied (Fluent, 2009). The model derived by Lun *et al.* (1984) was applied for the collisional dissipation energy. For radial distribution function, the model proposed by Ogawa *et al.* (1980) was applied (Fluent, 2009).

The temperature dependency of water viscosity was calculated from (Perry, 1970)

$$\frac{1}{10\mu} = 2.1482\left[\left(T-281.435\right)+\sqrt{\left(8078.4+\left(T-281.435\right)^2\right)}\right]-120 \qquad (5.5.0)$$

where T is the water temperature.

The water density dependency on temperature was calculated from (Kell, 1975)

$$\rho(T) = \frac{\left(\left(\left(\left(aT+b\right)T+c\right)T+d\right)T+e\right)T+f\right)}{\left(1+gT\right)} \qquad (5.5.1)$$

where a = $-2.8054\cdot10^{-10}$, b = $1.0556\cdot10^{-7}$, c = $-4.6170\cdot10^{-5}$, d = -0.0079870, e = 16.945, f = 999.83, and g = 0.016879.

6. Simulation results with laboratory test heat exchanger

6.1 Results with detailed model

6.1.1 Fluid flow field

The test case of fouling test apparatus was simulated with the detailed fouling model applying the Eulerian two fluid model. The forces due to the diffusion and drag were included, and the effect of the lift force was examined. The Eulerian multifluid model was applied, and smooth, clean stainless steel surface was assumed. For modelling turbulence, the low Reynolds number model of Yang and Shih was applied. The fouling rate of the heated surface was monitored, and the magnitude of the forces affecting on the fouling was studied.

Figure 25 shows the contours of the flow field. The fluid temperature increases towards the outlet a few degrees as the fluid passes the heated wall. The fluid flow has developed close to the turbulent channel flow at the midway of the apparatus. Near the outlet and inlet, the geometry of the apparatus causes some turbulence to the flow.

In Figures 26–28, the results are shown in more detail. Figure 26 shows the temperature distribution. In the vicinity of the wall, the temperature decreases linearly as a function of the distance from the wall. Figure 27 shows the results for the particle volume fraction and velocity magnitude distribution near the heated wall. The results are presented on the planes at three distances from the inlet (see Figure 24).

Figure 28 shows the ratio of acceleration due to the turbulent diffusion and Brownian diffusion calculated from equation (2.1.1). The Brownian diffusion is dominating within around ten micrometres from the wall. Further away from the wall, the turbulent diffusion is more important.

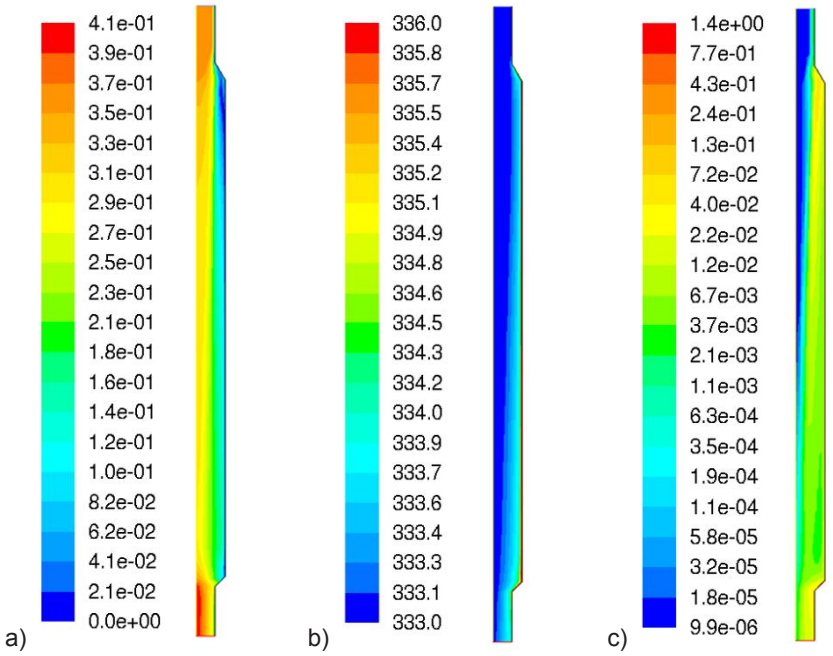

Figure 25. The simulation results: a) Fluid velocity magnitude (m/s) b) Fluid temperature (K), c) Turbulent energy dissipation (m^2/s^3).

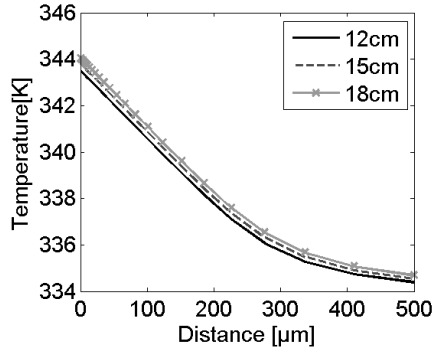

Figure 26. Temperature (K) profile near the heated wall. Lines correspond to different distances from the inlet, see Figure 24.

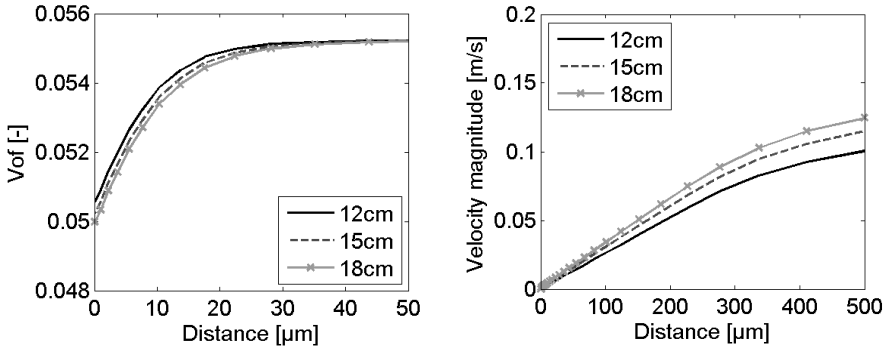

Figure 27. Results in the vicinity of the heated wall. On the left: Particle volume fraction. On the right: particle velocity magnitude (m/s). Lines correspond to different distances from the inlet, see Figure 24.

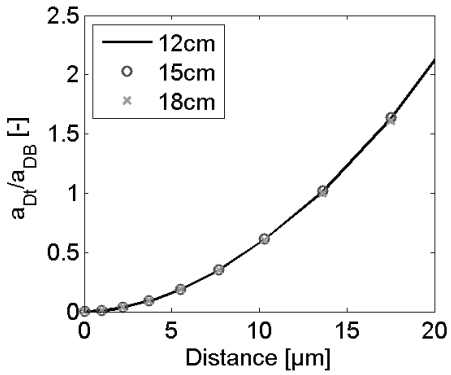

Figure 28. Ratio of acceleration due to turbulent diffusion a_{Dt}, and Brownian diffusion a_{DB}, as a function of distance from the heated wall.

6.1.2 Comparing the forces arising from diffusion and lift

In order to compare the forces due to diffusion and lift, the corresponding accelerations are presented in Figure 29. The particle acceleration $\mathbf{a_p}$ was derived from the calculated total force $\mathbf{F_{tot}}$ per unit volume

$$\mathbf{a_p} = \frac{\mathbf{F_{tot}}}{\alpha_p \rho_p} \tag{6.1.0}$$

where

$$\mathbf{F_{tot}} = \mathbf{F_{diff}} + \mathbf{F_{lift}} \tag{6.1.1}$$

was calculated from equations (2.1.0) and (2.1.3).

In Figure 29, the particle acceleration is shown at distances 12 cm, 15 cm and 18 cm from the inlet. The magnitude of the lift force was found to be negligible compared to the force due to diffusion.

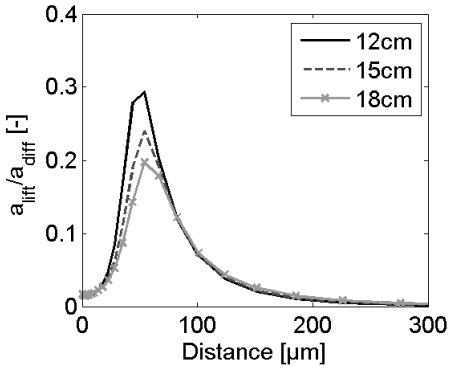

Figure 29. Particle acceleration due lift force versus diffusion at the near wall region. Lines correspond to different distances from the inlet, see Figure 24.

6.2 Simulation results with Wall Function Approach

6.2.1 Verification with detailed model

The same experiment calculated with detailed particulate fouling model was calculated by applying the wall function approach. Similarly with the detailed model, a smooth, clean stainless steel surface was assumed. The experiment was modelled both with the Eulerian multifluid model and the algebraic slip mixture model (ASM). The standard k-ε model with enhanced wall treatment was used for turbulence. Otherwise the same models were used as with the detailed modelling.

The results of fouling rates obtained with the two fouling models along the heated wall are compared in Figure 30. The results calculated with detailed fouling model including also the lift force are presented in Figure 30. As shown in Figure, the effect of the lift force on the fouling rate was insignificant.

The results of the wall function model are in good agreement with the detailed model results justifying the use of the wall function model. The discrepancy between the results of the Eulerian detailed model and the wall function approach may be due to the different models for turbulence. The standard k-ε model with

enhanced wall treatment was used for turbulence with wall function approach, and the model of Yang and Shih low-Reynolds number k-ε model (1993) was applied with the detailed models. Larger differences observed at the ends of the test section are caused by the expansion or contraction of the channel disturbing the flow.

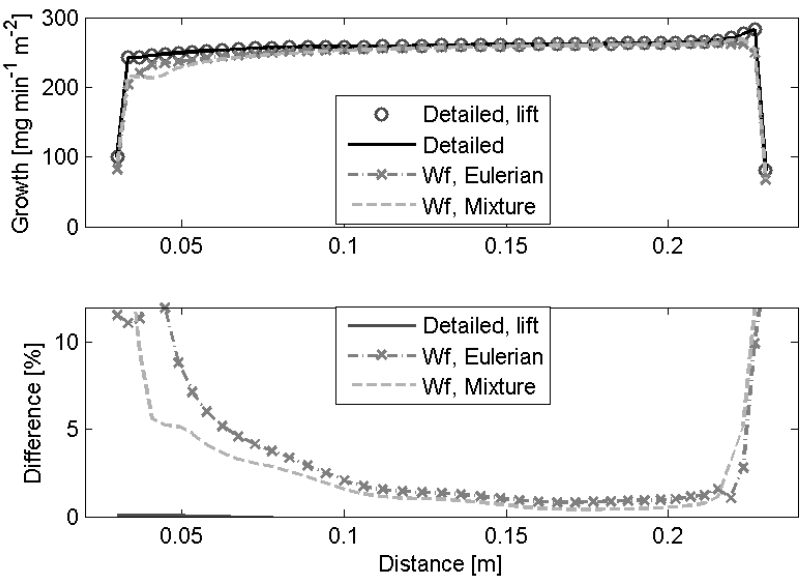

Figure 30. Fouling rate along the heated wall. X-axis shows the distance from the inlet. Results are shown for simulations with the detailed model and with the wall function approach (Wf) with the Eulerian multiphase model and the mixture model (ASM). The relative difference of the wall function and the detailed calculation results are shown at the bottom. The results with detailed model including lift force are shown with solid line.

The difference between the result of the wall function model with the algebraic slip mixture model (ASM) and the Eulerian model is insignificant as shown in Figure 30. The mixture model was applied in the rest of the simulations as a less expensive method.

In Figure 31, the turbulent kinematic viscosity predicted in the near wall region as a function of y^+ is shown for the results calculated with the standard k-ε model with enhanced wall treatment, Yang and Shih low-Reynolds number k-ε model (1993) and with the model of Johansen (1991) according to equation (3.1.8). The model of Yang and Shih low-Reynolds number over predicts the turbulent viscosity in the region $y^+ < 0.4$ in comparison with the standard k-ε model and with the model of Johansen (1991).

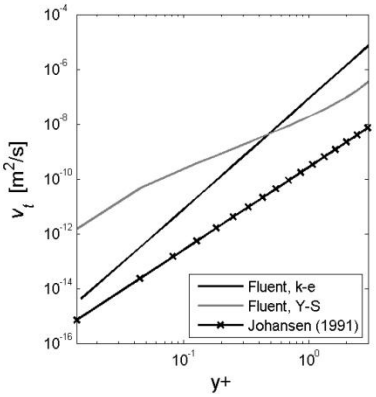

Figure 31. Turbulent kinematic viscosity in a near wall region as a function of y^+.

According to the results in Figure 31, the turbulence model applied had an effect on the simulated results compared in Figure 30. However, due to the long simulation time with the detailed fouling model, the results were not recalculated with the standard k-ε-model with enhanced wall treatment (EWT).

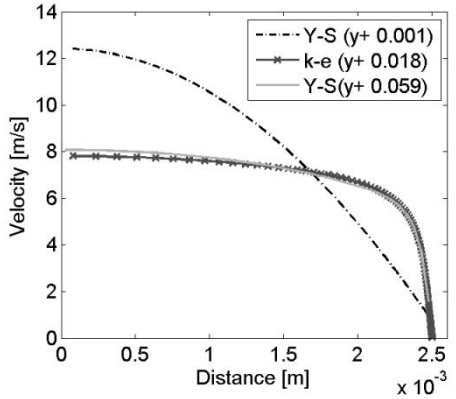

Figure 32. Velocity profile in a channel calculated with several grids (y^+ at the wall). YS – Yang and Shih model, ke – standard k-ε model with EWT.

The low Reynolds number turbulence model of Yang and Shih was studied further in order to validate its applicability in the case of industrial test heat exchanger case, where the Reynolds number is low due to very viscous fluid. The model was tested in a simple channel flow test case, and compared with the standard k-ε model with enhanced wall treatment. With the same initial parameters, the standard k-ε model with EWT predicted for the y^+ = 0.018, whereas the model of Yang

and Shih predicted the y^+ value to be 0.0013, and the laminar flow profile was produced, see Figure 32. If the near wall grid size was enlarged, so that the y^+ value was 0.059, the velocity profile was in good agreement with the profiles predicted by the standard k-ε-model with EWT, see Figure 32.

The low Reynolds number k-ε models are approaches, where the behaviour of eddy viscosity is corrected with damping functions (White, 1991). The models may mispredict the behaviour of k and ε near the solid walls. In here, the model of Yang and Shih might underpredict the production of turbulent energy, and therefore the flow is laminarized. The results showed that the model is not applicable in the cases with very small y^+ values.

6.2.2 Comparison against experimental data

In the comparison of the simulated results with the experiments described in Section 5, the surface was assumed to be fouled, and the properties of the fouled layer were applied. The simulation results with wall function approach are compared to the experimental fouling rates in Figures 33 and 34.

The calculated magnitude of the fouling rate was close to the experimental results, but the dependency on the heat flux or the mass flow rate of the slurry in the simulations was not as strong as in the experiments. The simulated deposition rate dependency on the flow rate was clearly too weak, as shown in Figure 33. At higher flow velocity, the predicted deposition rate was higher than the experimental results. At the lowest velocity, the predicted deposition rate was lower than the experimental result.

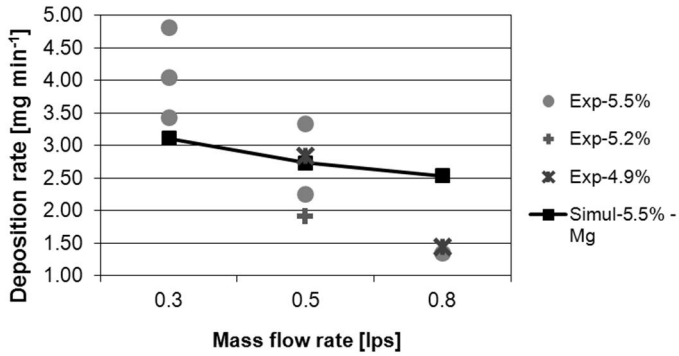

Figure 33. Mass deposition rate as a function of fluid flow rate with 5.5 vol% (13.9 wt%) particle concentration and heat flux of 21 kW/m^2. The simulation results are shown for the surface consisting of 8.2 wt% magnesium (Ojaniemi *et al.*, 2012).

The dependency of simulated results on the heat flux was in agreement with the experimental results for the particle concentration of 4.9%, Figure 34. The magni-

tude of the simulated results was 3–8% lower in comparison with the experimental values. The experimental results for slightly higher particulate concentration 5.2% were lower in comparison with the experimental results with the particle concentration of 4.9%, and the behaviour was different. In order to have a reliable comparison, there should have been more experimental results.

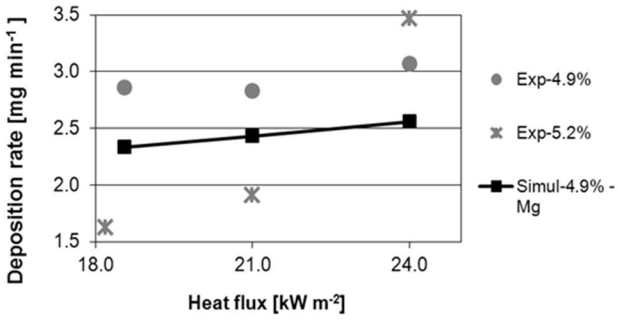

Figure 34. Mass deposition rate as a function of heat flux with 4.9 vol% (12.5 wt%) particle concentration and mass flow rate of 0.5 lps. The simulation results are shown for the surface consisting of 8.2% magnesium (Ojaniemi *et al.*, 2012).

The mass transfer rate was dependent on temperature via the viscosity and water permittivity. In the simulations, the heat flux was applied as the boundary condition for the heated wall and the wall temperature was based on the given flux. In the fouling experiments, the temperature was measured from the interface of heated copper block and stainless steel rather than directly from the steel surface contact with fluid. The effect of the coupling agent between the copper and steel test plate was evaluated separately by measuring the temperature of the heating element and the test stainless steel surface for the applied heat fluxes. The temperature difference between the measurement points was 2.3 to 3.0 degrees depending on the heat flux. This correction was applied to the measured temperatures when comparing to the simulation results in Figure 35. The predicted temperature deviated from the measured result by a few degrees (Ojaniemi *et al.*, 2012).

The difference in the temperature between experimental and simulated values was highest in the cases of the lowest mass flow rate and the highest heat flux, see Figure 35. In these cases, the simulated fouling rates also deviated from the experimental values, as observed in Figures 33 and 34. The calculated particulate fouling rate depends on the temperature and the simulated lower deposition rate is a result of the lower wall temperature in the simulation (Ojaniemi *et al.*, 2012). The heat transfer is controlled by turbulent diffusion, except very close to the wall. It is possible that the modelling of turbulence is less accurate for the smaller mass flow rates, i.e., smaller Reynolds number.

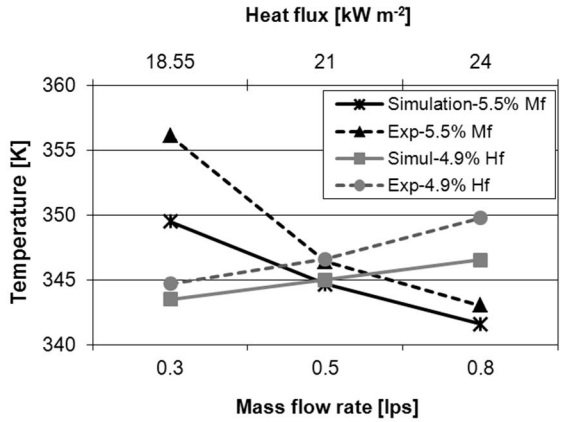

Figure 35. Wall surface temperature, solid line for simulated and dashed line for the experimental results. Results are shown as a function of fluid flow rate (Mf, axis on the bottom, dark lines) for 5.5 vol% particle concentration and heat flux of 21 kW/m^2. As a function of heat flux (Hf, axis on the top, light lines), the results are shown for 4.9 vol% particle concentration and mass flow rate 0.5 lps (Ojaniemi *et al.*, 2012).

Several experiments of fouling of heat exchangers with liquids are presented in literature, while most of the present studies are for gas-particle processes. Quan *et al.* (2008) studied the fouling of heat transfer surface during convective heat transfer with calcium carbonate solution. The fouling was due to scaling and particles formed in a liquid due to crystallization. The results for fouling rate showed similar behaviour under the varied process parameters: the fouling rate increased with the decreasing fluid velocity, the increasing water hardness, and the increasing temperature of the heat transfer surface. Similar results were obtained also by Müller-Steinhagen *et al.* (1988) with alumina particles suspended in water.

6.3 Effect of particle size distribution on fouling rate

Including the particle size distribution in the simulation would be computationally demanding. Therefore only the estimated effective particle size was applied in the simulations (see Ojaniemi *et al.*, 2012). However, the effect of particle size distribution was tested by simulation with several particle size classes. The effect of the particle size distribution was tested with two experimental distributions, measured with Sedigraph and Delsa Nano C (Puhakka *et al.*, 2013). The measurements were done for the same industrial process fluid, but different samples taken from different parts of the process. The measurements were able to distinguish particle sizes greater than 200 nm. In order to have an estimate for the smaller sized particles, the measurement results were fitted with log-normal distribution. In Figure 36, the measured distributions and the fitted log-normal distributions are shown.

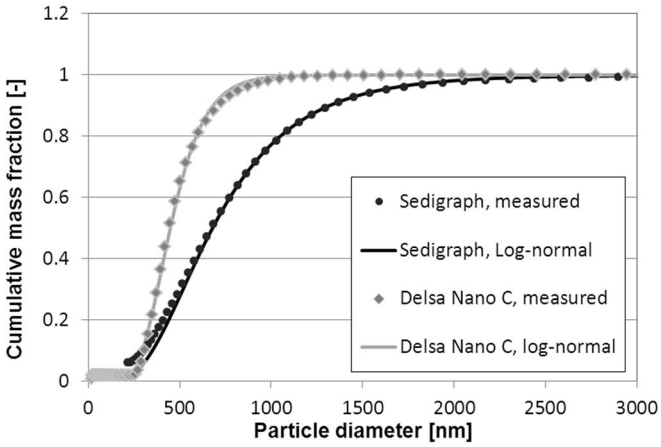

Figure 36. The particle size distributions measured with Sedigraph and Delsa Nano C with the log-normal fitted distributions (Puhakka *et al.*, 2013).

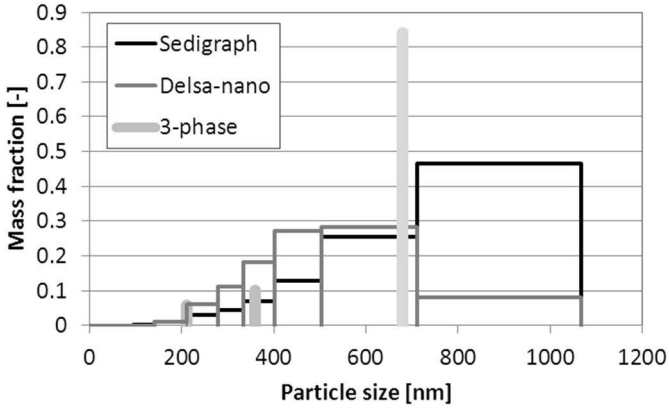

Figure 37. The mass fraction of the size classes based on the fitted distributions. The mass fractions applied with the 3-phase test in determining the effective particle size are shown by bars (Puhakka *et al.*, 2013).

Based on the fitted distribution, nine particle size classes were determined: 75 nm, 113 nm, 169 nm, 253 nm, 303 nm, 365 nm, 437 nm, 570 nm and 854 nm. The width of the size classes and the mass fraction of each class are shown in Figure 37. The mass fractions applied with the 3-phase test in determining the effective

particle size are shown by grey bars. The test was done with particle sizes 210 nm, 360 nm and 680 nm. The fractions were based on the measurement with Sedigraph.

The simulation result for the deposition rate calculated with the particle size distributions are shown in Figure 38. The deposition rate for each size class is presented for both distributions applied. The effect of the particle size distribution showed to be directly comparable to the deposition rate: if the mass fraction of the small size classes is increased, the total deposition rate is increased due to the strong dependency of the deposition rate on the particle size (Puhakka *et al.*, 2013). The smaller the particle size, the stronger is the deposition rate. This is in accordance with the results presented e.g. by Müller-Steinhagen et al (1988).

The size classes of large particles did not have an effect on the total deposition rate: the mass fraction of the last size class was five times larger with the distribution based on the measurement with Sedigraph in comparison to the distribution based on the Delsa Nano C measurement (Figure 37). However, the deposition rate shown in Figure 38 for the ninth class for both of the simulations was negligible. The total deposition rate with the distribution based on the measurements with Sedigraph was 1.71 mg/min, and with Delsa Nano C 3.23 mg/min. Maximum deposition rate was obtained around particle size class of 253 nm.

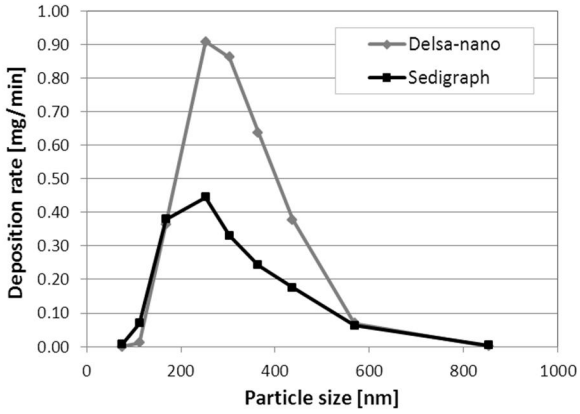

Figure 38. The calculated deposition rate (mg/min) of the nine size classes based on the fitted distributions (Puhakka *et al.*, 2013).

With the effective particle size 387 nm, the result for the deposition rate was 2.75 mg/min. That is larger than the result calculated based on the corresponding particle size distribution measured with Sedigaph, 1.71 mg/min. The determination of the mass fractions with 3-phase calculation was based on the same measured particle size distribution. As seen in Figure 36, the fraction of smallest particle size is larger in measurements than in the fitting. The calculation with nine size classes was based on the fitted size distribution. Actually the mass fraction applied for 210

nm particle is closer to the mass fraction distribution based on the Delsa Nano C measurements (see Figure 37). Thus, the deposition result is also closer to the results with calculated the distribution based on the Delsa Nano C measurement.

In addition, the deviation between the results might be also due to the different turbulence model applied. With the 3-phase testing, low-Reynolds number k-ε model of Yang and Shih (1993) was applied. The model of standard k-ε model with EWT was used in calculations with nine size classes.

6.4 Comparison of models for thermophoresis

6.4.1 Evaluating magnitude of thermophoresis

The wall function approach including thermophoresis was implemented in Fluent 14.0 with user defined functions (UDF). As stated in Section 2.1.3, thermophoresis is related with the temperature gradient, which is present in the near wall region of the heated surface. According to Figure 26, the turbulent diffusion overcomes the effect of Brownian diffusion at the distances more than around ten micrometres from the wall surface. Therefore, in order to evaluate the need to include the thermophoresis also into the outer region of the near wall, i.e. into the computational cells beyond the cells adjacent to the wall, comparison of the forces due to turbulent diffusion and thermophoresis was carried out. The results are shown in terms of the corresponding accelerations $\mathbf{a_{th}}$ and $\mathbf{a_{tdiff}}$ derived from the calculated forces per unit volume based on the equation (6.1.0).

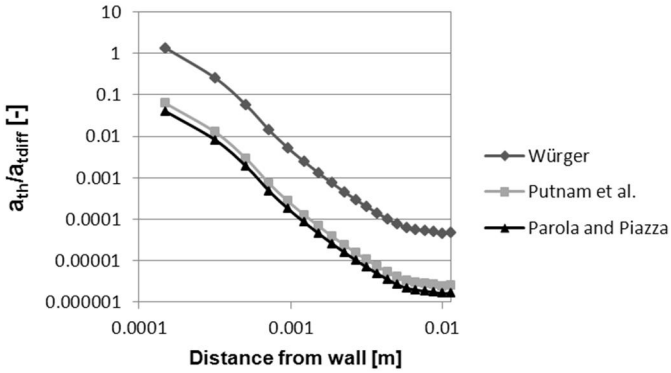

Figure 39. Ratio of acceleration due to thermophoresis, a_{th}, and acceleration due to turbulent diffusion, a_{tdiff}, as a function of distance from the heated wall. Results are calculated using three different Soret coefficient models.

Figure 39 shows the relative acceleration due thermophoresis in comparison to acceleration due to turbulent diffusion for the three Soret coefficients. According to models of Parola and Piazza (2004) and Putnam *et al.* (2007), equations (2.1.4) and (2.1.5), the effect of thermophoresis in comparison to turbulent diffusion is restricted only into the cells adjacent to wall. With the model of Würger (2009), equation (2.1.6), the effect penetrates deeper into the domain. However, the thermophoresis was included only into the near wall region in the wall function approach.

6.4.2 Simulation results with thermophoresis

In Figure 40, the deposition rate calculated including the thermophoresis on the heated wall is shown as a function of distance from inlet (Ojaniemi *et al.,* 2013). For comparison, the simulation results without the thermophoresis for the same case are shown. The models of Putnam *et al.* (2007) and Parola and Piazza (2004) seem to have only minor effect on the deposition rate in the simulated case. The model of Würger (2009) predicted greater effect, and the effect would be even greater if thermophoresis would be included in the domain next to the cells adjacent to the heated wall. In comparison to the experimental values (Ojaniemi *et al.,* 2013), the effect of Würger model seems to be too strong.

In Table 7., the differences of the predicted deposition rates with the applied models in comparison to the results with standard k-ε with EWT in 2D are presented. The averaged experimental value was 130 mg/m^2/min. Due to the large range of predicted values with the models presented in literature, the effect of thermophoresis was excluded from the final model.

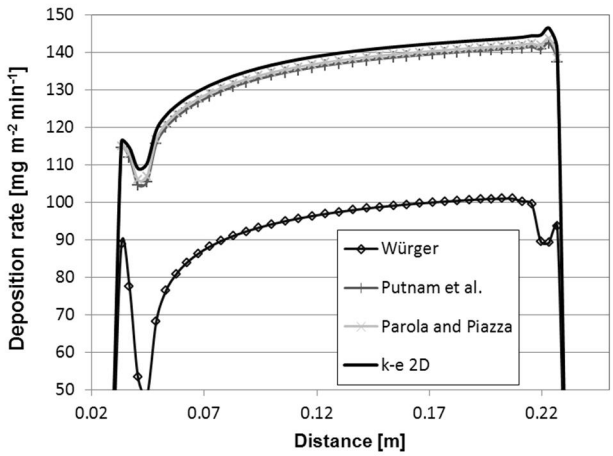

Figure 40. Deposition rate on the heated wall as a function of distance from inlet, mg/m^2/min (Puhakka *et al.*, 2013).

Table 7. Deposition rates predicted with the applied models for thermophoresis (Ojaniemi *et al.,* 2013).

	mg/m^2/min	%
k-ε, 2D, no Soret	136	
Putnam *et al.*	133	-2.2
Würger	92	-32.1
Parola and Piazza	134	-1.5
Experiment	130	

6.5 Comparison of results with LES and k-ε RANS model in 3D

The shear stress is one of the major effects in the particle re-entrainment implying that the realistic modelling of turbulence is essential. The CFD simulations of a test heat exchanger were performed with Large Eddy Simulation (LES) in 3D and compared to the results calculated with standard k-ε model with enhanced wall treatment (EWT) in 2D and 3D (Ojaniemi *et al.,* 2013). The Reynolds number of the test case was 6200. The wall function approach without thermophoresis was applied.

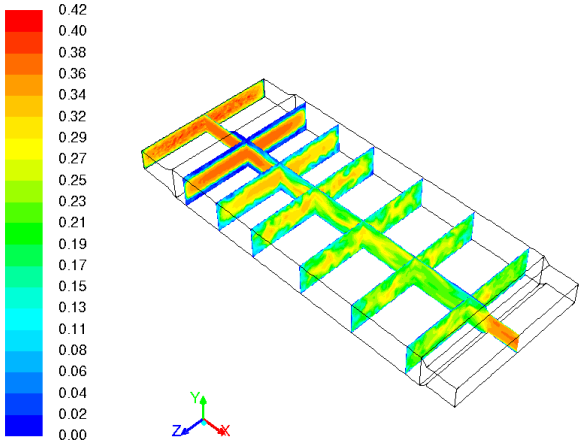

Figure 41. Instantaneous velocity magnitude, m/s, LES. Flow is in the direction of x-axis (Ojaniemi *et al.,* 2013).

Figure 41 shows, how the unsteady turbulent flow develops into the domain. In Figure 42, the sub grid turbulent viscosity is presented at the heated wall. The turbulent viscosity resulting from the modelling of the small scales eddies is insignificant implying that the relevant turbulence is resolved in the grid. A smaller eddy viscosity to viscosity ratio is predicted with LES than with the k-ε model with EWT, showing the LES modelling to be appropriate.

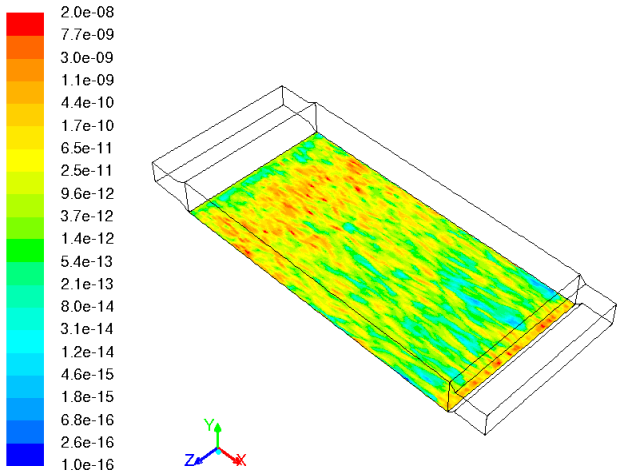

Figure 42. Profile for instantaneous sub grid turbulent viscosity at the heated wall. Logarithmic scale (Ojaniemi *et al.,* 2013).

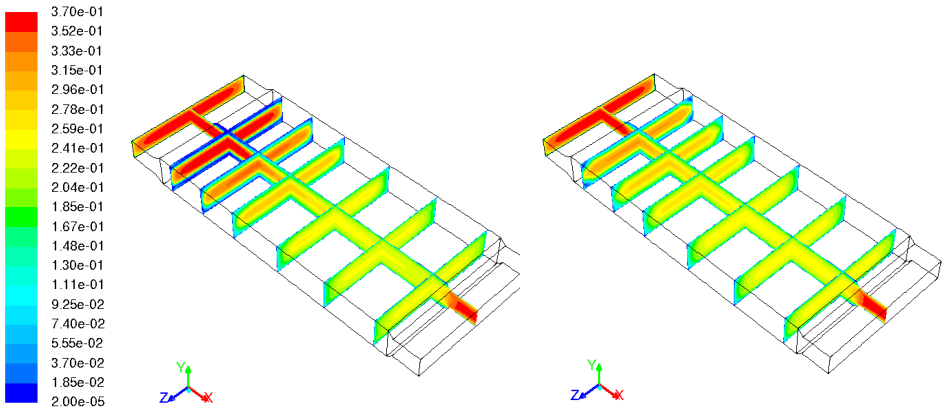

Figure 43. Velocity magnitude, m/s. On the Left: LES, time averaged result. On the Right: Standard k-ε with EWT, instantaneous velocity field. Flow is in the direction of *x*-axis (Ojaniemi *et al.,* 2013).

In Figure 43, the results for velocity magnitude in the heat exchanger are shown for simulation with LES and with standard k-ε model with EWT. The results for LES are time averaged from the simulation period of 72.4 s. The profiles for the results are quite different. LES model predicts the high-velocity flow to penetrate a longer distance into the domain than k-ε model. In generally, the k-ε model is known not to be able to predict well the separation point of step geometrics. The difference in the predicted results for velocity magnitude in the near region of the step geometry is shown in Figure 44. The flow field formed in the corner of the geometry is significantly different in the form of the eddy and in the magnitude of velocity.

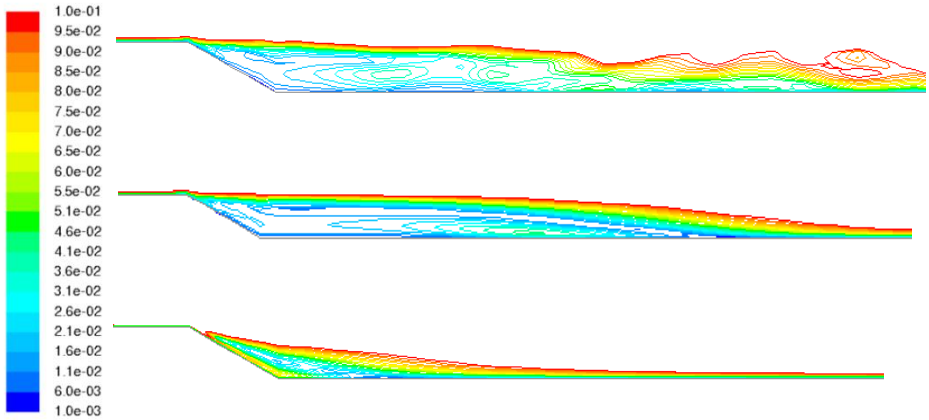

Figure 44. Velocity magnitude, m/s. On the top: LES, instantaneous velocity field. At the middle: LES, time averaged result. At the bottom: Standard k-ε with EWT, instantaneous velocity field. Flow is in the direction of *x*-axis.

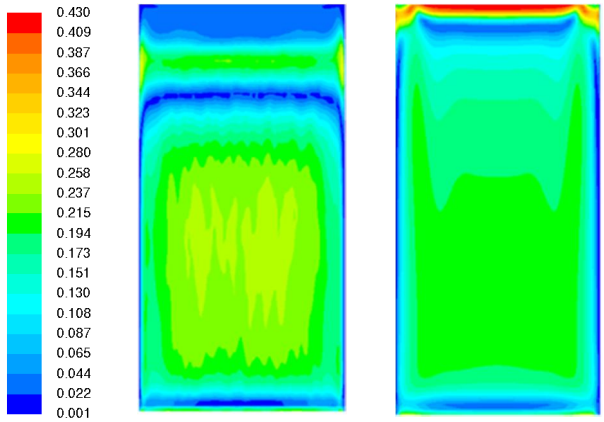

Figure 45. Shear stress at the heated wall, Pa. On the left: LES, time averaged result. On the right: standard k-ε with EWT. Flow is directed downwards (Ojaniemi *et al.,* 2013).

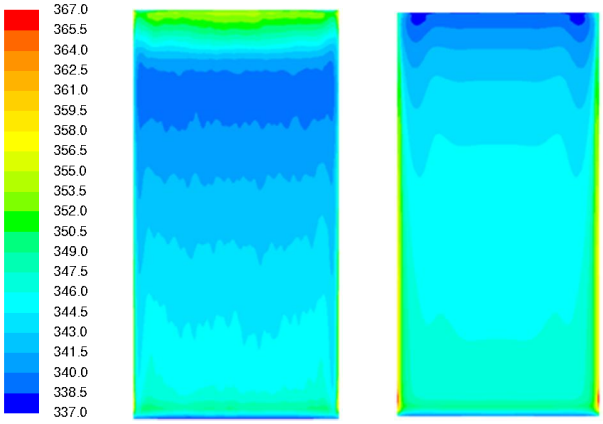

Figure 46. Temperature at the heated wall, K. On the left: LES, time averaged result. On the right: standard k-ε with EWT. Flow is directed downwards (Ojaniemi *et al.,* 2013).

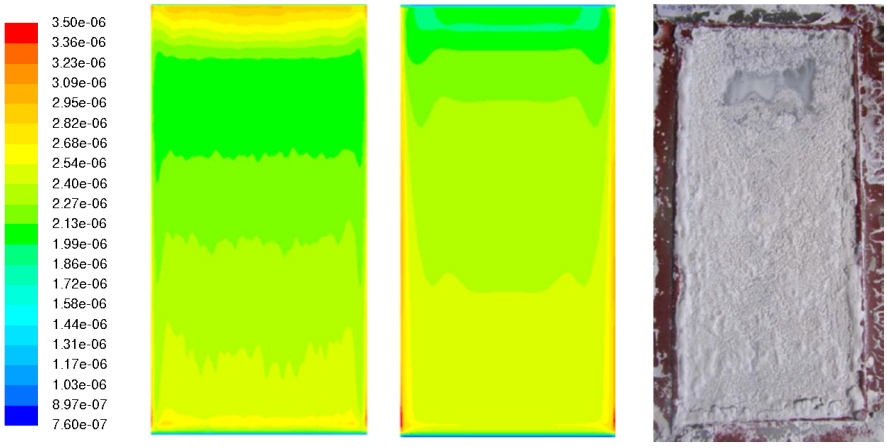

Figure 47. Deposition flux to the heated surface, kg/(m^{2}s). On the left: LES, time averaged result. At the middle: standard k-ε with EWT. On the right: Experimental results for deposition profiles. T_{fluid}=333 K, 0.45 lps, 30.2 kW/m^2, s.c. 50.7%. Flow is directed downwards (Ojaniemi *et al.,* 2013).

The difference in the predicted results with LES and with standard k-ε model with EWT is seen in the profiles of shear stress and temperature at the heated wall, see Figures 45 and 46. Since the flow velocity profiles are different, the resulting temperature distributions also differ. The temperature increases near the edge of the inlet as the flow is less mixed.

The temperature and shear rate effects on the fouling rate, thus the different results produced by the models are also seen in the distribution of deposits at the heated wall, see Figure 47. The LES model predicts stronger fouling rate at the edge of the heated wall near the inlet. According to the results with standard k-ε model with EWT, the fouling rate is higher in the corners near the outflow. Qualitatively the deposition profiles of the LES simulation results are closer to the experimental results showing the region with decreased fouling rate to be further away from the flow inlet. Example of the deposition on test plates in experiments is shown in Figure 47. The experiments were done with higher particulate concentration of 50.7% where the non-uniform deposition is clearly seen.

In Figure 48, the differences of the predicted deposition rates with the applied methods for modelling turbulence are presented along the heated wall. The results for 3D simulations are shown from the centre line along the fluid flow (see Figure 24.). The difference between the results with standard k-ε model with EWT in 2D and 3D in the total deposition rate on the heated surface is order of 3.9% the result for 3D being larger. The increased deposition rate in the corners of the heat exchanger resulted in increased averaged fouling rate with the standard k-ε EWT model in 3D. Occasionally, the difference between the results with standard k-ε model with EWT in 3D and LES is only 1.4%, although the profiles for the deposition rate are significantly different. The values are presented in Table 8.

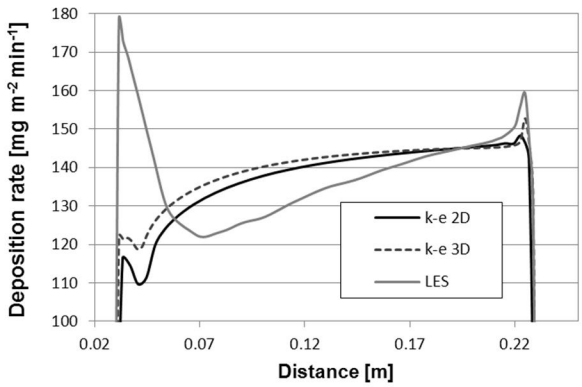

Figure 48. Deposition rate on the heated wall as a function of distance from inlet, mg/m^2/min.

Table 8. Deposition rates predicted with the applied methods for modelling turbulence (Ojaniemi *et al.,* 2013).

	mg/m^2/min	%
k-ε, 2D [*)]	136	
k-ε , 3D	141	3.9
LES, 3D	138	1.4
Experiment	130	

[*)] In Table 7, case is referred as ' k-ε, 2D, no Soret'

7. Modelling fouling with industrial test heat exchanger

7.1 Industrial test heat exchanger

The high efficiency corrugated plate heat exchanger (CHE) was used as an industrial test case. The test heat exchanger consisted of twenty corrugated Alfa Laval M3 chevron plates having ten slits for the slurry fluid. The slurry is warmed up with water steam flowing in opposite direction in the slits between the slits with slurry flow (see e.g. Kerner, 2011, for the illustration of the high efficiency corrugated plate heat exchanger). Fouling in a similar plate heat exchanger was studied also by Zettler *et al.* (2005). The depth of the corrugated surface was 2.4 mm, which is rather shallow in order to generate turbulent flow with high wall shear stress with relatively low channel flow velocities. Corrugated heat exchanger has been investigated also by Gradgeorge *et al.* (1998), Zhang, G-m. *et al.* (2013) and Li *et al.* (2013).

Only one pair of the plates of the equipment was modelled, see Figure 49. The computational domain was selected so that it has the full width of the slit, but only a part of the height of the equipment. The width of the numerical grid is 10 cm, the height is 6 cm and the distance between the plates is 4.8 mm at maximum. The total height of the plate was 43 mm. The grid size was 680 000 cells consisting mostly of tetra cells, with hexa cell inflation at the surface, as shown in Figure 49. The grid included the contact points of the plates as small holes.

The simulations were carried out with the assumption of fouled layer existing on the surface. For modelling the particulate fouling, the wall function approach without thermophoresis was applied. The material properties shown in Table 9 were applied. The presence of additional salt of magnesium and silicates were included into the model as a deposition layer component according to Section 2.5. The value applied for zeta potential of dolomite was –18 mV and for calcite particle, –20 mV (Riihimäki *et al.*, 2010). The zeta potential of –20 mV was taken for the stainless steel surface in simulations where the clean surface was assumed.

Table 9. Material properties and boundary conditions of the industrial test case modelled.

Density of particles ($CaCO_3$) , kg/m^3	2711
Zeta potential of particles, mV	-20
Thermal conductivity of particles, W/(m·K)	2.7
Specific heat of particles, J/(kg·K)	856
Representative particle diameter, nm	387
Mg^{2+} content of fouled layer, -	0.08
Silicates content of fouled layer, -	0.184
Ion strength, mol/dm^3	0.0044
Flow rate, m/s	0.7
Particle concentration at inlet, wt%	49, 58
Temperature of slurry at inlet, K	368

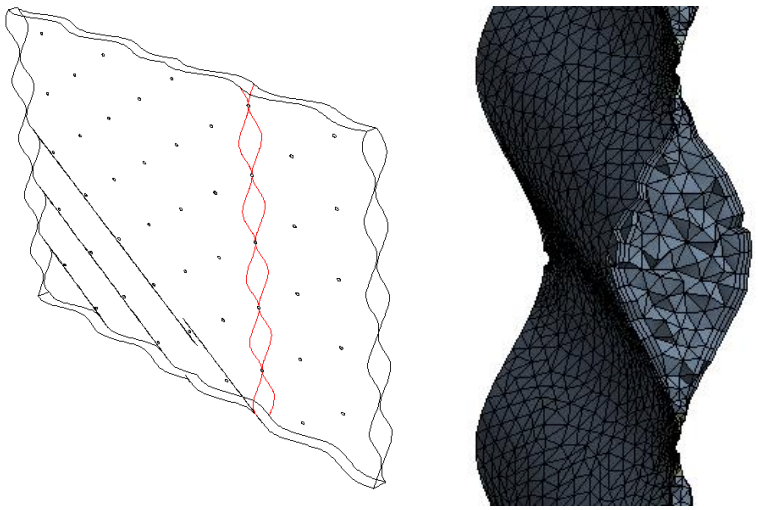

Figure 49. Computational geometry for the industrial test heat exchanger. Simulated results are presented on the plane shown with red vertical lines, and on the line at back plate. On the right: cross section of the grid. Flow is directed downwards.

The mass flow of the slurry decreased during the experiments with the industrial test heat exchanger in average 6.6% in a day. In modelling, the averaged flow velocity magnitude applied was 0.7 m/s. The fluid temperature at the inlet of the heat exchanger was 368 K. The plates of the heat exchanger were heated with water steam. The boundary condition of constant temperature was applied on the walls. The models for temperature dependency of water density and viscosity described in Section 5.5 were applied. Simulations were carried out as time dependent calculations with time step of 0.01s.

The particle concentration of 58 wt% was applied in modelling (Ojaniemi *et al.,* 2012). The particle concentration of 49 wt% was also studied. The model for viscosity of the suspension was derived based on experiments as described in next Section 0. Reynolds number of the simulated cases was around 1000. The standard k-ε model with EWT model was used for modelling turbulence of the non-Newtonian fluid flow. The standard approach for the near wall turbulence modelling does not take into account the rheology of the suspension. According to this, the estimates for the shear stress at the wall τ_w, and therefore the velocity profile, are mispredicted for fluids with non-Newtonian rheology.

With the model of standard k-ε with enhanced wall treatment (EWT), the flow field is calculated based on one-equation turbulence model with the grid to the wall, including also the viscous sub layer. The standard wall function is applied only in the buffer region as blended with the one-equation turbulence model. In the viscous sublayer of turbulence, the velocity profile is linear for Newtonian fluids, $u^+=y^+$. For power law fluids, the corresponding equation is $u^+=(y^+)^{1/n}$, with power law index n (Holland and Bragg, 1995). Thus, the fluid flow velocity for the shear thickening non-Newtonian fluids is decreased in the near wall region in comparison with the velocity of Newtonian fluid.

In the method applied for modelling turbulence, the non-Newtonian viscosity is taken into account. The effect of the viscosity is considered also in the wall function approach of modelling particulate fouling. Therefore, the rheology is taken into account in the near wall region in the velocity profile and in the fouling rate.

7.2 Non-Newtonian viscosity

Industrial processes with high solid content suspensions may have strong variations in viscosity with increasing shear rates, i.e. the suspension exhibits non-Newtonian viscosity behaviour (Riihimäki, 2013). For measuring the non-Newtonian viscosities, rotational methods are typically applied. The viscometers of Brookfield DV-II (spindle ULA-DIN-87), Hercules DV-10 Hi-Shear viscometer with the bob types A and E, and MCR 302 CP 50, Anton Paar, were applied in measurements (Riihimäki, 2013).

At the low concentrations, the test fluid can be considered to behave like a Newtonian fluid at shear rates below a few hundred 1/s. As the concentration increases, the fluid starts to behave as a shear-thinning fluid. The viscosity results for the fluid without dispersants are higher than with them. At the higher shear

rates the fluid is shear-thickening, and the viscosity increases as the concentration increases. The temperature dependence of water is a reasonable approximation at shear rates from 65 up to 20 000 1/s and with solid contents from 0 to 72 wt% (Riihimäki, 2013). The viscosity measurement of slurry with extremely high particle content was demanding, and reliable results were not obtained for the slurries with the highest solid content at high shear rates.

The results for measured viscosities (Riihimäki, 2013) were fitted with the power law model (Ostwald – de Waele model)

$$\mu = m\dot{\gamma}^{n-1} \tag{7.2.0}$$

for obtaining the non-Newtonian viscosity model in the case of industrial test heat exchanger. The measurements were available for the suspensions with solid content of 44, 53 and 65 wt%. The models for the suspensions with solid content of 58 wt% and 49 wt% were derived as weighted average from the models for the suspensions with measured concentrations. The parameters for the resulting model for the non-Newtonian viscosity with solid content 58 wt% are n = 1.5065 and m = $4.603 \cdot 10^{-4}$ and the minimum viscosity at temperature of 298 K is 14.4 mPas, see Figure 50. The range of validity is from 100 to 20 000 1/s. The model for the slurry with solid content of 49 wt% is also presented in Figure 50 with the parameters n = 1.3418 and m = $4.930 \cdot 10^{-4}$ and the minimum viscosity 4.9 mPas at temperature of 298 K.

The non-Newtonian viscosity models were applied in the CFD simulation of industrial test heat exchanger. The viscosity correlations were implemented with UDFs for the mixture viscosity of the ASM multiphase modelling method.

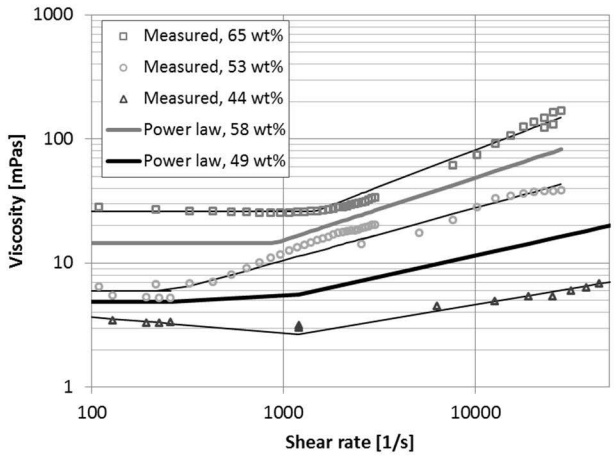

Figure 50. Power law fitted viscosity as a function of shear rate shown with lines Experimental data is presented with marks.

7.3 Comparison of simulated results with experimental results

Figure 51 shows the distribution of deposits on a plate according to the simulation results and experiments. The calculated distribution of the deposits is qualitatively correct. The largest deposits are located near and below the contact points of the plates. Some fouling also occurs in the bottom of the grooves. The distribution of the deposits is qualitatively similar in the simulations as in the fouling tests.

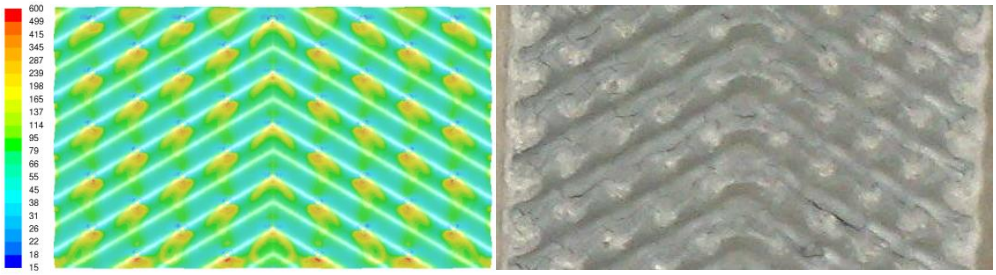

Figure 51. Deposits distribution on the surface of heat exchanger, logarithmic scale. On the left: simulation result for the deposition rate (g/m^{2}day). T_{fluid}=368 K, T_{wall}=373 K, 0.7 m/s, s.c. 58 wt%. On the right: experimental result. Flow is directed downwards.

The simulation result for the fouling rate with the slurry of solids content of 58 wt% scaled to the full size of the heat exchanger plate was 2.7 g/day. The average found in the industrial experiments was 1.9 g/day with the slurry of solids content of 72 wt% (Ojaniemi *et al.,* 2012). However, thermophoresis, surface roughness (including enhanced adhesion and re-entrainment), and effect of crystallization were not included into the model. In addition, the applied solids concentration was lower.

With the slurry of solids content of 49 wt%, the simulated fouling rate was 6.3 g/day. The non-Newtonian viscosity of the slurry was around 2.7 times lower than the viscosity with the slurry with higher concentration of 58 wt%, as seen in Figure 52. The fouling rate resulted to be more than two times higher. Therefore, according to the model, with the increasing slurry viscosity the fouling rate would decrease.

In Figures from 52 to 54, the simulation results are shown in vertical line seen in Figure 49 at the distance of 0.01 m from the axis of the computational grid. The results are shown for temperature, viscosity, shear rate and deposition flux as a function of height of the computational domain.

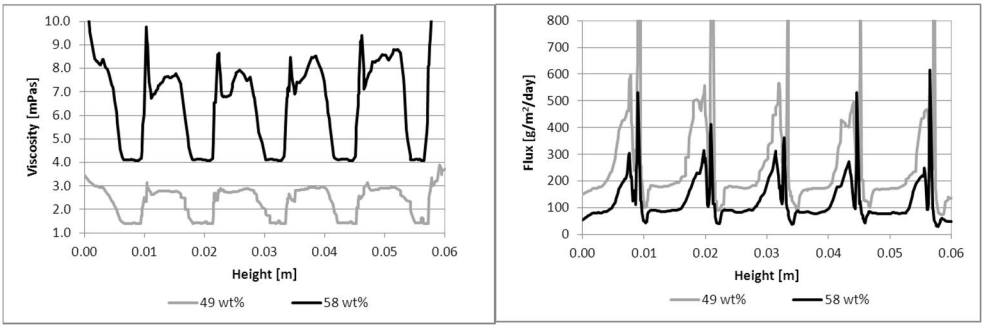

Figure 52. Results with particle concentrations of 49 wt% and 58 wt%, at the vertical line shown in Figure 49. On the left: non-Newtonian viscosity, mPas. On the right: deposition flux to the heated surface, g/(m^{2}day). Flow is directed from right to left.

The profile for non-Newtonian viscosity values are compared with the profiles of temperature and shear rate in Figure 53. Further, the result for deposition flux distribution is compared with the profiles of temperature and non-Newtonian viscosity distributions in Figure 54. The simulation results in Figures 53 and 54 for particulate fouling showed that the fouling rate is dependent both on the non-Newtonian viscosity and temperature. Further, both the non-Newtonian viscosity and temperature are affected by the shear rate: the shear thickening viscosity decreases the fouling rate as the shear rate increases. Temperature increases in the regions with lower shear rate due to decreased heat transfer, leading to increased fouling rate.

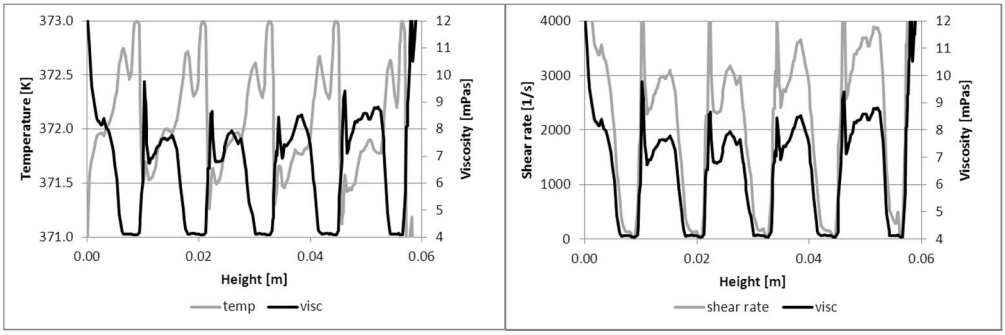

Figure 53. Results for non-Newtonian viscosity, mPas, at the vertical line shown in Figure 49. On the left: Comparison with temperature, K. On the right: Comparison with shear rate, 1/s. Flow is directed from right to left, solids content 58 wt%.

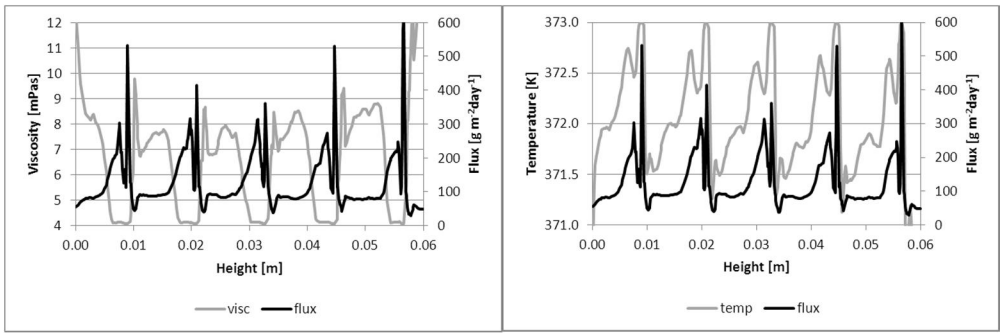

Figure 54. Results for deposition flux to the heated surface, g/(m^{2}day), at the vertical line shown in Figure 49. On the left: Comparison with temperature, K. On the right: Comparison with viscosity, mPas. Flow is directed from right to left, solids content 58 wt%.

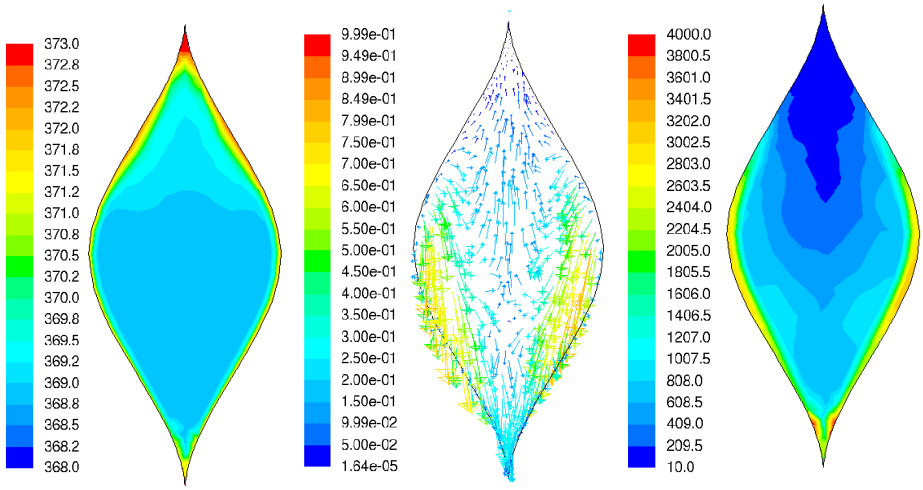

Figure 55. Simulation results in a middle of one knot (see Figure 49): On the left: Temperature, K. At the middle: Vectors of velocity magnitude, m/s. On the right: Shear rate, 1/s. Flow is directed downwards, solids content 58 wt%.

In Figure 55, the results inside a one knot of the plate heat exchanger are shown for the temperature and shear rate, and the vectors for velocity magnitude are presented. The results are shown for the centermost knot in the plane presented with vertical red lines in Figure 49. The region of higher temperature occurs coincidently with the lower shear rate and velocity magnitude regions. In comparison with Figure 54, it is concluded that the stronger fouling rate occurs in the same region. The fouling rate is lower in the region of higher shear rate. That is in good

agreement in the general knowledge of designing of the corrugated plate heat exchangers (Kerner, 2011).

In here, the constant wall temperature was considered. Therefore, the possible fluctuations in the wall temperature due to the varying the mixing conditions on the water steam side of the wall are not included in the present model.

7.4 Estimation of effect of surface properties on fouling rate

The effect of surface roughness on the fouling rate in the laboratory fouling test equipment was shown in Figure 15 and 16 calculated with water viscosity. In the estimation of the effect of roughness in re-entrainment of particles in the industrial test heat exchanger, the non-Newtonian viscosity was applied.

In Figure 56, the expected re-entrainment time calculated from equation (4.3.1) is presented for steel and calcium carbonate surfaces calculated with non-Newtonian viscosities modelled for suspension concentrations of 49 wt% and 58 wt%. The remaining fraction of the particles on the surface at the expected re-entrainment time is presented in Figure 57.

The parameters applied in calculation of the results shown in Figure 56 and 57 are shown in Table 3. For the calcium carbonate surface, the surface energy 0.58 J/m^2 calculated by molecular modelling was applied (Puhakka *et al.*, 2013). The value is not the change in the free surface energy according to the equation (2.4.4) required in the model of Vainshtein *et al.* (1997), but it is the free energy needed in formulating the new surface while splitting the material. In here, the value was applied for to have an estimation of the effect of the surface energy on the re-entrainment of the particles.

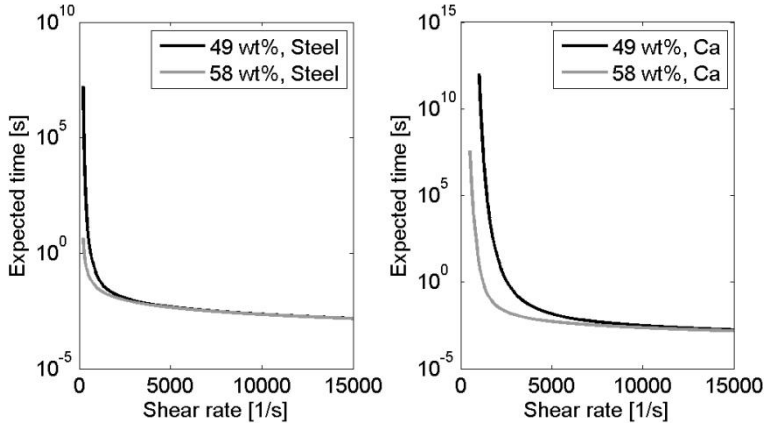

Figure 56. Expected re-entrainment time calculated based on eq. (4.3.1) with non-Newtonian viscosities modelled for suspension concentrations of 49 wt% and 58 wt%. On the left: Steel surface. On the right: Calcium carbonate surface.

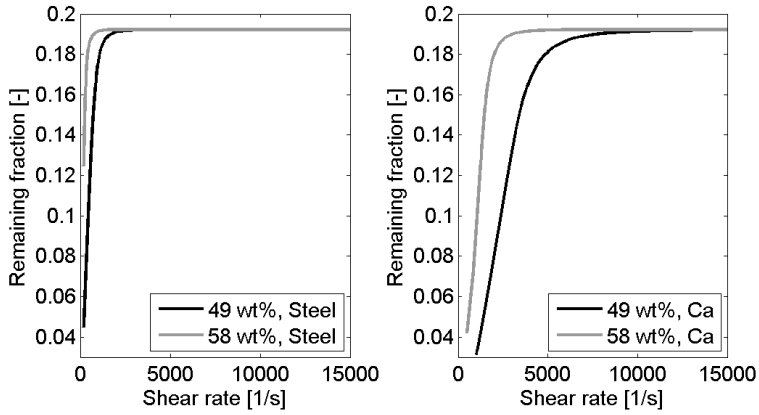

Figure 57. Remaining particle fraction at the expected re-entrainment time with non-Newtonian viscosities modelled for suspension concentrations of 49 wt% and 58 wt%. On the left: Steel surface. On the right: Calcium carbonate surface.

The amount of the particles remaining on the surface is dependent on time the particle has been expired with hydrodynamic forces. The bracketed part of the equation (4.3.2),

$$\left(1-\frac{f_{susp}(t_{\exp})\Delta t}{t_{\exp}}\right) \tag{7.4.0}$$

calculated at time step 0.01 s as a function of shear rate is presented in Figure 58. The time step corresponds with the time step applied in the simulations. The results show that the re-entrainment from the fouled surface with similar roughness structure would be harder in comparison to the clean surface. According to the results with the model of Vainshtein *et al.* (1997), the deposition rate would be lower with the fluid with higher viscosity.

The fraction of particles remaining on the rough, calcium carbonate plane surface from the adhered particles is presented as a function of shear rate and time in Figure 59. The results are shown for two particle sizes, 0.387 µm and 2 µm, as a function of shear rate at the instant times of 1 ms, 1 s and 1 min. in addition, for the particle size of 0.387 µm, the results are shown as a function of time with three shear rates 500, 1000 and 4000 1/s. For comparison, the result for the smooth plane is shown. The corresponding results were shown in Figure 15 and 16 for the stainless steel surface with similar roughness.

The particle re-entrainment from the calcium carbonate surface is slower in comparison with the stainless steel surface. This is in line with Bhushan (2013),

who stated that the higher the value for the free surface energy of solid surface, the stronger the bond formed with the mating material. In here, the free surface energy of calcium carbonate is stronger that the surface energy of stainless steel, therefore the bond with the calcite particle is stronger and re-entrainment rate is decreased.

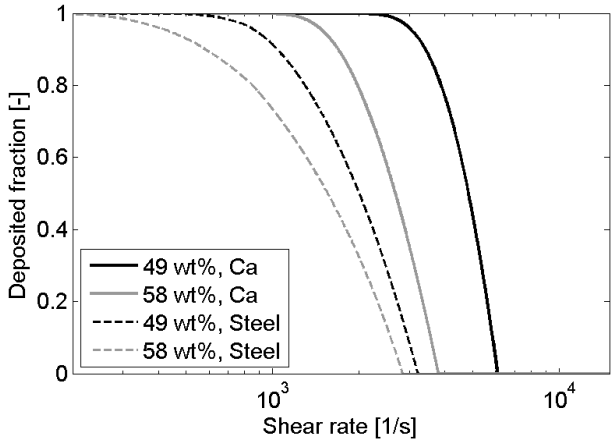

Figure 58. The parameter of source term of deposition rate: equation (7.4.0) calculated at time instant 0.01s for steel and calcium carbonate surfaces calculated with non-Newtonian viscosities modelled for suspension concentrations of 49 wt% and 58 wt%.

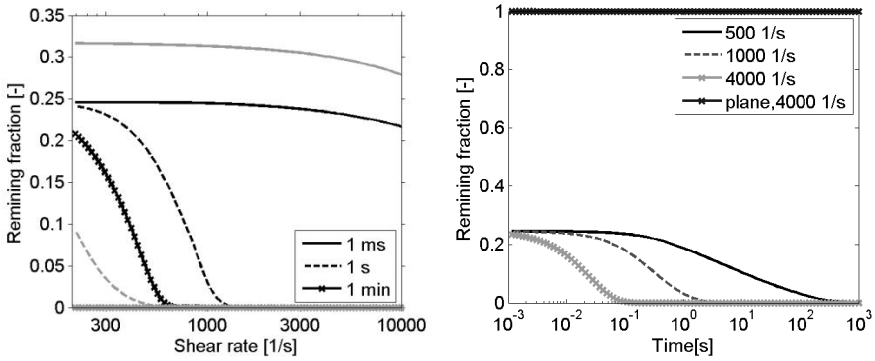

Figure 59. On the left: Remaining fraction on the rough calcium carbonate plane surface for two particle sizes: 0.387 µm (black lines) and 2 µm (grey lines). On the Right: The results are shown for particle size of 0.387 µm.

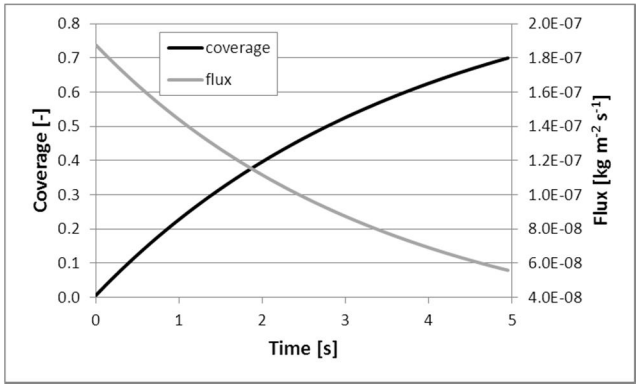

Figure 60. Results on the plane surface calculated with particle size 0.387 µm without re-entrainment: Surface coverage (black lines) and deposition flux to surface (grey lines).

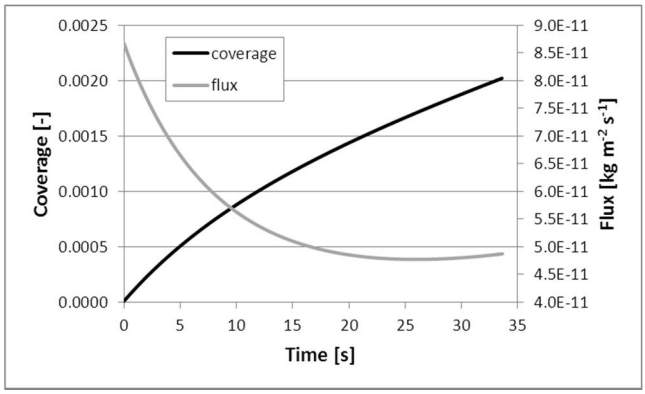

Figure 61. Results on the rough plane surface calculated with particle size 0.387 µm including re-entrainment: Surface coverage (black lines) and deposition flux to surface (grey lines).

The re-entrainment model was tested with the industrial test case. The fouling rate on a surface was calculated considering the fractions of clean and fouled surface starting from a clean, stainless steel surface applying non-Newtonian viscosity. The simulation was computationally highly demanding, and only a short time period was calculated. The results for CFD simulation of particulate fouling on stainless steel surface with and without re-entrainment model are presented in Figures from 60 to 63.

In Figures 60 and 61, the surface coverage due to the fouling and the magnitude of the deposition flux to the surface are presented as a function of time. With the results calculated without the re-entrainment, 70% of the surface is fouled after

5 seconds, but with re-entrainment model included, only 0.5 $^{o}/_{oo}$ of the surface is covered. Therefore, although the fouling rate on the stainless steel is higher than on the fouled layer (see Figure 11), the steel surface remains less fouled for a longer time period due to the easier re-entrainment.

The flux remaining on the stainless steel surface is 0.06 mg/m^2/s at the time instant of five seconds without considering re-entrainment. At the time instant 34.9 s, the remaining flux with re-entrainment is 0.05 µg/m^2/s. The magnitude of flux is increasing due to the increasing deposition on the fouled surface as the coverage of the surface is increasing. In here, the effect of crystallization on the surface coverage is not included. The difference between the results with re-entrainment and without re-entrainment for the remaining flux on the fouled surface was insignificant. In Figures 62 and 63, the total cumulated mass and the cumulated mass on the clean and fouled surfaces are presented as function of time.

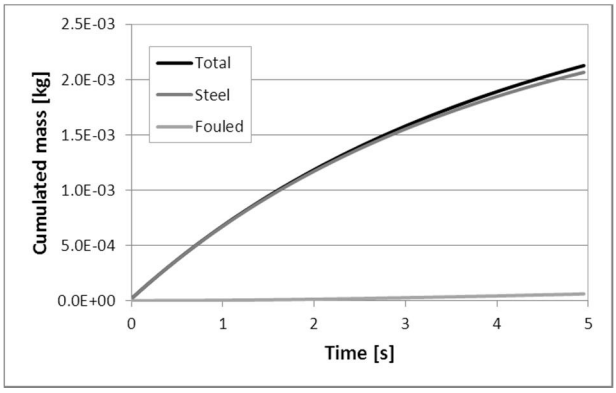

Figure 62. Cumulated mass (kg) on the plane surface calculated with particle size 0.387 µm, re-entrainment not included.

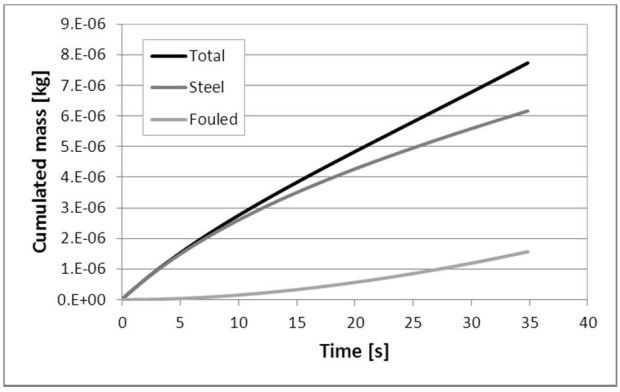

Figure 63. Cumulated mass (kg) on the rough plane surface calculated with particle size 0.387 µm including re-entrainment.

8. Discussion

8.1 Applicability of wall function approach

The postulation of the developed wall function model for particulate fouling was to assume the local equilibrium of the forces affecting on the particle transport. For accurate results, the assumption requires that the particle size is small. The comparison of the simulated results with the results of detailed CFD model showed the assumption to be applicable. With the wall function approach, the use of excessively small computational cells can be avoided.

The wall function approach is valid in the region below $y^+ < 3$. This is due to the model applied for the turbulent viscosity ν_t and approximations done with the temperature profile. The wall function model is applicable with laminar and turbulent flows, because the region $y^+ < 3$ is the region of turbulent inner layer, where the viscous shear forces are dominating. The turbulence is damped out and the flow is close to the laminar flow (White, 1991).

The simulated results were compared with the experimental results. The calculated magnitude of the fouling was close to the experimental results, but the dependency on the heat flux or the mass flow rate of the slurry was not as strong in the simulations as in the experiments with the fouling test apparatus. The model is based only on the parameter values found from literature, experiments or from the process conditions. Taking into account that there are no adjustable parameters, the agreement of simulated and experimental results in Figures 33 and 34 is good. The simulation did not include the effects of the surface roughness on the re-entrainment and adhesion, or the effects of thermophoresis or crystallization fouling.

8.2 On the effect of re-entrainment

The simulated deposition rate dependency on the flow rate was clearly too weak in comparison with the experimental results, as shown in Figure 33. At higher flow velocity, the predicted deposition rate was 80% higher than the averaged experimental result. The discrepancy could be explained with the re-entrainment. From the smooth, plane surface the re-entrainment was shown not to occur in the envi-

ronment of the laboratory experimental tests (see Figure 10) according to the model of Vainshtein *et al.* (1997). However, the re-entrainment has greater importance, if the surface roughness was included (see Figure 15).

The re-entrainment depends on the shear rate at the wall. In order to model the shear rate accurately, LES modelling was applied with the laboratory fouling test geometry. The averaged wall shear stress resulted to be too low to get any visible re-entrainment of the adhered colloidal particles according to the Figures 17 to 19. However, the instant shear rate value shown in Figure 64 is fluctuating in a scale that implies the re-entrainment would be possible. Therefore, the re-entrainment might be locally significant, and can explain at least a part of the difference between the experimental and simulated results for the fouling rate.

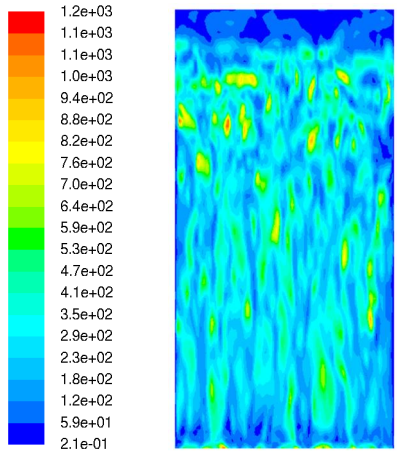

Figure 64. Instant shear rate at the heated wall, 1/s, simulated with LES.

The surface properties have a great impact on the re-entrainment. In addition to the surface roughness, the surface energy is important: the re-entrainment from the surface of higher surface energy is harder than from the surface of lower energy, see Figure 59. Therefore, the fouling on the already fouled surface would be enhanced, as presented with the industrial case, if the free surface energy of the fouled surface is higher than the energy of the clean surface.

The available data for adhesion energies is quite limited, as presented in Section 2.4. It has been pointed out that the wetting experiments do not provide enough information for determining the adhesion energy (Possart and Shanahan, 2011). Therefore, the estimation of the energies might need to be based on the experiments of the studied system. Molecular modelling has been proved to be applicable method for determining the adhesion energies, although the calculations are very time-consuming (Puhakka *et al.,* 2013). The value applied for the surface free energy of the calcium carbonate (in Section 7.4) was calculated by molecular modelling. The value used was not the change in the free surface ener-

gy according to the equation (2.4.4) required in the model of Vainshtein *et al.* (1997), but the free energy needed in formulating the new surface while splitting the material. The value was applied in the modelling in order to have an estimation of the effect of the surface energy on the re-entrainment of the particles. For calcite-calcite contact, the adhesion energy was not determined, but for e.g. calcite-Cr_2O_3, the adhesion energy would be 1.109 J/m^2. Therefore, the value of 0.58 J/m^2 was in a reasonable range.

In estimating the particulate fouling rate, see Figures 61 and 63, the effect of the surface roughness was included in to the modelling of re-entrainment. However, the effect of the surface roughness on the adhesion was not included in these simulations. The surface roughness decreases the interaction energy between the particle and wall surface thus increasing the adhesion of the particles on the surface, as shown in Section 2.6. Therefore, the results for the predicted deposition rate were underestimated.

The model of Vainshtein is capable of taking into account the material properties, e.g. surface energy. This is an advantage in modelling particulate fouling on surfaces of different materials e.g. in order to evaluate the applicability of the material in mitigating the fouling. However, the model is based on assumption of monolayer formation. Therefore, only a thin surface layer of the deposits is considered to interact with the flow. The dependence of re-entrainment of the structure of the deposits and the re-entrainment of clusters are neglected. Most of the existing investigations of particle re-entrainment from the wall by turbulent flow are restricted to a single particle studies. For aerosols, multilayer re-entrainment models are presented e.g. by Friess and Yadigaroglu (2002) and Gradón (2009).

8.3 On the modelling of adhesion with XDLVO

The overestimation of interaction energy predicted by DLVO theory is corrected more often by taking into consideration the surface roughness, heterogeneity of surface charges and comprising the acid-base interactions (XDLVO). In here, the adhesion was modelled with XDLVO theory, in where the surface chemical heterogeneity was taken into account. The results of XDLVO theory near the surface were corrected also with including the effect of the formed electrical double layer on the permeability of the hydrophilic liquid near the solid surface. As seen in Figure 5, the effect on the interaction potential is significant in the separation distances smaller than 10 nm.

The interaction energy between the colloidal particles is very complicated and is influenced by several factors (Liang *et al.,* 2007). The retardation effect on the Hamaker constant might be needed to be considered in electrolyte solutions. The electrolyte solution containing free charges influence on the all electrostatic fields present in the solution. At the larger separation distances (> 5 nm), where the interaction energy between the bodies can still be significant, the polarization of the electric fields due to these charges should be taken into account. Therefore,

the interaction energy due the force of van der Waals, and thus the fouling rate, might be over predicted in here.

The surface roughness affects the particle adherence on the surface: the short range interaction energies predicted by XDLVO between the surfaces are significantly suppressed, and thus the deposition of the particles is easier. The method of modified Derjaguin approach by Huang *et al.* (2010) was applied in investigating the effect of the surface roughness on the deposition rate. The method is accurate when the radius of the particle is large in comparison to the radius of the asperities. With large asperities, the method gives indicative results for the interaction energy.

In studying the effect of impurities on calcite particulate fouling, the similar phenomena were found in experimental tests and in modelling: In experiments, the particulate fouling was not occurring without additional salt in the test fluid. According to the predictions of the XDLVO model, a pure calcite particle is not adhering on a pure calcite surface. Therefore, the fouling of calcite particles can be thought to occur due to the impurities accumulated from the process fluid into the scales. In simulations, the surface chemical heterogeneity has been considered in the calculations according to Section 2.5. The simulated results were in fairly good agreement with the experimental results, although the amount of impurities (magnesium) in the fouling layer was estimated from other experiments.

The predicted results are strongly dependent on the amount of impurities in the scales. In here, only magnesium and silicates were taken into account in the model for industrial test heat exchanger. In the scale analysis, small amounts of aluminium, iron and potassium were also found (Riihimäki *et al.*, 2005). The effect of these materials on the mass deposition rate was not considered in the model.

The method applied for modelling the surface energy is based on the work of van Oss *et al.* (2006). However, in literature there are presented several other methods for determination of surface tension energies from wetting experiments, the best known versions are the model of Owens and Wendt and the model of Wu (Possart and Shanahan, 2011). These three models are widely applied in literature, although the accuracy all of the models is quite questionable due to the approximations made in the evaluations.

8.4 On the effect of particle size

The uncertainties in the evaluation of the particle size distributions and particle sizes cause considerable effects on the evaluation of deposition rates, as presented in Section 6.3. The particle size effects on the deposition rate in several ways. The re-entrainment is greater among the micron sized particles. In addition, with the micron sized particles, the adhesion on a smooth plate would be lower. According to XDLVO theory, the deposition rate is due to the small particles, as seen in Figure 8. For larger particles, the adhesion on the surface with small asperities would be easier, and the deposition rate would be greater. In that case, also the

re-entrainment is taking place easier even with lower values of the shear rate, and the total deposition rate would be lower. This is illustrated in Figures from 17 to 19.

Including the particle size distribution in the simulation would be computationally demanding. Therefore only the estimated effective particle size was applied. The tests with the particle size distribution showed that with the effective particle size, the overall deposition rate would be obtained in a fairly good agreement. However, the determination of the effective particle size is complicated due to the deposition rate dependency on a particle size, as seen in Figure 8. Therefore, in determining the effective particle size, the simulation with several particle sizes was needed in order to account the effects due to the dependency of particle size including also the hydrodynamic effects.

8.5 On the effect of thermophoresis

With several tested models of thermophoresis for charged spherical colloidal particles, the effect on the deposition rate seemed to be quite insignificant, of the order of 1%, see Figure 40. In comparison with the experimental results, the dependency of simulated results on the heat flux (Figure 34) was in agreement with the results for the particle concentration of 4.9%. Therefore, it might be possible that the magnitude of the thermophoresis is insignificant. However, if all the experimental results in Figure 34 are considered, the dependency on the heat flux is stronger, but in the opposite direction as assumed with the thermophoresis. Thermophoresis has been considered to prevent fouling in the temperatures of the test case as discussed in Section 2.1.3.

With the tested model of Würger (2009), the effect on the deposition rate was significant. The predicted deposition rate with the model of Würger (2009) was only 68% of the deposition rate without thermophoresis. Based on the Figure 2, with the model of Dhont *et al.* (2007) fouling would not occur almost at all.

From the final model, the effect of thermophoresis was excluded due to the large range of predicted values with the models presented in literature. For validating the models, there was not sufficiently experimental data available.

8.6 Evaluation of crystallization

The deposition rate due to crystallization was not included in the model. With the applied test fluid, the supersaturation ratio of $CaCO_3$ is low and therefore, the significance of the crystallization would be probably low, as discussed in Ojaniemi *et al.* (2012). In order to produce measurable crystallization fouling rate in the experiments in comparable conditions, the $CaCO_3$ concentration has been an order of magnitude greater (Pääkkönen *et al.*, 2010). At low supersaturation ratio, however, the attached colloidal particles may act as nuclei for crystallization, thus increasing the crystallization rate. The enhancing effect of the particles on the crystallization has noted to be stronger at the low fluid flow velocities (Andritsos and Karabelas, 2003).

As shown in Figure 33, at lower flow velocity, the predicted deposition rate was 24% lower than the averaged experimental result. That might indicate the need for including of the crystallization fouling. In addition, the dependency on the heat flux (Figure 34) might be explained with the crystallization, because the calcium carbonate forms inverse-solubility salts. Therefore, with increasing temperature the overall deposition rate would increase due to the crystallization.

In Figure 65, the sketch of the combination of crystallized and particulate fouling is presented. Crystallization starts by nucleating on the clean surface, and the surface area is enlarged by the nuclides. Particulate fouling can take place both on clean and fouled surface, but depending on the surface energies, the fouling rate is different. For modelling the particulate fouling rate on the clean surface, the coverage of the fouled surface has to be known.

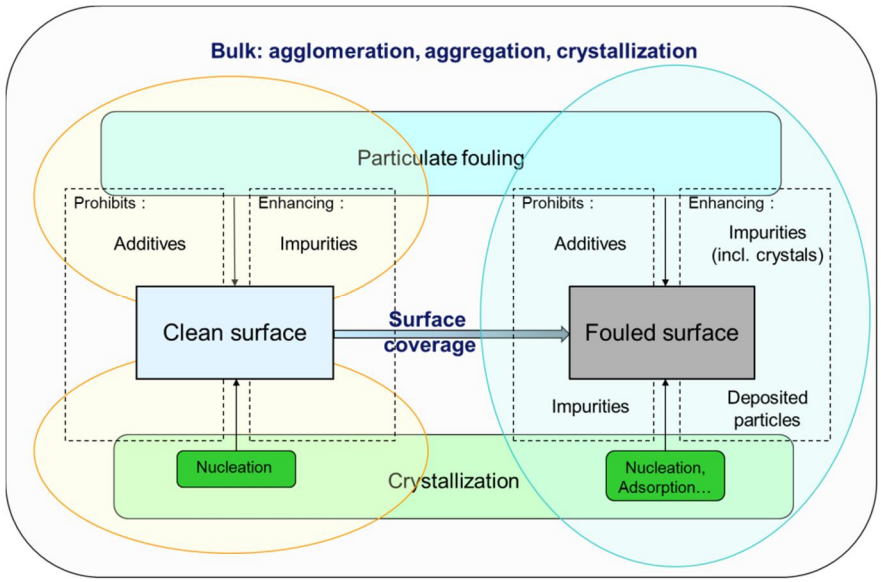

Figure 65. Sketch of the combination of particulate and crystallization fouling.

The additives, e.g. stability agents, keep the particles non-fouling. It is commonly known, that the stable colloidal suspensions form only monolayer fouling (Yiantsios and Karabelas, 2003). Impurities in the fluid resulting from the raw materials might break up the colloidal stability, and the particles start to deposit on the surfaces. The impurities affect also on the crystallization growth, e.g. magnesium prohibits the calcium carbonate crystallization growth (Nishino *et al.*, 2009; Lopez *et al.*, 2009; Astilleros *et al.*, 2010).

The precipitation fouling and particulate fouling influences each other in combined fouling, as discussed also by Andritsos and Karabelas (2003) and Zhang, F. *et al.* (2013). The particles have been generally assumed to induce crystallization

fouling due to the enlarged surface area for nucleates and crystal growth. On the other hand, the crystallization will change the roughness of the surface, and the particulate fouling is enhanced.

In high solid content slurries, the enlarged surface area due to the particles in bulk might reduce the crystallization on the wall surfaces due to the larger crystallization rate on the bulk fluid particles. The experiments have shown the seeded solutions to catalyse the $CaCO_3$ crystallization on the surfaces of calcite seeds (Lin and Singer, 2005).

The combined fouling caused by crystallization and particle attachment is a quite complex phenomenon due to the unknown details of the process. In addition to crystallization, agglomeration (due to the chemical forces especially in supersaturated fluids) and aggregation (due to the XDLVO forces) have been excluded from the model.

8.7 Effects due to the high particle concentration

In simulating the industrial test heat exchanger, the slurry is significantly more concentrated than in the experiments with the laboratory scale heat exchanger. Therefore the viscosity of the fluid is also higher and the fluid is non-Newtonian. With simulations of the industrial test heat exchanger presented in Ojaniemi *et al.* (2012), the calculations were done with Newtonian fluid with the viscosity derived from the experimental measures of the viscosity of the test fluid. The applied viscosity for the fluid was about 56 times water viscosity at the temperature 298 K. The simulations were carried out with the grid where the plates of the heat exchanger were separated with 0.25 mm. The simulated results for the fouling rate, 0.8 g/day, were significantly lower than the experimental results, 1.9 g/day. With the non-Newtonian model for the viscosity, the fouling rate resulted to be higher, 2.7 g/day. Therefore, the realistic modelling of fluid viscosity is essential in order to model fouling.

As noted in Section 7.1, the standard approaches for near wall turbulence modelling do not take into account the rheology of the suspension. For modelling turbulent flow of non-Newtonian suspension, the model of standard k-ε with enhanced wall treatment (EWT) was applied. The calculated flow field included also the viscous sub layer, and therefore, the rheology is taken into account in the near wall region in the velocity profile. The effect of the non-Newtonian viscosity on the flow field, and therefore on the fouling rate should be investigated further in the near wall region.

XDLVO theory has been developed for single particle and surface. The multiparticle effect on the interaction energy between the particles is significant in the concentrated colloidal dispersion. According to Liang *et al.* (2007), the effect can be considered with a cell model expressed by Bowen and Jenner (1995) applying the volume fraction approach proposed by Reiner and Radke (1991). In the method, the colloidal dispersion is divided into spherical cells with one particle and concentric spherical volume of electrolyte solution. With the approach, the force

between two particles including the multiparticle effect can be calculated. However, the method requires numerical solution of non-linear Poisson-Bolzman equation (PBE) at the surface of the concentric spherical volume of electrolyte solution. Therefore, the method might be computationally demanding in order to combine with CFD simulations.

9. Summary and conclusion

9.1 Summary

The fouling of heat exchangers due to colloidal particles in suspension of high solid concentration was examined and the CFD model for fouling was developed. Particulate fouling is generally considered as a serial process of the transport of the particles into the vicinity of the wall and the adherence on the surface. Once the particle is adhered on the surface, it may re-entrain from the surface due to the hydrodynamic forces affecting on the particle.

At first, the magnitude and interaction region of the forces affecting on the colloidal particles transport in to the heated wall were studied. For that purpose, the CFD fouling model was first implemented as a detailed version, which included all the relevant near-wall forces affecting the particles and requiring an extremely fine mesh near the fouling surface. Generally accepted models were applied in modeling the forces affecting on particle transport. The results with the model were compared with the experimental results by performing two-dimensional simulations. On the basis of the detailed model the forces considered in transport of the colloidal particles were drag and diffusion forces. The lift and turbophoresis were found to be insignificant in the case of submicron sized particles in liquid.

Based on the experience from the detailed simulation results, a wall function approach for the CFD modelling of particulate fouling was developed. Therefore, the wall function approach comprised the drag and diffusion forces as most relevant forces affecting on the particulate transport. The wall function approach allows much larger near-wall cell, thus decreasing the computational effort dramatically. The parameters applied in the developed wall function approach are based on the studied case and derived from physical properties.

For including the effect of thermophoresis, the wall function approach was further developed to include also the temperature profile. Several models presented in literature for the Soret coefficient of charged, spherical colloid in liquid were studied. The values predicted by the models had a wide range, and the models could not be validated with the experiments carried out. Therefore, the thermophoresis was neglected in the present wall function approach. However, the method for including the model into the approach is available.

The adhesion of the particles on the surface was modeled with masstransfer coefficient based on the model proposed by Spielman and Friedlander (1973). The model incorporates the interaction energy between the approaching surfaces into the calculation of particle flux at the wall. The interaction energy is calculated based on XDLVO theory. In calculating the masstransfer coefficient, the reduction of a particle movement in the close vicinity of the surface was included with the model of Elimelech *et al.* (1995).

For correcting the predicted interaction values in the near wall region with the XDLVO theory, the models of Podgornic *et al.* (1987) and Teschke *et al.* (2001) were applied. The XDLVO theory was modified by including the effect of the electric field due to the double layer formed near the surface on the polarization of the medium, i.e., water. The water permittivity near the surface is changed that effects on the double layer thickness. The values predicted by XDLVO theory are more often corrected with considering the surface roughness. The effect of surface roughness was studied with the models presented in literature.

The sensitivity of XDLVO theory on the process parameters was examined. The results with the theory were found to be greatly influenced by the zeta potential of the surfaces, particle size and ion strength of the suspension. The particle size was found to be critical for the particulate fouling. The submicron sized particles were significantly contributing to the fouling rate, whereas the effect of the larger particles was negligible.

The surface chemical heterogeneity has a great impact on the fouling rate. The particulate fouling of $CaCO_3$ seemed to occur on the surface already covered with a $CaCO_3$ layer only due to the impurities of the slurry according to the XDLVO theory. The precipitation of dissolved ions other than the particulate material may alter the surface energies and thus promote the particulate fouling. The results for fouling rate were very dependent on the amount of impurities. In modelling the particulate adhesion, the chemical heterogeneity of the surface was based on experimental data from the fouling layers found in industry.

The numerical models were tested for an experimental setup of the colloidal calcite particle fouling on the heated stainless steel surface (AISI 316L). Several mass flows and heat flows, and two mass fractions of particles were applied. The applicability of the fouling model for comprising the effect of process conditions was examined. The calculated magnitude of the fouling rate was close to the experimental results, but the dependency on the heat flux or the mass flow rate of the slurry in the simulations was not as strong as in the experiments. The crystallization, thermophoresis or re-entrainment were not included in the simulation.

In addition, in comparison to the measured values, the predicted surface temperature was lower. The modelled fouling process is dependent on the temperature and the simulated lower deposition rate is a result of the lower wall temperature in the simulation. The heat transfer is controlled by turbulent diffusion, except very close to the wall. It is possible that the modelling of turbulence is less accurate for the smaller mass flow rates, i.e., smaller Reynolds number. In order to have a reliable comparison, there should have been more experimental results.

As a practical case, the wall function approach was applied in the modelling of industrial corrugated heat exchanger equipment, where the content of particles used was 0.49 or 0.58 kg/kg_{fluid}. With the high solid content slurry, the viscosity behavior is non-Newtonian. The model for the non-Newtonian viscosity was derived from the experiments and implemented into CFD code. It was shown, that according to the model, the higher non-Newtonian viscosity of the flow decreases the particulate fouling rate due to lower mobility of the particles. However, the effect of the viscosity on fouling in the near wall region should be further studied.

The shear stress is a major effect in particle re-entrainment implying that the realistic modelling of turbulence is essential. Therefore, the CFD simulations of the laboratory test heat exchanger were performed with Large Eddy Simulation (LES) in 3D and the results were compared those calculated using the standard k-ε model with Enhanced Wall Treatment (EWT) in 3D. The time averaged values for shear rate were too small for promoting the particulate re-entrainment. However, the temporal values of shear rate might be able to locally re-entrain the particles.

The effect of surface roughness and surface energy on the particle re-entrainment was studied with the model of Vainshtein *et al.* (1997). The model was modified to be applicable for CFD simulation. The CFD simulation was carried out for the practical size heat exchanger in order to evaluate the effect of the surface energy on the fouling rate. The higher the adhesion energy in the contact of the mating surfaces, the harder the re-entrainment of the particle is. Therefore, the already fouled surface with higher surface energy tends to be fouling further due to the lower re-entrainment rate, although the deposition rate according to the XDLVO theory on the fouled surface was lower.

9.2 Conclusions

A wall function approach for the CFD modelling of particulate fouling of a heat exchanger was developed. Particulate fouling models applicable in high solid content in practical sized heat exchangers has not been presented so far in a literature. Based on the multiphase CFD method, i.e. the solution is modelled as a mixture of the liquid and solid phases, the approach is applicable in practical size heat exchangers with high solid content. In comparison with the detailed fouling model with extremely fine near-wall mesh, the computational effort needed was significantly lower with the wall function approach, which is applicable up to y^+ = 3.

The results were in fairly good agreement with the experiments, considering that all the parameters applied in the developed wall function approach are based on the studied case and derived from physical properties; separate adjustable model parameters were not added. The parameters applied were process specific boundary conditions. The values applied in the modelling of the surface free energies in determining the adhesion of the particles on the surface were determined experimentally or by the molecular modelling, or found from literature.

The combined CFD model of the wall function approach and the re-entrainment is novel method for simulation of particulate fouling process considering the sur-

face free energies of materials. The surface heterogeneity and the impurities in the solution have a great impact on the fouling rate. The precipitation of dissolved ions other than the particulate material may alter the surface energies and thus promote the particulate fouling. The re-entrainment of the particles is proportional to the adhesion energy of the contact of particle and surface. The applied re-entrainment model of Vainshtein *et al.* (1997) takes into account the adhesion energy. The study shows that the particulate fouling is controlled by surface energies of the materials.

The geometry and materials applied are important in designing the heat exchangers with less fouling properties. For that purpose, the presented model can be applied for an evaluation of the colloidal particulate fouling rate. In general, the developed wall function approach can be adapted into other applications of particles and surfaces.

References

Adamczyk, Z., Werónski, P., 1999, Application of the DLVO theory for particle deposition problems. Adv. Colloid Interface Sci., 83, 137-226.

Adomeit, P., Renz, U., 1996, Deposition of fine particles from a turbulent liquid flow: Experiments and numerical predictions. Chem. Eng. Sci. 51, 3491-3503.

Andritsos, N., Karabelas, A.J., 2003, Calcium carbonate scaling in a plate heat exchanger in the presence of particles. Int. J. Heat Mass Transfer 46, 4613-4627.

Astilleros, J.M., Fernández-Díaz, L., Putinis, A., 2010, The role of magnesium in the growth of calsite: An AFM study. Chemical Geology 271, 52-58.

Bacchin, P., Aimar, P., Field, R.W., 2006, Critical and sustainable fluxes: Theory, experiments and applications. J. Membr. Sci. 281, 42-69.

Bendersky, M., Davis, J. M., 2011, DLVO interaction of colloidal particles with topographically and chemically heterogenous surfaces. J. Colloid Interface Sci. 353, 87-97.

Bhushan, B., 2013, Tribology in Practice Series: Principles and Applications to Tribology, 2nd ed., Wiley, 308 p.

Biasi, L., de los Reyers, A., Reeks, M.W., de Santi, G.F., 2001, Use of a simple model for the interpretatation of experimental data on particle resuspension in turbulent flows. J. Aerosol Sci. 32, 1175-1200.

Boulangé-Petermann, L., Doren, A., Baroux, B., Bellon-Fontaine, M-N., 1995, Zeta potential measurements on passive metals. J. Colloid Interface Sci. 171, 179-186.

Bowen, W.R., Jenner, F., 1995, Dynamic ultrafiltration model for charged colloidal dispersions: a Wigner – Seitz cell approach. Chem. Eng. Sci. 50, 1707.

Bower, M.J.D., Bank, T.L., Giese, R.F., Van Oss, C.J., 2010, Nanoscale forces of interaction between glass in aqueous and non-aqueous media: A theoretical and empirical study. Colloids and Surfaces A: Physicochem. Eng. Aspects 362, 90–96.

Burdick, G.M., Berman, N.S., Beaudoin, S.P., 2005, Hydrodynamic particle removal from surfaces. Thin Solid Films 488, 116-123.

Chung-Cherng, L., 2013, Elasticity of calcite: thermal evolution. Phys. Chem. Minerals 40, 157–166.

Crowe, C., Sommerfield, M., Tsuji, Y., 1998, Multiphase flows with droplets and particles, CRC Press, Boca Rato, USA.

Derjaguin, B.V., Landau, L.D., 1941, Theory of the stability of strongly charged lyophobic sols and of the adhesion of strongly charged particles in solutions of electrolytes. Acta Physico Chemica URSS 14: 633.

Dhont, J. K. G., Wiegand, S., Duhr, S., Braun, D., 2007, Thermodiffusion of charged colloids: Single-particle diffusion. Langmuir 23, 1674-1683.

Elimelech, M., O'Melia, C. R., 1990, Effect of Particle Size on Collision Efficiency in the Deposition of Brownian Particles with Electrostatic Energy Barriers. Langmuir 6, 1153-1163.

Elimelech, M., Greory, J., Jia, X., Williams, R.A., 1995, Particle Deposition and Aggregation – Measurement, Modelling and Simulation, Elsevier.

Epstein, N., 1997, Elements of Particle Deposition onto Porous Solid Surfaces Parallel to Suspension Flows. Experimental Thermal and Fluid Science 14, 323-334.

Eskin, D., Ratulowski, J., Akbarzadeh, K., 2011, Modeling of particle deposition in a vertical turbulent pipe flow at a reduced probability of particle sticking to the wall. Chem. Eng. Sci. 66, 4561-4572.

Fluent, 2009, Ansys Fluent Users' guide – Release 12.1, Ansys Inc.

Fluent, 2011, Ansys Fluent Users' guide – Release 14.0, Ansys Inc.

Franks, G.V., 2002, Zeta potentials and Yield Stresses of Silica Suspensions in Concentrated Monovalent Electrolytes: Isoelectric Point Shift and Additional Attraction. J. Colloid Interface Sci. 249, 44-51.

Friess, H., Yadigaroglu, G., 2002, Modelling of the resuspension of particle clusters from multilayer aerosol deposits with variable porosity. J. Aerosol Sci. 33, 883-906.

Gidaspow, D., Bezburuah, R., Ding, J., 1992, Hydrodynamics of Circulating Fluidized Beds, Kinetic Theory Approach, In Fluidization VII, Proceedings of the 7th Engineering Foundation Conference on Fluidization, 75–82.

Gence, N., Nurgul, O., 2006, pH dependence of electrokinetic behaviour of dolomite and magnesite in aqueous electrolyte solutions. App. Surf. Sci. 252, 8057-8061.

Goldman, A.G., Cox, R.G., Brenner, H., 1967, Slow viscous motion of a sphere parallel to a plane wall. Chem. Eng. Sci. 22, 637-653.

Gradón, L., 2009, Resuspension of particles from surfaces: Technological, environmental and pharmaceutical aspects. Adv. Pow. Tech. 20, 17-28.

Grandgeorge, S., Jallut, C., Thonon, B., 1998, Particulate fouling of corrucated plate heat exchangers: Global kinetic and equilibrium studies. Chem. Eng. Sci. 53, 3051-3071.

Guha, A., 1997, A Unified Eulerian theory of turbulent deposition to smooth and rough surfaces. J. Aerosol Sci. 28, 1517-1537.

Guha, A., 2008, A generalized mass transfer law unifying various particle transport mechanisms in dilute dispersions. Heat Mass Transfer 44, 1289-1303.

Handbook of Chemistry and Physics, 1998, CRC Press, Boca, Raton.

Henry, C., Minier, J-P., Lefevre, G., 2012, Towards a description of particulate fouling: From single particle deposition to clogging. Adv. Colloid Interface Sci. 185-186, 34-76.

Henry, C., Minier, J-P., Lefevre, G., Hurisse, O., 2011, Numerical study on the deposition rate of hematite particle on polypropylene walls: Role of surface roughness. Langmuir 27, 4603-4612.

Hoek, E.M.V., Agarwal, G.K., 2006, Extended DLVO interactions between spherical particles and rough surfaces. J. Colloid Interface Sci. 298, 50-58.

Holland, F.A., Bragg, R., 1995, Fluid flow for chemical and process engineers, 2nd ed., Jordan Hill, GBR, Butterworth-Heinemann

Huang, X., Bhattacharjee, S., Hoeh, E. M. V., 2010, Is surface roughness a “scapegoat” or a primary factor when defining particle-substrate interactions?. Langmuir 26, 2528–2537.

Johansen, S.T., 1991, The deposition of particles on vertical walls. Int. J. Multiphase Flow 17, 355-376.

Johnsen, S.G., Johansen, S.T., 2010, Deposition modeling from multi-phase dispersed flow – A boundary layer wall function approach, Proceedings of 8th International Conference on Heat Exchanger Fouling and Cleaning VIII – 2009 (Peer-reviewed), eds. H. Müller-Steinhagen, M. R. Malayeri, and A. P. Watkinson, EUROTHERM Seminar No. 86, 2009, pp. 237–244.

Karabelas, A.J., 2002, Calcium carbonate scaling in a plate heat exchanger in the presence of particles. Int. J. Therm. Sci. 41, 682-692.

Kell, G.S., 1975, Density, thermal expansivity, and compressibility of liquid water from 0˚ to 150˚C: Correlations and tables for atmospheric pressure and saturation reviewed and expressed on 1968 temperature scale. J. Chem. Eng. Data Vol. 20, pp. 97-105.

Kerner, J., 2011, Compact, high-efficiency heat exchangers: Understanding fouling. Chem. Eng. Vol. 118, pp. 35-41.

Li, W., Li, H-x., Li, G-q., Yao, S-c., 2013, Numerical and experimental analysis of composite fouling in corrugated plate. Int. J. Heat and Mass Transfer, 63, 351-360.

Liang, Y., Hilal, N., Langston, P., Starov, V., 2007, Interaction forces between colloidal particles in liquid: Theory and experiment. Adv. Colloid Interface Sci. 134-135, 151-166.

Lin, Y-P., Singer, P. C., 2005, Effects of seed material and solution composition on calcite precipitation. Geochimica et Cosmochimica Acta 69, 4495-4504.

Lopez, O., Zuddas, P., Faivre, D., 2009, The influence of temperature and seawater composition on calcite crystal growth mechanisms and kinetics: Implications for Mg incorporation in calcite lattice. Geochimica et Cosmochimica Acta 73, 337-347.

Lun, C. K. K., Savage, S. B., Jeffrey, D. J., Chepurniy, N., 1984, Kinetic Theories for Granular Flow: Inelastic Particles in Couette Flow and Slightly Inelastic Particles in a General Flow Field. J. Fluid Mech. 140, 223–256.

Maniero, R., Canu, P., 2006, A model of fine particles deposition on smooth surfaces: I – Theoretical basis and model development. Chem. Eng. Sci. 61, 7626-7635.

MATLAB and Statistics Toolbox Release 2012, The MathWorks, Inc., Natick, Massachusetts, United States.

Martines, E., Csaderova, L., Morgan, H., Curtis, A.S.G., Riehle, M.O., 2008, DLVO interaction energy between a sphere and a nano-patterned plate. Colloids and Surfaces A: Physicochem. Eng. Aspects 318, 45-52.

Menter, F.R., 2011, Best Practice: Scale-Resolving Simulations in ANSYS CFD, ANSYS Germany GmbH.

Müller-Stainhagen, H., 2011, Heat Transfer Fouling: 50 Years after the Kern and Seaton Model. Heat Transfer Eng. 32, 1–13.

Müller-Stainhagen, H., Reif, F., Epstein, N., Watkinson, A.P., 1988, Influence of operating conditions on particulate fouling. Can. J. Chem. Eng. 66, 42-50.

Nicoud, F., Ducros, F., 1999, Subgrid-scale stress modelling based on the square of the velocity gradient tensor flow. Turbulence and combustion 62 (3), 183-200.

Nishino, Y., Oaki, Y., Imai, H., 2009, Magnesium-mediated nanocrystalline mosaics of calcite. Crystal growth and design 9, 223-226.

Ogawa, S., Umemura, A., Oshima N., 1980, On the equation of fully fluidized granular materials. J. Appl. Math. Phys., 31:483.

Ojaniemi, U., Pättikangas, T., Riihimäki, M., Manninen, M., 2008, CFD model for particulate fouling – modelling particle adhesion on surface with XDLVO theory, in: S.T. Johansen (Ed.), 6th Int. Conf. on CFD in Oil & Gas, Metallurgical and Process Industries, SINTEF/NTNU, Trondheim, Norway.

Ojaniemi, U., Riihimäki, M., Manninen, M., Pättikangas, T., 2012, Wall function model for particulate fouling applying XDLVO theory. Chem. Eng. Sci. Vol. 84, 57-69.

Ojaniemi, U., Manninen, M., Pättikangas, T., Riihimäki, M., 2013, Modelling turbulence and thermophoresis in plate heat exchanger with high solid content, Proceedings of 10th International Conference on Heat Exchanger Fouling and Cleaning X – 2013 (Peer-reviewed), Eds. H. Müller-Steinhagen, M. R. Malayeri, and A. P. Watkinson.

Oliveira, R., 1997, Understanding Adhesion: A Means for preventing fouling. Experimental Thermal and Fluid Science 14, 316-322.

Parola, A., Piazza, R., 2004, Particle thermophoresis in liquids. Eur. Phys. J. E Vol. 15, 255-263.

Perry, J.H., 1970, Chemical Engineer´s Handbook, McGraw-Hill, New York.

Podgornik, R., Cevc, G., Zeks, B., 1987, Solvent structure effects in the macroscopic theory of van der Waals forces. J. Chem. Phys. (87) 5957.

Possart, W., Shanahan, M. E. R., 2011, Thermodynamics of adhesion. Eds. da Silva, L. F. M., Öchsner, A., Adams, R. D., Handbook of adhesion technology, Springer-Verlag, Berlin Heidelberg.

Probstein, R. F., 2013, Physicochemical Hydrodynamics: An Introduction, ed. Brenner, H., Butterworths series in chemical engineering, Butterworth-Heinemann, e-book, ISBN 9781483162225, loaded 22.10.2013.

Puhakka, E., Ojaniemi, U., Pättikangas, T., Manninen, M., Pääkkönen, T.M., Riihimäki, M., Lecoq, E., Duday, D., Guillot, J., 2013, EFFIMAT, Improved energy efficiency by modifying the surface properties of materials, Final report 2013, Research Report VTT-R-07328-13, Espoo, Finland.

Putnam, S.A., Cahill, D.G., Wong, G.C.L., 2007, Temperature dependence of thermodiffusion in aqueous suspensions of charged nanoparticles. Langmuir 23, 9221-9228.

Pääkkönen, T.M., Riihimäki, M., Puhakka, E., Muurinen, E., Simonson, C.J., Keiski, R.L., 2010, Crystallization fouling of CaCO3 – Effect of bulk precipitation on mass deposition on the heat transfer surface, Proceedings of 8th International Conference on Heat Exchanger Fouling and Cleaning VIII – 2009 (Peer-reviewed), Eds. H. Müller-Steinhagen, M. R. Malayeri, and A. P. Watkinson, EUROTHERM Seminar No. 86, 2009, pp. 209–216.

Quan, Z., Chen, Y., Ma, C., 2008, Experimental study of fouling on heat transfer surface during forced convective heat transfer. Chinese J. Chem. Eng. 16 (4) 535-540.

Reeks, M.W., 1983, The transport of discrete particles in inhomogeneous turbulence. J. Aerosol Sci. 14, 729-739.

Reeks, M.W., Reed, J., Hall, D., 1988, On the resuspension of small particles by a turbulent flow. J. Phys. D: Appl. Phys. 21, 574-589.

Reeks, M.W., Hall, D., 2001, Kinetic models for particle re-suspension in turbulent flows: theory and measurement. J. Aerosol Sci. 32, 1-31.

Reiner, E.S., Radke, C.J., 1991, Electrostatic interactions in colloidal suspensions – test of pairwise additivity. AIChE J 37, 805-24.

Riihimäki, M., 2013, measurement results, personal information.

Riihimäki, M., Ojaniemi, U., Pättikangas, T.J.H., Pääkkönen, T.M., Manninen, M., Puhakka, E., Muurinen, E., Simonson, C.J., Keiski, R.L., 2010, Fouling in high solid content suspension – Effect of nucleating air and background electrolyte, Proceedings of 8th International Conference on Heat Exchanger Fouling and Cleaning VIII – 2009 (Peer-reviewed), Eds. H. Müller-Steinhagen, M. R. Malayeri, and A. P. Watkinson, EUROTHERM Seminar No. 86, 2009, pp. 192–199.

Riihimäki, M., Muurinen, E.I., Keiski, R.L., 2005, Silicate Fouling in Evaporators – Thermodynamic Equilibrium Modeling of Aqueous Electrolytes, in: 7th World Congress of Chemical Engineering, Glasgow, Scotland.

Santos, O., Nylander, T., Roshmaninho, R., Rizzo, G., Yiantsios, S., Andritsos, N., Karabelas, A., Müller-Steinhagen, H., Melo, L., Boulangé-Petermann, L., Gabet, C., Braem, A., Trägårdh, C., Paulsson, M., 2004, Modified stainless steel surfaces targeted to reduce fouling – surface characterization. J. Food Eng. (64) 63–79.

Semenov, S. N., Schimpf, M. E., 2011, Thermodynamics of mass transport in diluted suspensions of charged particles in non-isothermal liquid electrolytes. C.R.Mecanique Vol. 339, pp. 280-286.

Spielman, L.A., Friedlander, S.K., 1973, Role of electrical double layer in particle deposition by convective diffusion. J. Colloid Interface Sci. Vol. 46, pp. 22-31.

Stempniewicz, M. M., Komen, E. M. J., 2010, Comparison of several re-suspension models against measured data. Nuclear Eng. and Design, 240, 1657-1670.

Suresh, L., Walz, J. Y., 1996, Effect of surface roughness on the interaction energy between a colloidal sphere and a flat plate. J. Colloid Interface Sci. 183, 199-213.

Teschke, O., Ceotto, G., Souza, E.F., 2001, Interfacial water dielectric-permittivity-profile measurements using atomic force microscopy. Physical Review E. 64, 011605-(1–10).

Vainshtein, P., Ziskind, G., Fichman, M., Gutfinger, C., 1997, Kinetic Model of Particle Re-suspension By Drag Force. Phys. Rew. Lett., 78, 551-554.

Van Oss, C.J., 2006, Interfacial forces in Aqueous media, 2nd ed., Marcel Dekker, New York.

Verwey, E. J. W., Overbeek, J. Th. G., 1948, Theory of the stability of lyophobic colloid, Elsevier, Amsterdam.

Warzynski, P., 2000, Coupling of hydrodynamic and electric interactions in adsorption of colloidal particles. Adv. Colloid Interface Sci. 84, 47-142.

Wen, C.-Y., Yu, Y. H., 1966, Mechanics of Fluidization. Chem. Eng. Prog. Symp. Series 6, 100–111.

White, F. M., 1991, Viscous fluid flow, 2nd ed., McGraw-Hill, Inc., Singapore.

Wu, W., Giese Jr, R.F., Van Oss, C.J., 1996, Change in surface properties of solids caused by grinding. Pow. Tech. 89, 129-132.

Würger, A., 2009, Temperature dependence of the Soret motion in colloids. Langmuir 25, 6696-6701.

Yang, Z., Shih, T. H., 1993, New time scale based k-ε model for near-wall turbulence. AIAA Journal, 31 (7), 1191-1198.

Yiantsios, S. G., Karabelas, A. J., 2003, Deposition of micron-sized particles on flat surfaces: effects of hydrodynamic and physicochemical conditions on particle attachment efficiency, Chem. Eng. Sci. 58, 3105-3113.

Ziskind, G., Fichman, M., Gutfinger, C., 1995, Resuspension of particulates from surfaces to turbulent flows – Review and analysis. J. Aerosol Sci. 26, 613-644.

Ziskind, G., Fichman, M., Gutfinger, C., 1998, Effects of shear on particle motion near a surface – Application to resuspension. J. Aerosol Sci. 29, 323-338.

Zettler, H.U., Wei, M., Zhao, Q., Müller-Steinhagen, H., 2005, Influence of Surface Properties and Characteristics on Fouling in Plate Heat Exchangers. Heat Transfer Engineering 26, 3-17.

Zhang, F., Reeks, M., Kissane, M., 2013, Particle re-suspension in turbulent boundary layers and the influence on non-Gaussian removal forces. J. Aerosol Sci. 58, 103-128.

Zhang, G-m., Li, G-q., Li, W., Zhang, Z., Leng, X-l., Tian, M-c., 2013, Particulate fouling and composite fouling assessment in corrugated plate. Int. J. Heat and Mass Transfer 60, 263-273.

Series title and number

VTT Science 88

Title	**Modelling particulate fouling in heat exchanger with high solid content liquid suspension**
Author(s)	Ulla Ojaniemi
Abstract	A computational fluid dynamics (CFD) model for particulate fouling in high solid content heat exchangers has been developed. The model is applicable in practical industrial heat exchangers. Particulate fouling is generally considered as a serial process of transport of particles into the vicinity of the wall, adherence on the surface and possible re-entrainment from the surface. The CFD fouling model was first implemented as a detailed two fluid Eulerian model, which included all the relevant near-wall forces affecting on the colloidal particles and requiring an extremely fine mesh near the fouling surface. For modelling particle transport, the generally accepted models were applied. Particle adhesion on the surface was described by a mass transfer coefficient based on the XDLVO theory. Based on the experience gained from the detailed model, a wall function approach was developed for calculating the near-wall particle transport in order to avoid the use of excessively small computational cells. The wall function model was compared to a detailed CFD model and to experimental results from a fouling test apparatus. Deposition of sub-micron calcium carbonate (CaCO3) particles on a heated stainless steel AISI 316L surface in water based suspension was used as a case study. Comparisons were made with several heat fluxes and mass flow rates applying two different high particle concentrations. As a practical case, the wall function approach was applied in the modelling of industrial corrugated heat exchanger equipment with liquid of very high particle content. For including the non-Newtonian viscosity behaviour of the high solid content slurry, the model for viscosity was derived from the experiments. The re-entrainment of the particles from the surface takes place, if the hydrodynamic forces exceed the adhesion forces even temporarily. Shear stress is a dominant force affecting the re-entrainment. For evaluating the shear strass in detail, the test apparatus was modelled using large eddy simulation (LES) method in addition to the standard k- turbulence model. The re-entrainment model presented in the literature was applied in order to evaluate the effect of surface roughness and surface energy on the re-entrainment. The model was modified for CFD application, and it was applied in fouling modelling of the practical heat exchanger. The effect of surface roughness on adhesion was studied based on the models presented in literature. In addition, the effect of particle size distribution on the fouling rate was examined.
ISBN, ISSN	ISBN 978-951-38-8250-1 (Soft back ed.) ISBN 978-951-38-8251-8 (URL: http://www.vtt.fi/publications/index.jsp) ISSN-L 2242-119X ISSN 2242-119X (Print) ISSN 2242-1203 (Online)
Date	April 2015
Language	English, Finnish abstract
Pages	117 p.
Name of the project	
Commissioned by	
Keywords	CFD, particulate, fouling, heat exchanger
Publisher	VTT Technical Research Centre of Finland Ltd P.O. Box 1000, FI-02044 VTT, Finland, Tel. 020 722 111

Julkaisun sarja ja numero

VTT Science 88

Nimeke	**Partikkelisen likaantumisen mallinnus korkean kiintoainepitoisuuden nesteseoksessa lämmönvaihtimissa**
Tekijä(t)	Ulla Ojaniemi
Tiivistelmä	Partikkelilikaantumisen mallintamiseen korkeassa kiintoainepitoisuudessa on kehitetty laskennallinen malli, joka soveltuu teollisuusmittakaavan lämmönvaihtimiin. Partikkelilikaantuminen kuvataan yleisesti peräkkäisinä tapahtumina: partikkelin kulkeutumisena pinnan läheisyyteen, kiinnittymisenä pintaan ja mahdollisesti irtoamisena pinnasta. Likaantumisnopeutta simuloitiin ensin Eulerilaisella kaksifaasimallilla, jossa kolloidisen partikkelin kulkeutumiseen nesteessä vaikuttavat voimat mallinnettiin erillisinä käyttämällä erittäin tiheää hilaa voimien vaikutusalueiden tarkastelemiseksi. Voimien mallintamisessa sovellettiin yleisesti käytettyjä malleja. Partikkelin kiinnittyminen pintaan mallinnettiin massansiirtokertoimella, jonka määrittämisessä käytettiin XDLVO-teoriaa. Yksityiskohtaisen mallin tulosten perusteella kehitettiin partikkelilikaantumisen seinämäfunktiomalli, jota soveltamalla vältytään erittäin tiheältä hilalta seinämän läheisyydessä. Seinämäfunktiomallilla saatuja laskentatuloksia verrattiin yksityiskohtaisella mallilla saatuihin tuloksiin ja laboratoriomittakaavan likaantumislaitteistolla saatuihin koetuloksiin. Testitapauksena käytettiin koetuloksia kolloidisten kalsiittipartikkelien ($CaCO_3$) likaantumisnopeudelle kuumalle ruostumattomalle teräspinnalle (AISI 316L) vesiseoksessa. Vertailuja tehtiin usealla lämpövuolla ja virtausnopeudella sekä kahdella korkealla partikkelipitoisuudella. Seinämäfunktiomallia sovellettiin käytännön kokoluokan aallotetun lämmönvaihtimen partikkelilikaantumisen mallintamiseen erittäin korkealla partikkelipitoisuudella. Korkean kiintoainepitoisuuden seoksen epänewtoniselle viskositeetille kehitettiin malli kokeellisten viskositeettimittausten perusteella. Partikkelin irtoaminen pinnalta voi tapahtua, kun siihen kohdistuvat hydrodynaamiset voimat ovat hetkellisestikin suuremmat kuin sitä kiinni pitävä adheesiovoima. Leikkausjännitys on vaikuttavimpia irtoamiseen vaikuttavia voimia. Leikkausnopeuden tarkemmaksi arvioimiseksi virtaus koelaitteiston geometriassa mallinnettiin k- -turbulenssimallin lisäksi isojen pyörteiden mallilla (LES). Kirjallisuudessa esitetyllä irtoamismallilla arvioitiin pinnan karheuden ja pintaenergian vaikutusta irtoamiseen. Malli muunnettiin virtauslaskentaan soveltuvaksi ja sitä käytettiin käytännön kokoluokan lämmönvaihtimen likaantumismallinnuksessa. Pinnan karheuden vaikutusta XDLVO-voimaan ja adheesioon arvioitiin kirjallisuudessa esitetyillä malleilla. Myös partikkelikokojakauman merkitystä likaantumisnopeuteen arvioitiin.
ISBN, ISSN	ISBN 978-951-38-8250-1 (nid.) ISBN 978-951-38-8251-8 (URL: http://www.vtt.fi/publications/index.jsp) ISSN-L 2242-119X ISSN 2242-119X (Painettu) ISSN 2242-1203 (Verkkojulkaisu)
Julkaisuaika	Huhtikuu 2015
Kieli	Englanti, suomenkielinen tiivistelmä
Sivumäärä	117 s.
Projektin nimi	
Rahoittajat	
Avainsanat	CFD, particulate, fouling, heat exchanger
Julkaisija	Teknologian tutkimuskeskus VTT Oy PL 1000, 02044 VTT, puh. 020 722 111

Modelling particulate fouling in heat exchanger with high solid content liquid suspension

A computational fluid dynamics (CFD) model for particulate fouling in heat exchangers with high solid content liquid suspension has been developed. The relevant near-wall forces were considered in modelling the colloidal particles transport and the interaction forces between the solid surfaces. A wall function approach was developed in order to avoid the use of excessively small computational cells in a near wall region. All the parameters applied in the developed wall function approach are based on the process specific parameters, derived from physical properties or literature. The study shows that the particulate fouling is controlled by interaction forces between the solid surfaces. The particle size, surface heterogeneity and the impurities in the solution have a great impact on the fouling rate. The geometry and materials applied are important in designing the heat exchangers with less fouling properties. The developed model applies to an evaluation for the colloidal particulate fouling rate in industrial size heat excangers.

ISBN 978-951-38-8250-1 (Soft back ed.)
ISBN 978-951-38-8251-8 (URL: http://www.vtt.fi/publications/index.jsp)
ISSN-L 2242-119X
ISSN 2242-119X (Print)
ISSN 2242-1203 (Online)